EINDHOVEN UNIVERSITY OF TECHNOLOGY

Eindhoven University of Technology

MASTER

Design and control of a 3 DOF actuator for a T-ROM optical storage system

Oosterbosch, R.J.M.

Award date:
2005

Link to publication

Disclaimer
This document contains a student thesis (bachelor's or master's), as authored by a student at Eindhoven University of Technology. Student theses are made available in the TU/e repository upon obtaining the required degree. The grade received is not published on the document as presented in the repository. The required complexity or quality of research of student theses may vary by program, and the required minimum study period may vary in duration.

General rights
Copyright and moral rights for the publications made accessible in the public portal are retained by the authors and/or other copyright owners and it is a condition of accessing publications that users recognise and abide by the legal requirements associated with these rights.

- Users may download and print one copy of any publication from the public portal for the purpose of private study or research.
- You may not further distribute the material or use it for any profit-making activity or commercial gain

Design and Control of a 3 DOF Actuator for a T-ROM Optical Storage System

Rudy Oosterbosch

DCT 2005.124

Master's thesis

Coaches: Ir. A.A.A. Kastelijn (Philips Research)
Dr. ir. T.J. de Hoog (Philips Research)

Supervisor: Prof. dr. ir. M. Steinbuch (TU/e)

Philips Research Laboratories Eindhoven
Storage Sector
Optics and Mechanics Group

Technische Universiteit Eindhoven (TU/e)
Department of Mechanical Engineering
Dynamics and Control Technology Group

Eindhoven, September, 2005

Abstract

The T-ROM (Talbot-ROM) optical storage system is currently a subject of interest at Philips Research. It is a novel storage solution for content distribution to portable devices that aims to combine the robustness advantage of solid-state storage with the low cost mass replication of optical storage. The system is based on a large array of optical probes that illuminate a rectangular removable card. The bit patterns stored on the card medium are recovered in a parallel fashion by detection with a conventional image sensor. In order to read out all data the probes are moved along the card medium. Accurate position information is obtained by the combined use of the image sensor and a method based on the moiré magnification technique.

The system objectives require a reliable read out, small form factor, high data throughput rate and the ability to cope with external mechanical disturbances. In order to reach the objectives, first a selection is made of the basic system configuration and motivations and specifications for a 3 degree of freedom (DOF) piezoelectric actuator are given. Afterwards, an in-plane 3 DOF piezoelectric actuator is developed at Philips Research. The challenge of the actuator design is the small form factor in construction height. By modelling and analyzing the actuator, it is shown that in out-of-plane direction the design does not satisfy the requirements. Recommendations are given for an alternate design. In order to achieve in in-plane directions a high data throughput rate and to cope with external mechanical shock disturbances, control objectives are specified. A condition for a sufficient control bandwidth, however, is a sufficient sampling rate. Currently, the control bandwidth is limited by the CCD image sensor but, theoretically, CMOS image sensor windowing offers the possibility to read out at significantly higher rates. Experimental measurements show at first sight promising results. Finally, straightforward feedback controllers are designed and closed loop simulations show a data throughput rate high enough for playing DVD quality videos and a sufficient external mechanical disturbance rejection.

Preface

This Master of Science (M.Sc.) thesis was written as a part of my final year at Eindhoven University of Technology (TU/e). This investigation was performed at Philips Research Laboratories in Eindhoven within the Group Optics & Mechanics of the Storage Sector, where I have been working on a new storage solution for content distribution.

It is not possible for me to mention all the names of the people who have been helping during this project. I will, however, acknowledge specifically Thomas de Hoog and Aukje Kastelijn for creating the possibilities of this assignment and for being my encouraging mentors at Philips Research. Their help and interest were a very important part of my final year. I also would like to thank Professor Maarten Steinbuch for his comments and suggestions during my year at Philips.

Other people who have been very helpful during my project are Christopher Busch, who familiarized me with optical storage systems in general, Walter Bierhoff, for helping me with all aspects regarding the actuator design, Erik van Dijk, for his in depth technology help on LabVIEW and CMOS detectors, and Siân Hillier, who suggested me grammatical corrections for in my report. Furthermore, I would like to thank Coen Liedenbaum and Nijs van der Vaart for giving me the opportunity for a studious internship within their research group. Last, but not least, I would like to thank Cristian Presura, for being my pleasant room mate, and everyone in the group Optics and Mechanics for the pleasant atmosphere during working hours.

Throughout the year I have experienced Philips in many fields. Aukje Kastelijn gave me the opportunity to participate in the 8th Philips Conference on Application of Control Technology in Hilvarenbeek with a demonstration on T-ROM. As a visitor I became familiar with the available expertise and experience in the field of control technology. As a member of the Philips Intern Committee I even "*got more from my internship*," with that referring to the committees slogan. Together with five other interns being spread all over Philips in the Netherlands I organized the Philips Intern Day in April at Philips Headquarters' in Amsterdam. The highlight of the day was my encounter with the Chief Executive Officer of Philips, Mr. Kleisterlee. He inspired me for the rest of my internship.

Rudy Oosterbosch
Eindhoven, September 2005

Contents

Abstract **iii**

Preface **v**

1 Introduction **1**

1.1 Problem Description and Objectives 1

1.2 Report Outline 2

2 System Description **5**

2.1 System Technology Overview 5

2.2 Position Control 6

2.3 T-ROM Demonstrator Platform 9

2.4 Newly to be developed T-ROM Demonstrator 11

3 Selection of the Basic System Configuration **15**

3.1 Positioning and Alignment Requirements 16

3.2 Distribution of the Degrees of Freedom 17

4 System Actuation **19**

4.1 Piezoelectric Actuation Principles 19

4.2 Monolithic Piezoelectric Actuation Modelling 22

4.3 Piezoelectric Positioning Mechanism 25

4.4 Discussion 28

5 Actuator Design **29**

5.1 Design Specifications 29

5.2 Conceptual Design 29

5.3 Modelling and Analysis 31

5.4 Discussion 41

6 System Modelling **43**

6.1 Linear Dynamic System Representation 43

6.2 Frame Suspension Design 45

6.3 System and Disturbance Dynamics 47

6.4 Discussion 50

7 Controller Design 51
- 7.1 Control Architecture . . . 51
- 7.2 Bandwidth Specifications . . . 53
- 7.3 Image Sensor Bandwidth Improvements . . . 57
- 7.4 Reference Trajectory . . . 58
- 7.5 Feedback Controller Design . . . 60
- 7.6 Simulation Results . . . 63
- 7.7 Discussion . . . 64

8 Conclusions and Recommendations 65
- 8.1 Recommendations . . . 66

Bibliography 67

List of Symbols 71

A System Components 75
- A.1 Illumination Unit . . . 75
- A.2 Image Sensor . . . 75
- A.3 Probe Generating Element . . . 76
- A.4 Storage Medium . . . 78

B Piezoelectric models 81
- B.1 Linearized Piezoelectric Relations . . . 81
- B.2 Generalized Maxwell Model . . . 83

C Flexures 87
- C.1 Flexible Hinge . . . 87
- C.2 Flexure Mechanism . . . 87

D Actuator Vibrations Modes 91

E Stage Dynamic System Model 93
- E.1 Dynamic System Model . . . 94
- E.2 Quasi-static Transfer functions . . . 95

F T-ROM Dynamic System Model 97

G Shock Simulation 99

Chapter 1

Introduction

Optical storage was originally mainly used for storing digital audio. Today, different optical storage media formats exist such as the Compact Disc (CD), the Digital Versatile Disc (DVD) and the Blu-ray Disc (BD), and are used for computing, sound reproduction, and video. The polycarbonate disc is flat and circular, and turns. The information on an optical disc is encoded as a spiral track of pits and lands, moulded into the top of the polycarbonate disc. The information is accessed when the pits and lands are illuminated with a laser. By measuring the reflected light intensity with a photodiode, one is able to read the data from the disc.

A key strength of optical storage is the availability of low-cost, mass replicable media for content distribution. However, the presence of several moving parts in an optical disc drive makes it sensitive to motion and shock and, in combination with the large disc size, less suitable for portable application. At Philips Research an optical storage system has been developed that is compact and aims to combine the robustness of solid state memories, such as Compact Flash, with the removability and low-cost of optical media. It is an optical ROM (Read-Only-Memory) card system, that makes use of the Talbot effect for read out of the data. It therefore is called T-ROM. The system is based on a large array of optical probes that illuminate a rectangular removable card. This is shown schematically in figure 1.1. The bit patterns stored on the card medium are recovered in a parallel fashion by detection with a conventional image sensor. In order to read out all data the probes are moved along the card medium.

Potential applications of T-ROM can be found in numerous areas. One can think of an application in hand held games or in mobile phones to playback music and movies. Also applications like e-book, e-news and e-zines, appear to be attractive applications as one can read books, newspapers and magazines on an electronic reading device while on the move. But also other fields of application, which are less obvious, may form an attractive area. One can think of upgrading toys or dolls with new functionalities like stories, music and videos for kids.

1.1 Problem Description and Objectives

The aim of the T-ROM optical storage system is a storage solution for content distribution to portable devices. A final product should approach fitting in a Compact Flash form factor (42.8 x 36.5 x 5 mm^3). The total storage capacity should be on the order of 250 MB to 1 GB and should fit on an 18 x 18 mm^2 removable data card. The corresponding data rate should match the digital versatile disc (DVD) data throughput rate (i.e. a bit rate of 10 Mbps). In the current phase of the project, Philips Research is

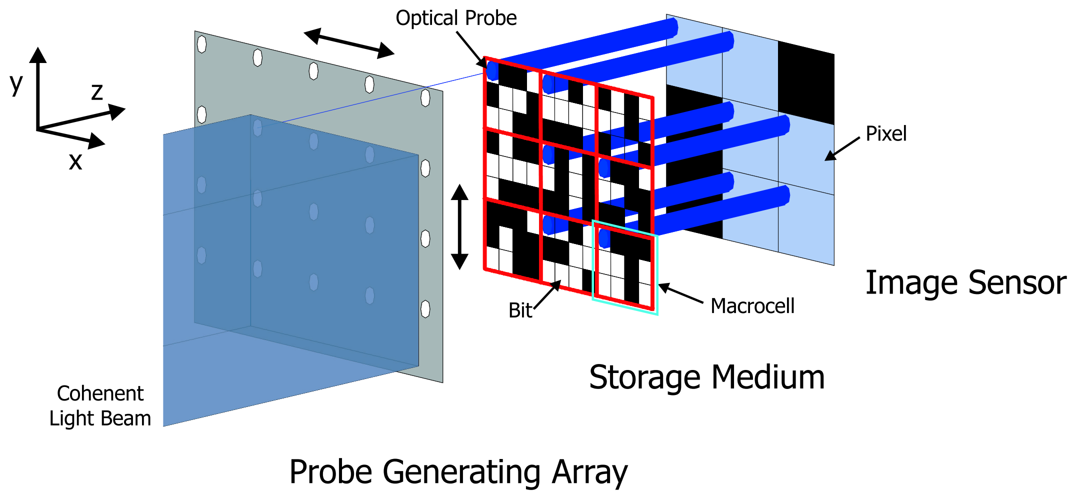

Figure 1.1: Illustration of the working principle of the T-ROM system. The data are accessed by scanning the probes over the medium.

aiming to develop a demonstration model with maximum outer dimensions of 42.8 x 36.5 x 20 mm^3. Automatic read-out should be supported and the bit rate should be, at a minimum, appropriate for playing MPEG-4 video (i.e. 1 Mbps). As the system is intended for portable application it is important to deal with external disturbances.

The objective of the work described in this report is the full integration of automatic position adjustments in the newly to be developed demonstration model, enabling reliably read-out at a data throughput rate of at least 1 Mbps. Simultaneously, the system should have the ability to cope with external mechanical disturbances. More specifically, this means that an actuator must be designed, which realizes the required adjustments. The actuator has to be driven by an actuation principle that allows accurate positioning, in order to read out data reliably. The requirements should be satisfied as well as the system dimension constraints. The illumination unit, storage medium and the image sensor restrict the actuator dimension to a maximum of 42.8 x 36.5 x 3 mm^3. Further, automatic position adjustments require a proper control system. Closed loop control is required in order to read out data reliably. At the moment the closed loop system bandwidth is limited by a few Hertz. The reason is the fact that the servo signals are generated by a CCD image sensor, which has a typical refresh rate of 30 frames per second. As portable application is in consideration, the resulting low bandwidth will also put a limit on the disturbance rejection. An option to increase the sampling rate is to use a CMOS image sensor instead of CCD image sensor, as CMOS image sensors offer the possibility to read out small regions-of-interest at a significantly higher rate than the full-frame refresh rate. Theoretically, such an approach would allow to increase the servo bandwidth significantly.

1.2 Report Outline

The chapters in this report are organized as follows. In the next Chapter an overview of the T-ROM system technology will be given. Included is a description of the current status of the system and a preview of the coming developments. In Chapter 3 the basic system configuration is discussed and different

options are proposed and a selection is made. Next, in Chapter 4, different actuation principles are discussed and a selection is made of the best option. Subsequently, an electromechanical model is given for the selected principle. In Chapter 5 a conceptual actuator design is presented, which is modelled and analyzed. In addition, conclusions are drawn about the proposed design and recommendations are given for a final design. Further, in Chapter 6, a simple one-dimensional model is given in order to discuss the data read out and the rejection of external mechanical disturbances. Some conclusions are drawn about the system suspension and also about the to be actuated directions. The control system is discussed in Chapter 7. For that purpose, some control specifications are derived before the controller is designed and simulation results are shown. In this chapter also some considerations are made of increasing the sampling rate and the use of a CMOS image sensor. Finally, in chapter 8 conclusions are drawn and recommendations are given.

Chapter 2

System Description

In this chapter a description of the T-ROM system will be given. In section 2.1 an overview of the system technology is given. Further, in section 2.2 the positioning problem is brought to attention as this is a critical system aspect. Section 2.3 gives a description of the the current status of the T-ROM system and section 2.4 discusses some important aspects of the newly to be developed demonstration model.

2.1 System Technology Overview

The system, as is shown in figure 1.1, consists of four basic components: an illumination unit, a probe generating element, a removable storage medium and a mega pixel image sensor. The illumination unit consists of a coherent light beam, with a wavelength of 405 nm, which is transformed by a probe generating element into a large array of optical probes, also called spots. The probe generating element is a metal layer with a two dimensional array of circular apertures of 1 μm diameter at a 15 μm pitch. The array of spots is generated by the Talbot effect. The Talbot effect is an optical effect that refers to the fact that a periodic structure, when illuminated with a parallel beam of coherent light, reproduces itself at a fixed distance, the Talbot distance. The Talbot distance z_T is a function of the pitch p and wavelength λ and is equal to

$$z_T = \frac{2p^2}{\lambda}. \tag{2.1}$$

In figure 2.1 it is illustrated how the Talbot effect is used in the T-ROM system. The storage medium is placed in the Talbot focal plane, i.e. at the Talbot distance. The relatively large working distance allows the use of a thick cover layer on the medium, reducing the sensitivity to contamination.

The information on the medium is coded into transparent and non-transparent data bit patterns. The size of a bit corresponds to the size of a spot. As the spot size is far smaller than a pixel size, the number of data bits fairly exceed the number of pixels. Bit patterns arise as bits are read out in a parallel. The image sensor can reconstruct the bit patterns by detecting the light that is let through by the bits. The bit pattern that is detected by the image sensor at a given time corresponds to one data page. An example of a data page taken at an experimental setup is shown in figure 2.2. Movement of the optical probes along the storage medium enable selecting and reading out different data pages. In order to read out all data pages, the maximum required moving range is determined by the spot

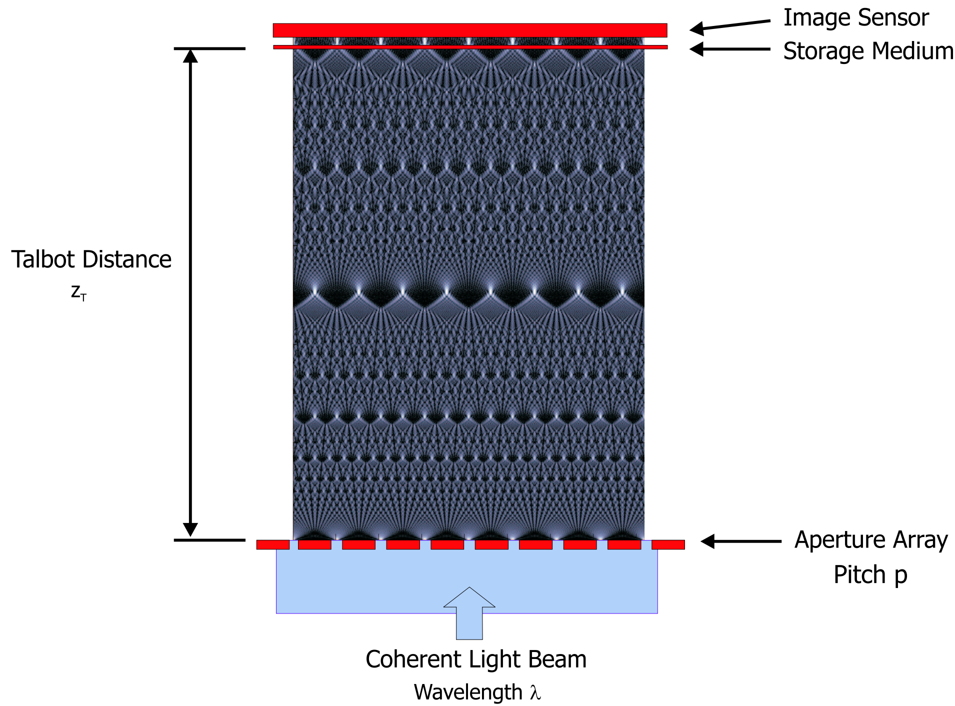

Figure 2.1: Illustration of the use of the Talbot effect in the T-ROM system. An image of the aperture array appears at the Talbot distance.

pitch. As a consequence, every spot illuminates its own group of bits. Such a group of bits is united in a so-called macrocell, as is shown in figure 1.1.

Through the multiplicity of detectable data bits by one sensor pixel, the achievable data density is fully determined by the size of the spots, and not by the resolution of the image sensor. This multiplexing technique allows to detect data bits at sub-pixel resolution. It is further noted that the exact way of transmission of the light that is let though by the data bits to the pixels is unknown, and with this also the exact distance between the storage medium and image sensor.

2.2 Position Control

The data stored on the medium is read out in a massively parallel fashion using an array of about 1000 x 1000 optical probes. As a result, a sufficiently high data rate can be achieved with relatively slow scanning movements in x and y direction, such as indicated in figure 1.1. As mentioned, the maximum required stroke of the scanning movement is defined by the spot pitch. Both a required small scanning range and low scanning rate are favorable from the point of view of system robustness. The small scanning range allows the use of high stiffness pivots, which are favorable for accurate positioning, while in the meantime being free of play and friction. Furthermore, a low scanning rate requires only a low system bandwidth. This places less stringent demands on the required sampling rate.

To access the data that are stored on the medium, it is important to accurately know the position of the optical probes relative to the position of the individual bits. Most likely the storage medium will

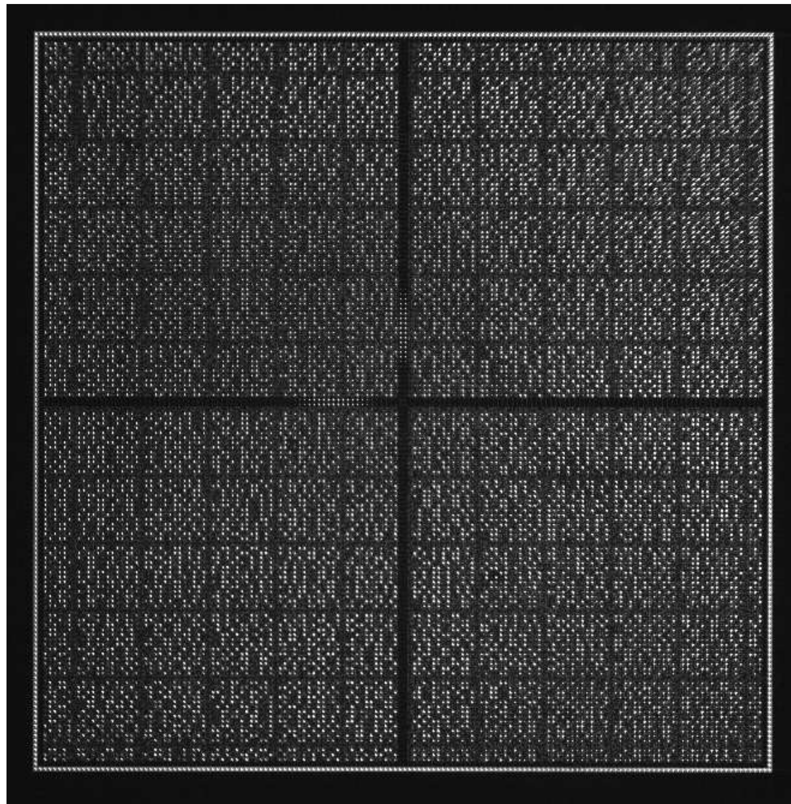

Figure 2.2: Image of a data page with moiré servo marks. The moiré fringes are clearly visible in both directions of the center cross.

not be perfectly aligned with the probe generating element and the image sensor as well. Tilt and rotation misalignments may occur. Also position offsets are to be expected due to temperature effects and manufacturing tolerances. The relative difference between the desired position at a time and the actual position of the read-out spots is denoted by a position error. Throughout this report the position error is described with respect to an x, y and z coordinate system. The z axis is chosen perpendicular to the storage medium surface, the focusing direction, whereas the x and y axis are chosen in a scanning direction. The coordinate system is defined in figure 1.1.

The small data bit sizes require accurate positioning of the spots to the storage medium. This position requirement is rather more critical than the relative position of the image sensor with respect to the storage medium as a pixel size is only on the order of a macrocell size. The relatively large pixel size, however, requires a special method to obtain information about the spot position at sub-pixel level. Therefore, a method based on the moiré magnification effect is used to obtain accurate position information. In order to obtain a moiré effect, a periodic structure with a slit pattern is imprinted on the medium in scanning directions. This periodic structure is extended along the full length of the medium. Illumination of the periodic structure will result in interference fringes as the slit pattern period is slightly different from the spot pitch. The fringe pattern is a so-called magnification of the slit pattern and is called a blob, or a servo mark, as it marks the relative position of the spots to the data bits. The principle is illustrated in figure 2.3. When the probe generating element moves with respect to the medium over a distance $\Delta\sigma$, then the fringe patterns move over a distance $\Delta\Sigma$. The period of

the fringe pattern is equal to

$$\frac{(p+\delta)\,p}{|\delta|}. \tag{2.2}$$

The parameter p represents the spot pitch and δ gives the pitch offset. The magnification factor is a function of the pitch offset, and equals $p/|\delta|$. At zero pitch offset the magnification is infinite.

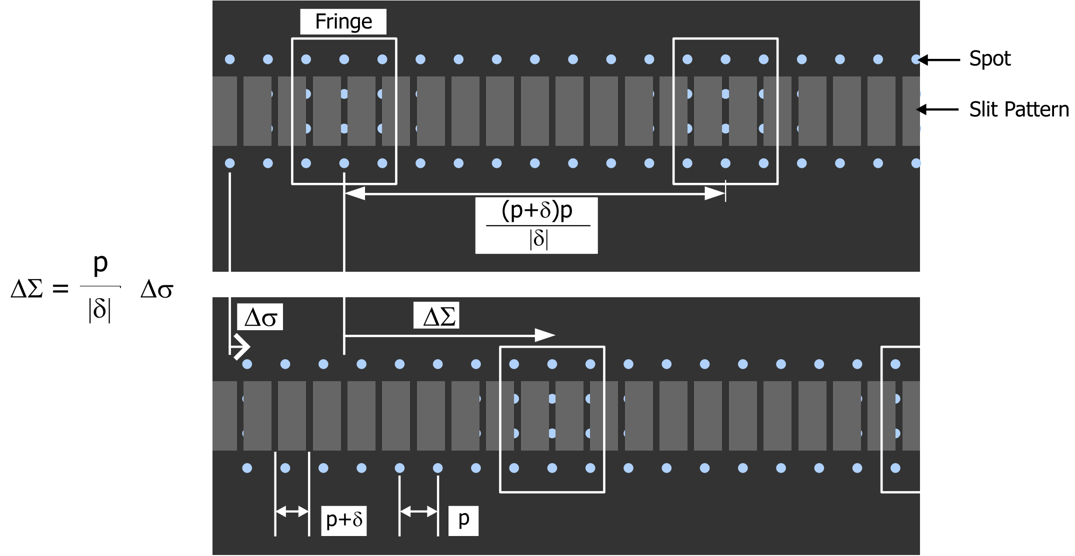

Figure 2.3: Illustration of the moiré magnification technique. The period of the slits is offset by the δ from the pitch p of the spots. Due to the moiré interference, fringes appear. When the probes are shifted over a small distance $\Delta\sigma$, the fringes are shifted over a much larger distance $\Delta\Sigma$.

The slit patterns are placed on the storage medium, in so-called servo lines, in such a way that, when the optical probes are aligned with the $(1,1)$ position in the macrocell, the centers of the bright fringes appear exactly at an edge of the data area on the medium. Suppose that there are n x n data bits in a macrocell. Then, in order to place the probes at the (i,j) position $(1 \le i,j \le n)$, the fringes should be shifted by $\frac{(i-1)}{n}\frac{(p+\delta)p}{|\delta|}$ in the x direction and $\frac{(j-1)}{n}\frac{(p+\delta)p}{|\delta|}$ in the y direction. By computing the distance between the detected fringe position and the predefined fringe position a control error signal can be generated. For a large enough magnification, the position of the fringes can be detected easily with the image sensor. The fringe pattern is clearly visible in figure 2.2 in the two bands that form a cross at the center of the medium.

The maximum resolution that can be obtained in the position detection depends on the length of the storage medium. For example, in x direction, the $(1,1)$ position in the macrocell corresponds with a fringe at the left edge of the data area, then the $(n,1)$ position in the macrocell corresponds, at maximum, with a fringe at the right edge of the data area. Otherwise, if the fringe goes beyond the medium length, the position can not be detected anymore. As the center position of the fringe can be determined with an accuracy of ± 1 pixel the resolution is defined by

$$\frac{p \cdot c}{d}. \tag{2.3}$$

Parameter c and d represent the linear image sensor pixel dimension and the linear data dimension respectively. Both will be discussed in section 2.4.

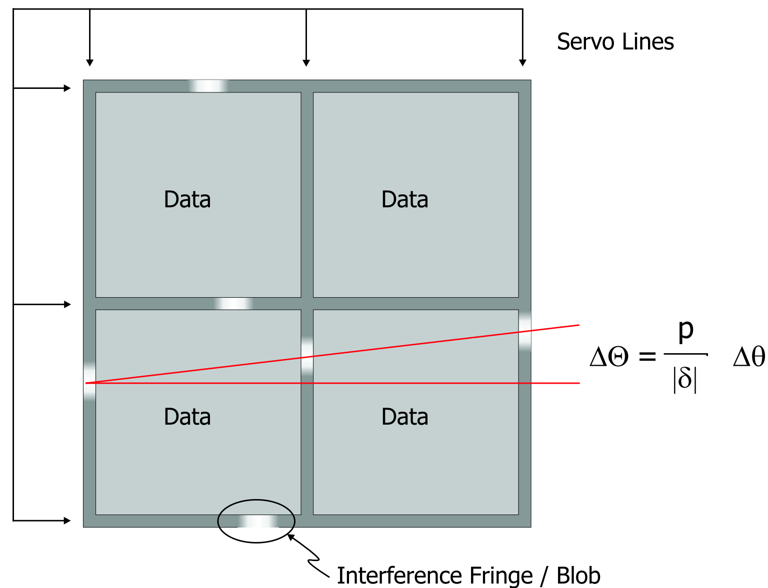

Figure 2.4: An example of a layout of servo marks for the detection of rotational misalignments. Parallel servo marks (blobs) are used. For an angle $\Delta\theta$ between the probe generating element and the medium it holds $\Delta\Theta = \frac{p}{|\delta|}\Delta\theta$.

Expanding the moiré magnification technique also rotational offsets, of the probe generating element with respect to the storage medium, can be visualized. For that purpose, multiple servo lines with slit patterns are incorporated in the medium, as illustrated in figure 2.4. An angle $\Delta\theta$ between the probe generating element and the storage medium results in a magnified angle $\Delta\Theta$, with a magnification factor $p/|\delta|$, of the line that intersects the fringes that appear along the parallel slit patterns. Finally, the moiré magnification technique will also enable to adjust the focus. The contrast of the moiré fringes is a measure of the focus quality. This is due to the fact that a moiré magnified servo mark becomes sharper when the probes with which the slit pattern is illuminated are narrower. Hence, optimizing the focus position can be done by maximizing the contrast of the fringe pattern.

So, the image sensor is incorporated in the systems for two reasons. It is both a prerequisite for data read out and to position the optical probes with respect to the storage medium with a high accuracy level.

2.3 T-ROM Demonstrator Platform

A compact demonstrator with integrated light path was built to demonstrate the complete T-ROM data retrieval concept: insertion of the removable medium, scanning of the macrocells by using the optical probes, detecting data bits by an image sensor and calculating the required servo signals on a PC with a LabVIEW interface. A photograph of the demonstrator is shown in figure 2.5. The outer dimensions of this demonstrator are 80 x 80 x 50 mm^3. The review of the demonstrator given in this section is based on the description given in [12].

The illumination unit consists of a coherent light beam (blue laser diode with a wavelength of 402 nm), which is reversed by a prism and a grating for a compact design, and is transformed by an aperture array into a large array of optical probes. The aperture array, in turn, is mounted on a actuator stage

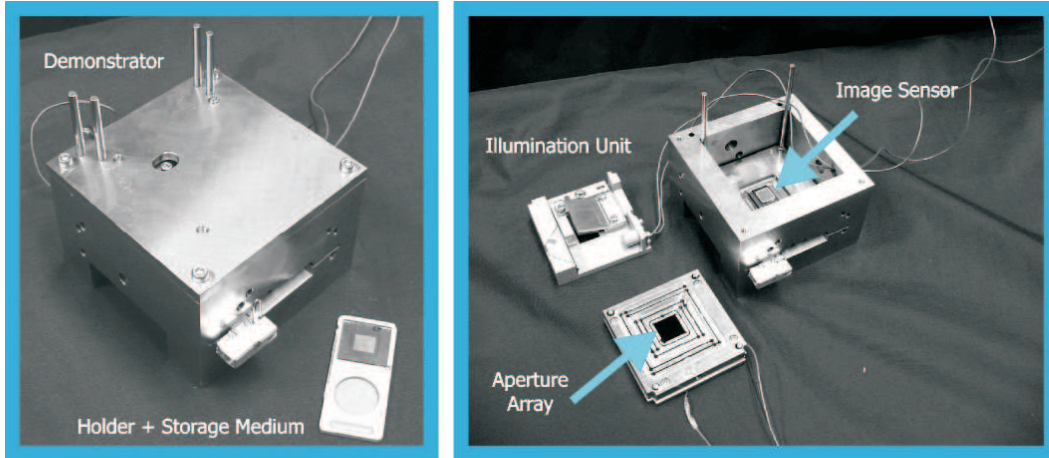

Figure 2.5: Photograph of the T-ROM demonstrator in an integrated (left) and in a partly disassembled state (right).

with two monolithic piezoelectric elements incorporated to obtain macrocell scanning. The stage was manufactured by Physik Instrumente. The scanning range is 16 μm in both directions. The aperture array itself consists of circular apertures, of 1 μm diameter and 15 μm pitch, imprinted in a thin layer of chromium on top of a quartz base. The apertures have been made with electron beam lithography. In the same way the storage medium has been manufactured. This particular medium contains data bits with a linear dimension of 1 μm and has therefore 225 data pages. For easy insertion the storage medium is mounted in a holder. The image sensor is a Dalsa CCD sensor with a resolution of 1024 x 1024 pixels. The pixel size is 7.5 x 7.5 μm^2 and therefore results in an oversampling ratio of 2, i.e. 4 pixels for each macrocell. In order to transfer the light that is allowed through by the data bits to the image sensor, a fiber channel plate, with fiber diameter of about 3 μm, is mounted on top of the sensor. When inserted in the demonstrator, the medium is placed in direct contact with this fiber plate.

The optical probes are positioned by automated feedback control onto the data bits on the storage medium, in both the x and y directions. The control is realized by means of an implemented proportional and integral feedback control algorithm in LabVIEW. As the corresponding system bandwidth is on the order of several Hertz, the data rate is limited by several Kbps. Position information is obtained from moiré servo marks, as was described in the previous section. As the used slit pattern has a period of 15.04 μm the resulting moiré magnification factor is 375. As the center position of the fringes can be determined with an accuracy of ± 1 pixel an adjustment resolution of ± 20 nm is obtained, which is within the requirement (± 100 nm). The width of the slit in the slit pattern is 1 μm. As a result the width of the fringes is about 60 pixels, at optimum focus. Finally, for each servo line, the position error signal is determined by correlating the measured servo mark intensity with the theoretical servo mark intensity.

Figure 2.6 shows a schematic overview of the scanning control as used in the T-ROM demonstrator. It is seen that before applying blob detection and error signal generation, the CCD image sensor is read out first and a frame is grabbed by the 12 bit RoadRunner frame grabber. Secondly, the grabbed frame is provided though the LabVIEW interface to the blob detection and error signal generation algorithms. Finally, after control, the control inputs to the piezoelectric elements are amplified by a factor 10. Note that the adjustments of the focus and in-plane rotations are still carried out manually.

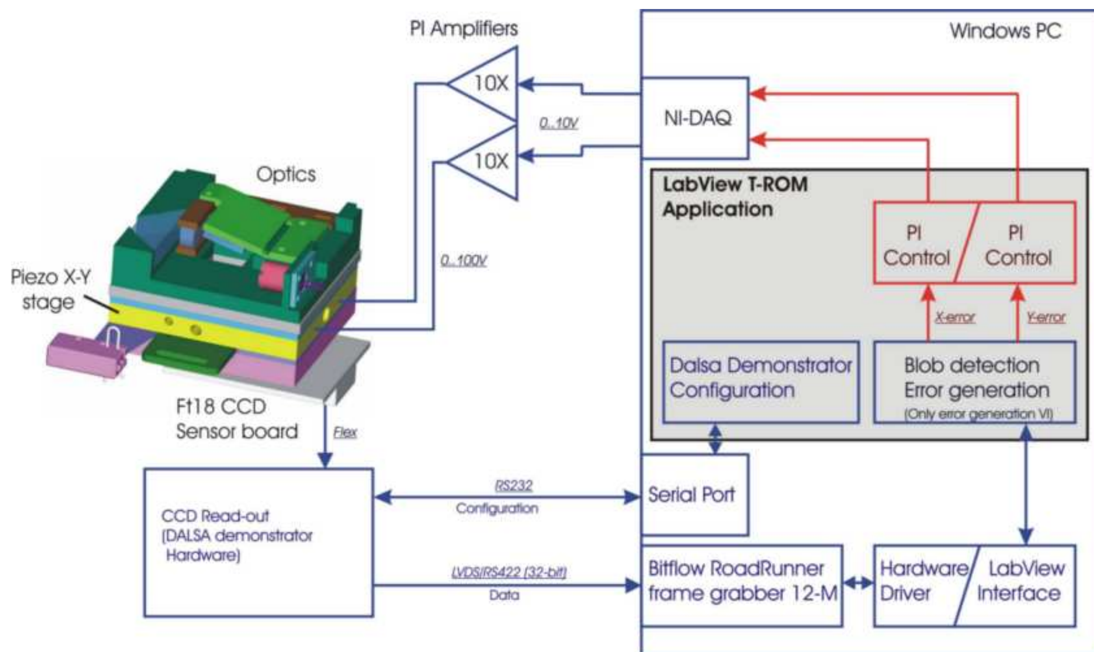

Figure 2.6: Schematic overview of the control loops present in the T-ROM demonstrator platform.

2.4 Newly to be developed T-ROM Demonstrator

The storage medium format structure, as used in the demonstrator described in the previous section is schematically represented in figure 2.7, with one highlighted macrocell. The macrocell size and bit size are denoted by respectively p and b, while the dimension of the storage medium is denoted by d. Such a two dimensional medium format has been at the center of attention in the Two-Dimensional Optical Storage (TwoDOS) project at Philips Research [17]. Two-dimensional optical storage aims at increasing the data capacity and the data throughput rate for conventional optical storage systems, like CD, DVD and BD, which are in essence one dimensional, by combining parallel read-out and advanced signal processing. Experimental results show a significant increase in data throughput rate and storage capacity with respectively 10 and 2 times. However, a major drawback of the presented two dimensional medium format structure is the significantly increasing signal processing power, as cross-talk of neighbouring tracks is significantly larger. Here cross-talk is the spurious and unwanted signal coming from the light that impinges upon neighbouring bits. The corresponding significantly higher costs make the presented two-dimensional medium format structure unrealistic to use.

For the newly to be developed demonstration model of the T-ROM optical storage system, therefore, an alternative concept based on conventional optical disk formats is proposed. As in CD, DVD and BD players, the data is read in adjacent tracks. The cross-talk to neighbouring tracks is rather lower than in the two-dimensional optical storage medium format presented in TwoDOS. Along the track, the data can be recovered by using standard signal processing techniques. A schematic representation is shown in figure 2.7. The track pith (TP) and channel bit length (CBL) are represented by the parameter t and b respectively. The dimensions depend on the storage capacity and the size of the medium. In accordance with optical disk formats, the direction along the track is called the tangential direction, the direction across the track is called the transversal direction and the direction perpendicular to the medium is called the focus direction.

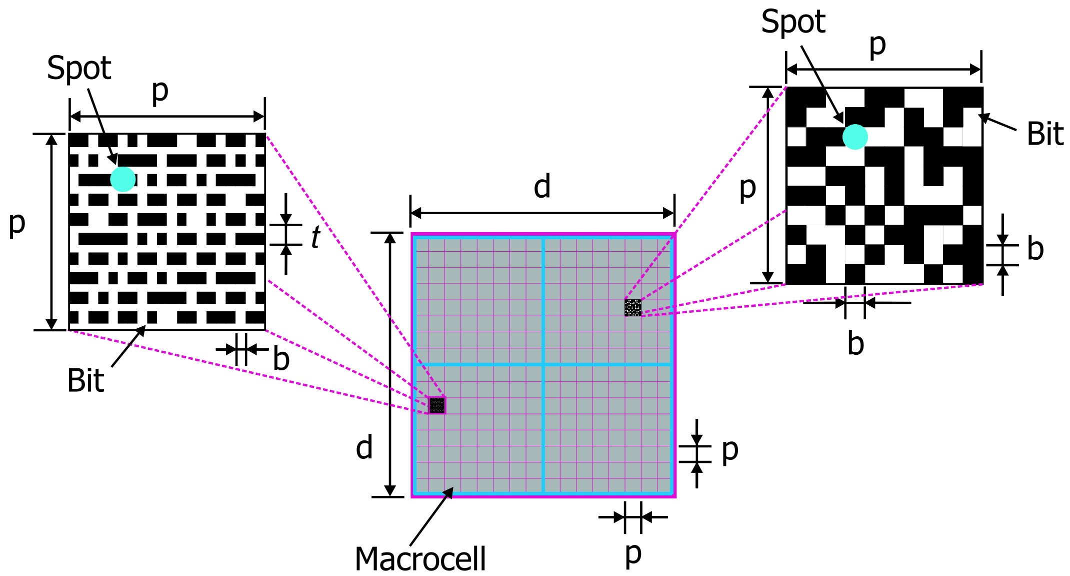

Figure 2.7: Two-dimensional medium format containing macrocells (middle) with both the old configuration, with square bits, (right) and the new configuration, with bits placed in tracks (left).

For the new demonstrator model a user storage capacity of 100 Mb is proposed, combined with current state-of-the-art technology. With an encoding efficiency of 50% this means a total required storage capacity of 200 Mb. The storage medium dimension d, as shown in figure 2.7, will be 7.3 mm. The corresponding channel bit length b and track pitch are respectively 75 nm and 422 nm. A derivation of these values is given in Appendix A. Further, the laser wavelength and the spot diameter, the full width at half maximum, are assumed to be respectively 405 nm and 338 nm. The spot depth of focus is 560 nm and the number of spots is on the order of 0.3 million. The image sensor is a mega-pixel sensor with a pixel size of 6.7 x 6.7 μm. The oversampling ratio is 2, i.e. 4 pixels for each macrocell. The new configuration of the storage medium is discussed here as it put severe demands on the position accuracy of the system, as will be seen in the next Chapter. All relevant parameters and values are once more summarized in table 2.4. All values are derived in Appendix A.

It is noted that for the final aim of the T-ROM system a storage medium size of 18 x 18 mm^2 is suggested, as was mentioned in section 1.1. Obviously, for the same storage medium format structure, this leads to a higher storage capacity and also to more spots. Consequently, in order to obtain the required bit rates, the sensor refresh rate will be lower. This will result in lower a scanning rate. As this only serves as note, the bit rates mentioned in the table will be retained.

Table 2.1: Overview of the parameters values for the newly to be developed demonstration model.

Parameter	Variable	Value	Unit
Wavelength	λ	405	nm
Spot Diameter (FWHM)	a	338	nm
Spot Depth of Focus	F_D	560	nm
Number of Spots	N	$3.0 \cdot 10^5$	
Talbot Distance	z_T	0.9	mm
Sensor Pixel Dimension	c	6.7	μm
Sensor Surface Dimension	u	7.3	mm
Number of pixels	K	$1.2 \cdot 10^6$	
User Storage Capacity	V	100	Mb
Encoding Efficiency	η_{enc}	0.5	
Data Area Dimension	d	7.3	mm
Spot Pitch / Macrocell Dimension	p	13.4	mm
Channel Bit Length (CBL)	b	75	nm
Track Pitch (TP)	t	422	nm
Bit Rate	D		
• MPEG-4 quality		$1 \cdot 10^6$	bit/s
• DVD quality		$10 \cdot 10^6$	bit/s

Chapter 3

Selection of the Basic System Configuration

A critical aspect in the T-ROM system is the positioning and alignment of the probe generating element, the storage medium and the image sensor with respect to each other. Loading a new medium will introduce deviations in the alignment. The positioning and alignment problem is discussed on the basis of the illustration given in figure 3.1. The probe generating element, the storage medium and the sensor surface are presented here with respect to a reference frame fixed at the probe generating element. The positioning problem is in terms of x, y and z direction while the alignment problem handles the φ, ψ and θ directions. The distance z_T represents the Talbot distance while the distance between the storage medium and the sensor is denoted by z_S. In section 3.1 requirements on the po-

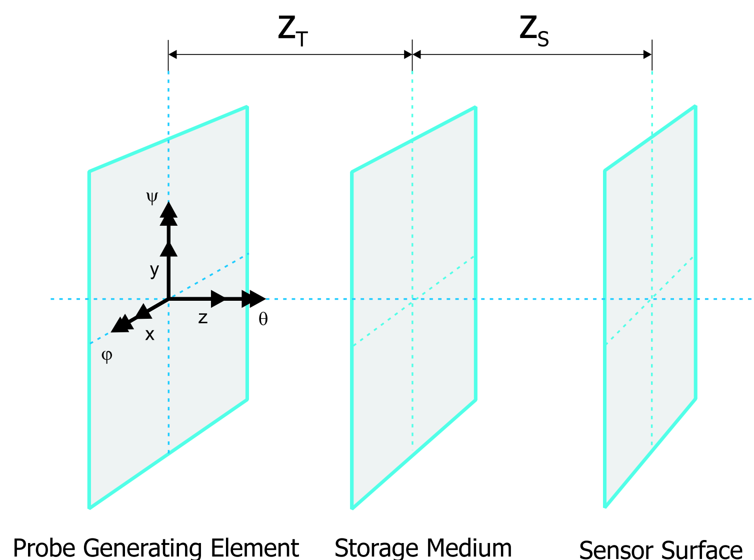

Figure 3.1: The positioning and alignment of the probe generating element, the storage medium and the image sensor presented with respect to a reference frame.

Table 3.1: Positioning and alignment requirement.

Direction	Tangential [μm]	Transversal [μm]	Focus [μm]	Tilt [μrad]	Rotation [μrad]
Stroke	13.4	13.4	30	0	$5 \cdot 10^3$
Accuracy	$\pm 7.5 \cdot 10^{-3}$	$\pm 42 \cdot 10^{-3}$	$\pm 140 \cdot 10^{-3}$	± 39	± 2

sitioning and alignment are derived. In order to position the probe generating element, the storage medium and the image sensor with respect to each other, such that the data is read out reliably, in section 3.2 the distribution of the degrees of freedom over three elements is discussed.

3.1 Positioning and Alignment Requirements

The probe generating element and the storage medium are the most sensitive parts of the system. It is very important that the storage medium is precisely placed at the Talbot distance, in the Talbot focal plane, and that the elements are aligned with respect to each other with a high accuracy level. Rotation misalignments, i.e. rotation around the z axis, between the probe generating element and the storage medium will introduce cross talk and therefore affects the bit error rate negatively. Here, the bit error rate is the ratio of the number of bits incorrectly received to the total number of bits illuminated during a specified time interval. The corresponding tilt alignments, i.e. rotations around the x and y axis, will also affect the bit error rate negatively as not every generated spot will be equally focussed on the storage medium. Rotation and tilt misalignments between the storage medium and image sensor surface are less critical as cross talk is less due to the relatively large pixel sizes and the multiplexing technique. The positioning accuracy in x,y and z direction is also less critical. Although the exact in-between distance z_S is still unknown the final distance will be on the same order as the Talbot distance.

The allowed spot deviations relative to the data bits, in all directions, are limited by the requirements determined by the optical principles of the read out. In tangential direction, the demands put upon the spot deviations follow from cross-talk considerations. In transversal direction the spots should be positioned close to the middle of the tracks in order to be able to illuminate all macrocells at the correct position and the same time. Further, the rotational accuracy should be better than one channel bit length over the length of the medium. In focusing direction, to prevent out of focus illumination, the position accuracy should be better than the focus depth. Finally, the corresponding tilt accuracies should be better than the focus depth over the length of the medium.

In order to quantify the positioning, accuracy margins are selected. The system should be within the accuracy margins at all times. The accuracy margins are defined in tangential, transversal and focus direction and are in percentage of the channel bit length b, the track pitch t and the focus depth F_D respectively. The accuracy margin ξ for each direction is defined here according to

$$\begin{aligned} |\xi_{tangential}| &\leq 10\% \; b \\ |\xi_{transversal}| &\leq 10\% \; t \\ |\xi_{focus}| &\leq 50\% \; F_D \end{aligned} \tag{3.1}$$

By using the parameter values given in table 2.4 the corresponding margins are respectively ± 7.5, ± 42 and ± 140 nm. The corresponding tilt and rotational accuracy levels can be calculated by considering the length of the medium. For the medium length defined in table 2.4 the tilt accuracy is 39 μrad and the rotational accuracy is 2 μrad. All accuracy levels are once more summarized in table 3.1.

Table 3.2: Different options for distributing the degrees of freedom over the system components

	Probe Generating Element	Storage Medium	Image Sensor
1	L_x, L_y	L_z,R_z	
2	L_x, L_y, R_z	L_z	R_z
3	L_x, L_y, L_z	R_z	
4	L_x, L_y, L_z, R_z		R_z
5		L_x, L_y, L_z, R_z	
6	R_z	L_x, L_y, L_z	R_z
7	L_z	L_x, L_y, R_z	
8	L_z, R_z	L_x, L_y	R_z
9	L_x	L_y, L_z, R_z	
10	L_x, R_z	L_y, L_z	R_z
11	L_x, L_z	L_y, R_z	
12	L_x, L_z, R_z	L_y	R_z

3.2 Distribution of the Degrees of Freedom

From the considerations of the previous section it follows that four degrees of freedom (DOF) must be actuated. Tilt alignments (i.e. in φ and ψ direction) are not involved as the required accuracy level is far lower than the required accuracy level for rotational misalignments (i.e. θ direction) and they are assumed to be handled by the loading mechanism of the medium. Two DOFs are required in order to read out all data on the storage medium, as the probe generating element has to move with respect to the storage medium in both tangential and transversal direction. Focusing on the storage medium with respect to the probe generating element is the third DOF to be actuated. Further, when inserting a medium, a rotational misalignment has to be compensated by either the medium or both the probe generating element and sensor. This misalignment in θ direction is the fourth DOF to be actuated. Although the loading mechanism is not known yet it is assumed that the mechanism is strong enough to withstand forces induced by loading the medium, even if this is done by hand.

The positioning and alignment can be obtained by a variety of system configurations. Given the restrictions, there are 12 options to divide the required degrees of freedom over the components. All options are given in table 3.2 in terms of translations and rotations. The translations are defined by L_x, L_y and L_z and the corresponding rotation is defined by R_z. For options 1 to 4 the translations L_x and L_y are implemented at the probe generating element, for options 5 to 8 the translations L_x and L_y are implemented at the medium, and for options 9 to 12 the translations L_x and L_y are decoupled. Notice that L_x and L_y are exchangeable. The final decision whether L_x or L_y is in transversal or tangential direction will be made in Chapter 6. During evaluation of the options, a number of criteria are identified as follows

- Moving the sensor is a bad solution, as the sensor has a connector, and the biggest volume/mass.
- Having less DOFs implemented at the medium is favorable, as the construction around the medium will experience the biggest load when loading the medium. When allowing motion at the medium to facilitate a DOF, low stiffness is introduced.
- Having less DOFs collocated with R_z is favorable, as this DOF requires the highest accuracy.

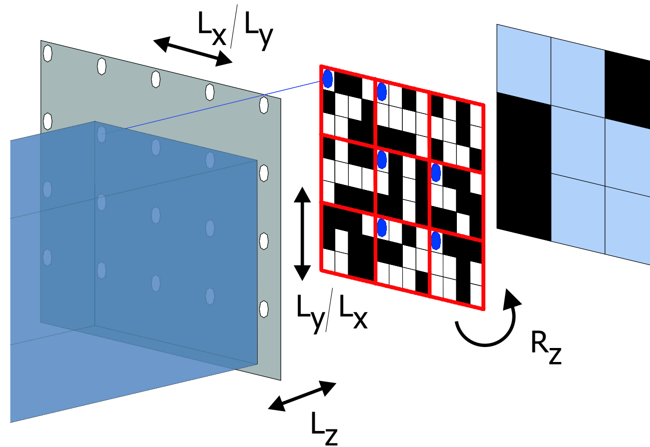

Figure 3.2: The best option of distributing the degrees of freedom over the system components: the translations at the probe generating element and the rotation at the storage medium. Translations L_x or L_y are exchangeable.

Implementing other DOFs at the same component will introduce cross-talk between R_z and this DOF.

- Moving the probe generating element is favorable over moving the medium, as the probe generating element has the lowest volume and mass.

Based on these criteria the option with the rotation R_z implemented at the medium, and all other DOFs (L_x, L_y, L_z) implemented at the probe generating element, is the best option. This is shown schematically in figure 3.2. The corresponding strokes for L_x and L_y are based on the macrocell size, and therefore at least 13.4 μm. The stroke in focus direction L_z and the required rotation R_z should compensate for introduced deviations when a storage medium is loaded. They are assumed to be respectively 30 μm and 5 milliradians. It is noted that in the tangential and transversal direction it is not necessary to compensate for deviations when a storage medium is loaded. The only condition is that the number of spots exceed the number of macrocells, in both tangential and transversal direction. All required strokes and accuracy levels are summarized in table 3.1.

Chapter 4

System Actuation

The best option to actuate the degrees of freedom, as were derived in de previous Chapter, are based on system requirements. In the T-ROM system, the probe generating element has a typical mass of 0.5 gram and the displacement requires a 7.5 nanometer accuracy at maximum. Simultaneous gravity compensation requires a stiffness of, at least, $6.7 \cdot 10^6$ N/m. These requirements are best met by closed loop operation but, as the system sensor bandwidth is limited to several Hertz, the required stiffness should be incorporated into the system as passive mechanical stiffness. To also fulfill the specified scanning range of 13.4 μm a force of 9 N is required. In an ordinary electromagnetic actuator, as extensively used in CD or DVD players, the actuator force is related to the current according to

$$F(t) = BI(t)l \sin \upsilon, \tag{4.1}$$

where the magnetic induction B is typically 0.5 T and the length of the conductor in the field l is 10 mm. Assuming the current acts perpendicular to the magnetic field, i.e. υ is 90 degrees, the required force results in a current I of approximately 1800 Amperes. This conflicts with the condition of low power consumption and moreover due to the current density, of typically 10 Amperes per square millimeter, a too large wire volume would be required. Because of the reasons mentioned an electromagnetic actuation system is inappropriate to be used in the T-ROM system.

In recent years, piezoelectric materials and actuators have received considerable attention in literature and have become a standard option in positioning applications where the displacements must be small and highly accurate [36]. Instruments such as the scanning tunnelling and atomic force microscopes almost universally use piezoelectric actuators to generate the fine motions required [1], [35] and [40]. Piezoelectric actuators are also known for their capability of generating large forces [26]. The combination of accurate positioning and large force generation should make piezoelectric actuators appropriate to use in the T-ROM system. In the next paragraph an overview is given of most common piezoelectric actuation principles. In section 4.2 the modelling of monolithic piezoelectric elements is discussed in more detail and finally, in section 4.3, a monolithic piezoelectric element incorporated in a translation stage is discussed separately.

4.1 Piezoelectric Actuation Principles

Piezoelectric elements use the inverse piezoelectric effect to convert electrical energy into mechanical energy. Piezoelectricity is the ability of certain crystals to induce an electrical charge when subjected to mechanical stress. This effect is reversible, and so piezoelectric crystals, subjected to an externally

applied voltage, can deform a small amount. These relations are shown schematically in figure 4.1. This deformation forms the basis for piezoelectric actuation principles.

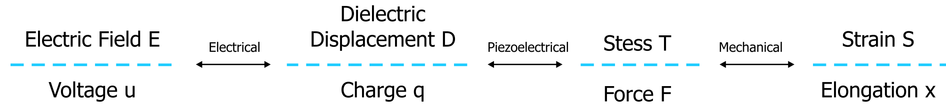

Figure 4.1: Schematic representation of piezoelectric relations.

Many piezoelectric actuation principles are known. In this section an overview is given of the most common principles. The criteria of comparison are mainly concentrated on the performance and a compact design. For performance, besides a maximum moving range large enough for focusing and scanning, the stiffness and the generated force have to be sufficient in order to cope with external mechanical disturbances. Also a self-braking system is preferred, meaning that due to internal friction the system can not be displaced by external forces. As the internal friction blocks the position this allows to switch of the power to the system.

4.1.1 Monolithic piezoelectric elements

Applying an electric field to a monolithic piezoelectric element results directly in material deformation. The direction in which the material deforms depends on the polarization direction of the dipoles present in the piezoelectric ceramic. Different modes are distinguished. Stage positioning can be obtained by physically coupling the element to the stage (for example by using an adhesive layer). In general the deformation, stiffness and generated force depends upon the element length, width and thickness. Typical field strengths are on the order of 2 kV per millimeter element thickness. When using the multi-layer technique (stacks) the operating voltage can be reduced while the performance is retained. Making use of stacks the power consumption is on the order of several Watts. As a monolithic piezoelectric element operates as capacitive load it consumes almost no power in static application and therefore it produces almost no heat. Issues of monolithic piezoelectric elements are hysteresis, drift, aging and also the decreasing lifetime in a (very) long-term static mode, especially when operating at maximum input voltage.

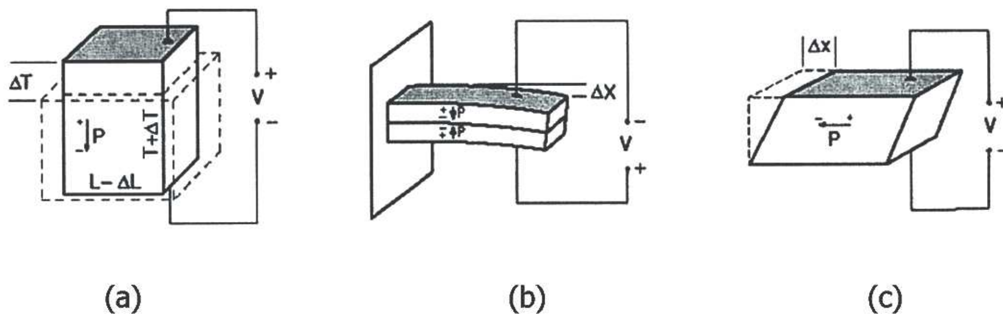

Figure 4.2: Different types of monolithic piezoelectric elements: (a) the expansion or contraction type, (b) the bender type and (c) the shear type [27].

The three modes of monolithic piezoelectric elements that are distinguished are the longitudinal, the transversal and the shear mode. The first mode is widely used in precision engineering. Examples can be found in diesel fuel injection systems [21], translation stages [24] and printer heads [39]. The electric field in this mode has the same polarity and orientation as the polarization direction of the dipoles. By applying an electric field across a single layer of a piezoelectric ceramic, the layer will expand in the thickness direction or longitudinal direction (i.e. along the axis of polarization). At the same time, the layer contracts in the transverse direction (i.e. perpendicular to the axis of polarization) as shown in figure 4.2(a). The latter refers to the transversal mode. In longitudinal mode, maximum strain levels of typically 0.1% can be achieved, i.e. $1\ \mu$m elongation per millimeter element thickness. As those layers have a high stiffness and can generate large forces, a combined use with levers is suitable, in order to obtain significantly larger displacements. This type of monolithic piezoelectric element is known as an expansion or contraction motor.

A second type of monolithic piezoelectric element is the bender of bi-morph which produces a bending motion. At least two layers are required. Bender motion occurs when one layer expands and the other layer contracts in the transverse direction. This is shown schematically in figure 4.2(b). The displacement range achieved at the tip of piezoelectric element is large compared to the displacement with an expansion and contraction motor, but the corresponding generated force and stiffness are considerably lower. In proportion to the expansion and contraction type, this type is very fragile. Bimorphs are often used for active vibration damping. Examples can be found in MRI scanners [31] and hard disk drives [37]. A third type is the shear motor, named after the use of the shear mode to obtain a displacement. This type is shown schematically in figure 4.2(c). As the performance of this type of piezoelectric element is limited it is here not discussed further. For more information on the shear mode and its applications one is referred to [25].

4.1.2 Piezoelectric stepping devices

In a piezoelectric stepping device, stage positioning is obtained by sequentially activating and deactivating monolithic piezoelectric elements while friction elements are used to hold the position. Such stepping devices can easily span a wide range at high resolution while in the meantime it is possible to relax the piezoelectric element. An illustration of the stepping principle is given in figure 4.3. Examples of stepping devices can be found in [13], [18] and [41].

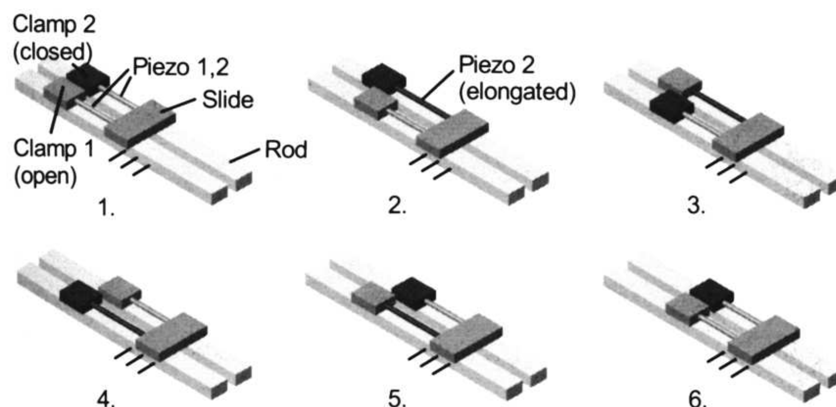

Figure 4.3: The principle of a piezoelectric stepping device: piezoelectric element 1 and 2 are sequentially activated and deactivated while clamp 1 and 2 sequentially hold the position [18].

A major drawback of most types of stepping devices is the need for more than one piezoelectric element. Therefore, besides the costs, rather a complex structure is required to position the device (move and clamp). Furthermore, a high resolution can only be obtained when the friction elements are designed and manufactured carefully concerning the stick-slip conditions. Concerning the stick-slip also the smoothness of the motion becomes an issue.

4.1.3 Piezoelectric ultrasonic devices

The principle of piezoelectric ultrasonic devices is based on generating waves in the ultrasonic frequency range in a piezoelectric ceramic plate. In the main type the waves are created by simultaneous generating a longitudinal extension mode and a transverse bending mode (both > 20 kHz). The simultaneous excitation of these two modes creates a small elliptical motion of the ceramic edge. Both modes are schematically shown in figure 4.4. Through frictional contact, of the edge with a stage, the tangent forces can realize a stage motion. For a sufficient traction the contact conditions as well as normal forces between both interacting bodies are crucial. Examples of ultrasonic devices can be found in [19] and [38]. A special type of ultrasonic devices are surface acoustic wave devices. In this type the elliptical motion is obtained by generating waves (> 1 MHz) at the surface of the ceramic plate inducing a travelling wave through the whole plate. Again the stage is friction driven, as is shown in figure 4.5. Applications are found in [5] and [32].

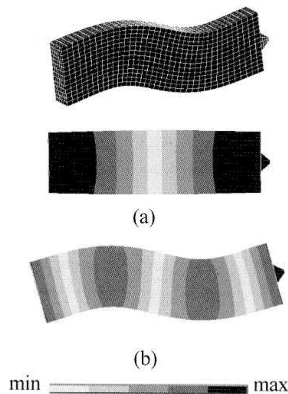

Figure 4.4: Schematic representation of longitudinal extension mode (a) and transverse bending mode (b) in a piezoelectric ceramic plate (top) [38].

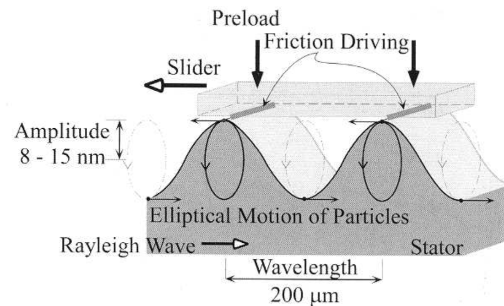

Figure 4.5: Illustration of the surface acoustic wave principle [32]. The slider is driven by the elliptical motion of the particles through frictional contact.

Ultrasonic devices are known for their large thrust forces. To obtain a robust support relatively large actuator dimensions are required. The advantage, like in the stepping device, is that the position is blocked when the device is not powered as the stage will stick to the surface.

4.2 Monolithic Piezoelectric Actuation Modelling

For a compact design, monolithic piezoelectric elements are preferred. The expansion and contraction motor is especially preferred, due to its good performance. Although the system is not self-braking,

while stepping and ultrasonic devices are, a compact design is seen to be more important. However, as mentioned in section 4.1.1, a monolithic piezoelectric element consumes almost no power in static application, as it operates as capacitive load. Furthermore, by closed-loop operation, the negative effects of hysteresis and drift can be eliminated as well as the lifetime issues.

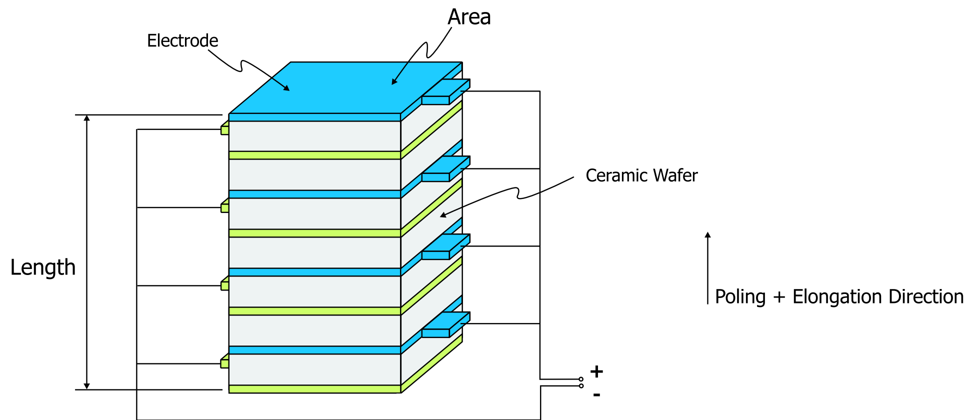

Figure 4.6: Monolithic piezoelectric stack element with ceramic wafers operating in longitudinal mode.

A piezoelectric stack element is shown schematically in figure 4.6. The wafers of a piezoelectric stack element are connected in series mechanically and in parallel electrically. The mutual relations are given in figure 4.1. To link the electrical and mechanical quantities of piezoelectric materials, linearized constitutive relations were formulated by a standards committee of the IEEE in 1987 [33]. The relations suppose that the material strain and dielectric displacement (charge per unit area) exhibited by a piezoelectric ceramic are both linearly affected by the mechanical stress and electrical field to which the ceramic is subjected. A brief overview of these relations is given in Appendix B but for further analysis one is referred to [28] and [31]. The linear constitutive relations, however, fail to describe the nonlinear behavior that is present in all piezoelectric ceramics. Experimental results had shown that the nonlinearity lies solely in the electrical domain and is mainly caused by hysteresis ([9], [29], [11] among many others). The amount of hysteresis is on the order of 15% of the elongation and depends not only on the magnitude of the input but also on the input history [8]. The hysteresis effect is shown in a voltage steering configuration and not in a charge steering configuration. This is illustrated schematically in figure 4.7.

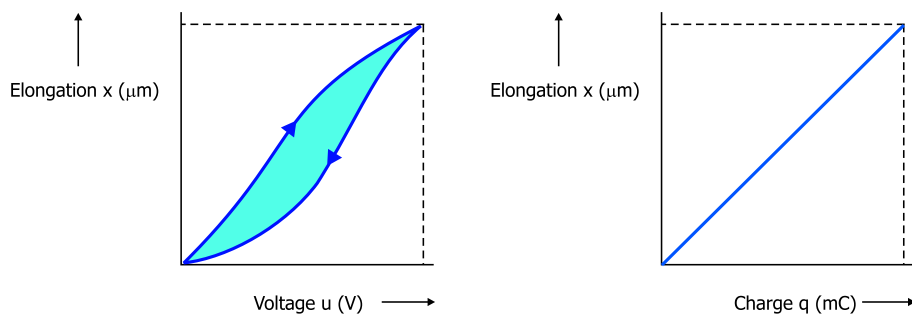

Figure 4.7: Schematic representation of the variation in elongation obtained in a voltage (left) and charge (right) steering configuration.

Describing the interaction of the mechanical and the electrical quantities a more convenient and intuitive model, based on [9] and [1], can be used. This model is more convenient and intuitive as it has several analogies with DC permanent magnet motors. The model is shown schematically in figure 4.8. The basis describing the constitutive electromechanical relations is formulated by

$$\begin{aligned} F_p(t) &= T u_p(t), \\ q_p(t) &= T x_p(t). \end{aligned} \tag{4.2}$$

Here force F_p and position x_p represent respectively the transduced force from electrical side and the actual piezoelectric element elongation whereas charge q_p is piezoelectric element charge and voltage u_p is the voltage across the piezoelectric element. The parameter T represents the electromechanical transformer ratio. Relation (4.2) is in analogy with the motor and generator law as used in DC motor modelling. This equation suggests a linear relation between the voltage across the piezoelectric element and the transduced force but in fact a distinction is made in modelling the hysteresis and piezoelectric effect. As can be seen from figure 4.8 it applies that

$$u_p(t) = u_{in}(t) - u_H(t). \tag{4.3}$$

Here voltage u_{in} is the applied voltage and voltage u_H is defined as a function of the applied charge according to

$$u_H(t) = H\left(q_{in}(t)\right), \tag{4.4}$$

where H is an operator representing the hysteresis on the electrical side. By changing the traditional voltage steering for charge steering it is possible to bypass the hysteresis effect. This results in a simplified definition for u_p, replacing (4.3), according to

$$u_p(t) = \frac{1}{C}\left(q_{in}(t) - q_p(t)\right), \tag{4.5}$$

with capacitance C representing the sum of capacitances of the individual wafers of the piezoelectric element. To compensate for hysteresis when using voltage steering, several models can be found in literature. All of them have particular advantages and disadvantages. Examples are a model based on non-linear first-order differential equation [1], the Preisach model [8], [23] and the generalized Maxwell slip model [9]. In Appendix B a short description of this generalized Maxwell model is given. The generalized Maxwell model is preferred above other models as the hysteresis effect is completely mechanically represented.

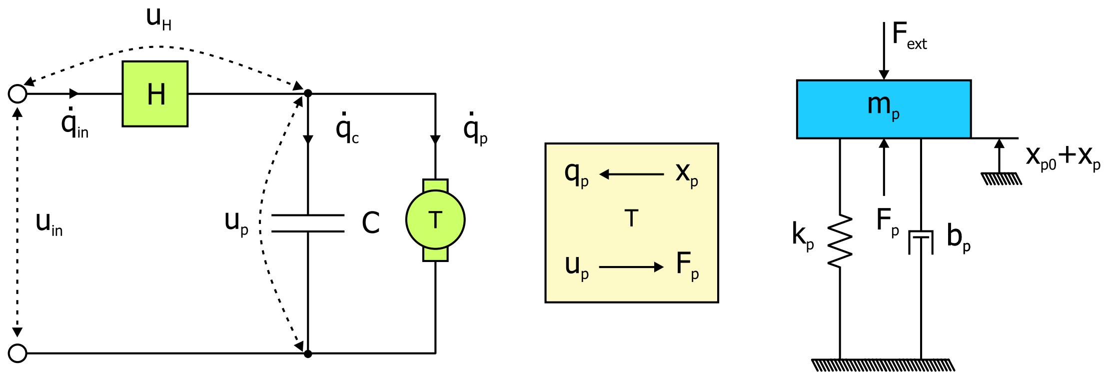

Figure 4.8: Electromechanical model representing a piezoelectric element.

A good approximation representing the mechanical side of (4.2) is found in [1]. The piezoelectric element is mechanically modelled as a distributed parameter system but a lumped parameter model was demonstrated to be a good approximation. In figure 4.8 the parameters m_p, b_p and k_p represent respectively the piezoelectric element mass, damping and stiffness. The lumped parameter model in differential form is formulated as

$$m_p\ddot{x}_p(t) + b_p\dot{x}_p(t) + k_p x_p(t) = F_p(t) - F_{ext}(t), \tag{4.6}$$

where parameter m_p represents the piezoelectric mass, which is defined in [1] according to

$$m_p = \frac{4m_{piezo}}{\pi^2}. \tag{4.7}$$

The mass m_{piezo} is the weighted piezoelectric element mass. The difference $F_p - F_{ext}$ mechanically drives the piezoelectric element. Also a constant external force is necessary as a piezoelectric element is brittle in tension, and can only withstand tensile forces of a few Newton. This constant force will shift the elongation range without reducing it. Therefore, the initial values belonging to (4.6) are formulated as

$$\begin{aligned} \dot{x}_p(0) &= 0, \\ x_p(0) &= x_{p0}. \end{aligned} \tag{4.8}$$

As a piezoelectric element is most often used in a translation stage the combined mechanical behavior is discussed in more detail in the next section.

4.3 Piezoelectric Positioning Mechanism

Figure 4.9 shows a piezoelectric monolithic element incorporated in a translation stage. The parameters m_s, b_s and k_s represent respectively the stage mass and stage suspension damping and stiffness. The force F_0 represents the external constant force enforcing the initial offset x_{p0} on the stage position. In order to prevent tensile forces, the force F_0 should at least compensate for the gravitational force on mass m_s. In section 4.3.1 the quasi-static behavior of the translation stage is discussed more extensively and in section 4.3.2 a dynamical analysis and the relation to the electrical domain is discussed.

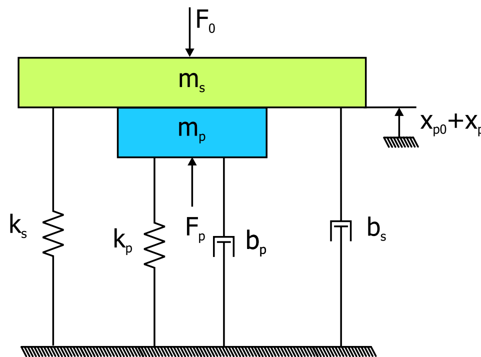

Figure 4.9: Schematic representation of a piezoelectric element incorporated in a translation stage.

4.3.1 Quasi-static Analysis

The mechanical relation for the quasi-static behavior, i.e. low frequency motion, for the translation stage given in figure 4.9 is described by

$$F_p(t) = (k_p + k_s)\, x_p(t), \tag{4.9}$$

with x_p the stage displacement, which equals the piezoelectric element elongation, and F_p the transduced force from electrical side. Herewith, the force working against the stage stiffness k_s is known as the effective transduced force F_p^{eff}. In product catalogs, such as [26], the maximum stage displacement $x_{p,max}$ is often given by

$$x_{p,max} = \left(\frac{k_p}{k_p + k_s}\right) x_{max}, \tag{4.10}$$

The free elongation x_{max} refers to the maximum attainable piezoelectric element elongation at the maximum recommended voltage level. When the piezoelectric element is completely free to deform ($k_s = 0$), the maximum stage displacement $x_{p,max}$ equals x_{max} and the effective transduced force equals zero. In a blocked configuration ($k_s \to \infty$) the effective transduced force equals the blocking force F_b, where the blocking force refers to the maximum attainable transduced force from electrical side at the maximum recommended voltage level. In product catalogs, the piezoelectric element stiffness k_p is specified in terms of the blocking force and the maximum free elongation according to

$$k_p = \frac{F_b}{x_{max}}. \tag{4.11}$$

The maximum free elongation is a function of the total piezoelectric element length and can be increased by lengthening the element whereas the blocking force can be increased by scaling-up the width and height. As mentioned before, using stacks only lowers the input voltage level while the performance is maintained.

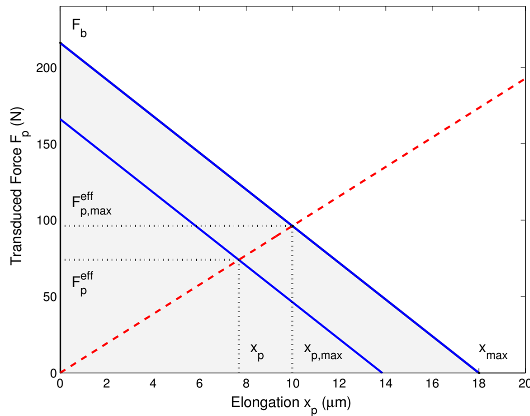

Figure 4.10: Motor-load characteristic for a monolithic piezoelectric stack element with $x_{max} = 18$ μm and $F_b = 216$ N (solid) acting against a stiffness $k_s = 9.6$ N/μm (dashed).

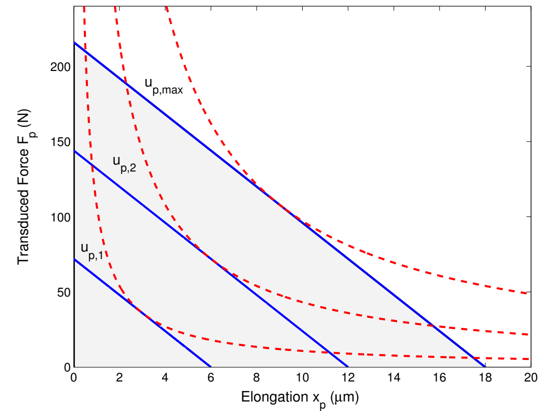

Figure 4.11: Characteristics for a monolithic piezoelectric stack element with $x_{max} = 18$ μm and $F_b = 216$ N for different voltage levels (solid), with $u_{p,max} > u_{p,2} > u_{p,1}$. Also corresponding lines of constant work are shown (dashed).

The interaction of the stage stiffness k_s and the piezoelectric element stiffness k_p is schematically shown in figure 4.10, by means of a motor and load characteristic. Such characteristics are extensively used in the automotive industry to represent and analyze motor performances under different load conditions [30]. The motor characteristic relates in this case the transduced force and elongation of a piezoelectric element. The load characteristic represents the stage stiffness k_s. The reduction of the stage stiffness on the piezoelectric element elongation is directly seen in the working points, the points of intersection of the load and motor characteristic. At maximum voltage level the working point represents the maximum stage displacement $x_{p,max}$ and maximum effective transduced force $F_{p,max}^{eff}$. The shaded area in the figure represents the covered working area.

In figure 4.11 motor characteristics are given for different voltage levels. In the figure also lines are given of constant work, which is defined as the product of the effective transduced force and elongation. The maximum amount of work delivered by a piezoelectric element is found when the force is delivered at half its free elongation, and so when k_s equals k_p. It is noted that in automotive industry the characteristics relate torque and speed, and are therefore energy based. For piezoelectric elements the characteristics relate force and displacement and are therefore work based.

4.3.2 Dynamic Analysis

A good approximation for the dynamic behavior of a piezoelectric element is already given in (4.6). When observing a piezoelectric element incorporated in a translation stage this relation can be extended to

$$(m_p + m_s)\ddot{x}_p(t) + (b_p + b_s)\dot{x}_p(t) + (k_p + k_s)x_p(t) = F_p(t). \tag{4.12}$$

Again F_p is the transduced force from electrical side and x_p is the piezoelectric element elongation. The piezoelectric element stiffness, however, is much more complicated than the simple relation given in (4.11). The stiffness is in fact rather undefinable as one should distinguish stiffness for large and small signal conditions, static and dynamic operation and also for open and closed electrodes. In [1] and [9] open and closed electrodes are distinguished, which corresponds to respectively a charge steering configuration and a voltage steering configuration. For a charge steering configuration the transduced force F_p is obtained by combining (4.2) and (4.5). It follows that

$$F_p(t) = \frac{T}{C}\left(q_{in}(t) - Tx_p(t)\right). \tag{4.13}$$

Equating this relation to the second order differential equation given in (4.12), then it follows after rewriting for the relation between q_{in} and x_p, that

$$(m_p + m_s)\,\ddot{x}_p(t) + (b_p + b_s)\,\dot{x}_p(t) + \left(k_p^o + k_s\right)x_p(t) = \frac{T}{C}q_{in}(t). \tag{4.14}$$

The piezoelectric element stiffness is defined as

$$k_p^o = k + \frac{T^2}{C}. \tag{4.15}$$

The stiffness term k_p^o is known as the open electrode stiffness. The stiffness k is the piezoelectric material stiffness, defined by the modulus of elasticity, cross area and element length. The value for the linear capacitance C can be found in piezoelectric element specifications. The transformer ratio T, on the other hand, can only be measured. For an accurate value one should resort to a charge versus elongation or voltage versus force measurements.

In a voltage steering configuration the current can freely flow to electrically charge the element. As a consequence a lower piezoelectric element stiffness will be experienced. By using the generalized Maxwell model, as described in [9], the piezoelectric element stiffness is defined as

$$k_p^s = k + \frac{T^2}{C + C_m}, \tag{4.16}$$

where C_m is a so-called linearized Maxwell capacitor. As $C_m > 0$ it is obvious that the stiffness is larger with open electrodes. One is referred to Appendix B for a more detailed description on voltage steering and describing the corresponding hysteresis effect.

4.4 Discussion

In this Chapter piezoelectric actuation principles were discussed. The stacked monolithic piezoelectric element was found to be the best option for the T-ROM system, as it has good a performance and is compact. In order to predict and to gain an understanding of the piezoelectric element behavior, a piezoelectric element model was derived. A difference between charge steering and voltage steering was established. Originally, the intention was to use the model to really operate piezoelectric elements by voltage steering. For that purpose, in Appendix B, a start was made with modelling the hysteresis effect present in piezoelectric elements. In order to only demonstrate the system behavior, in this report charge control will be used because of its linearity. Furthermore, as the transformation ratio T could not be measured with the present setup, it will also be impossible to derive an accurate model for a voltage steering configuration. As a consequence, the piezoelectric element stiffness k_p will be approximated by the stiffness relation given in (4.11).

Chapter 5

Actuator Design

In the previous Chapters the basis actuator configuration and the type of actuation have been discussed. In this Chapter a three DOF actuator design, developed at Philips Research, is analyzed regarding its kinematic, static and dynamic behavior. First the actuator specifications are summarized in section 5.1. The conceptual design is shown in section 5.2 and is modelled and analyzed in section 5.3. Finally, in section 5.4 the analysis of the conceptual design is discussed and some recommendations for improvements are given.

5.1 Design Specifications

The system actuator design aims at an integrated focus actuation in a tangential and transversal scanning construction with a small construction height. The maximum dimensions of the actuator are based on the Compact Flash form factor with dimensions in length and width of respectively 36.5 mm and 42.8 mm. For a compact design, the construction height should be 3 mm at maximum. Uncoupled directions of motion are preferred in order to have independent piezoelectric elements. From a control point of view this means three independent controllers for the three independent directions of motions (three Single-Input-Single-Output systems). Recall that the required strokes are 13.4 μm in scanning direction and 30 μm in focusing direction. The corresponding required accuracies are in tangential direction ± 7.5 nm, in transversal direction ± 42 nm and in focus direction ± 140 nm. The rotational alignment of the storage medium is for further investigation and therefore not discussed here. It is noted that details such as the thermal center of construction and manufacturing fall outside the scope of work presented in this report.

5.2 Conceptual Design

In figure 5.1 a first proposal for a conceptual design of the in-plane actuator is shown. The xy positioning mechanism consists of two stacked stages with one and the same kind of flexure mechanism, and will be used to move the spots along the bits in either tangential or transversal direction. As mentioned before, the final decision whether x or y is in transversal or tangential direction will be made in Chapter 6. In each direction the flexure mechanism consists of four flexible hinges, which have a low bending stiffness in driving direction. In focus direction a third stacked stage with a similar flexure

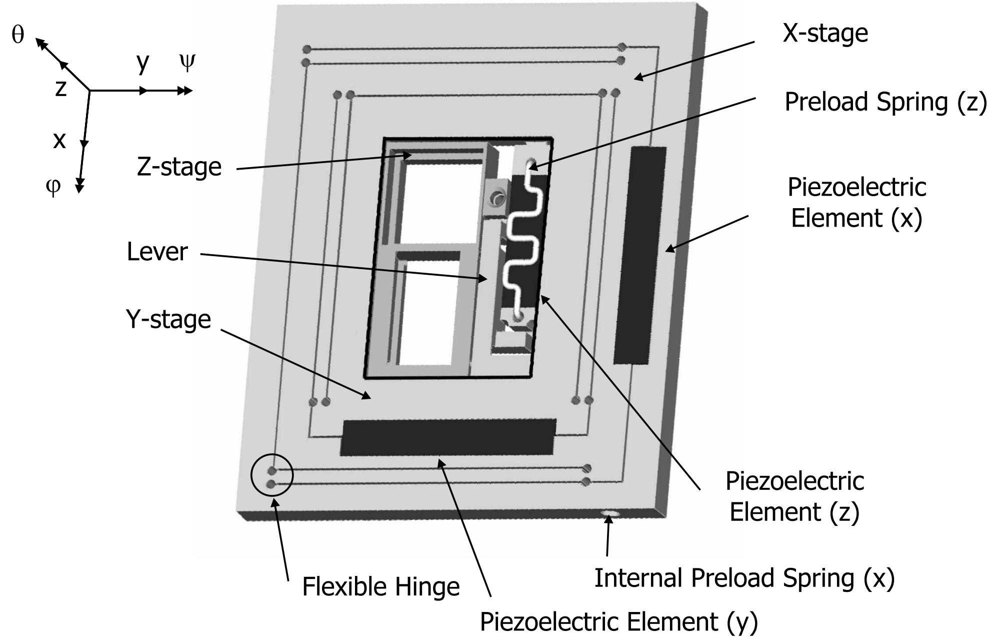

Figure 5.1: Conceptual design of the in-plane 3 DOF actuator. The x, y and z stages are each driven by a piezoelectric element.

mechanism is proposed. All stages are mounted orthogonally. An advantage of using flexible hinges is the absence of friction and play. A three degree of freedom probe generating element displacement is possible with the arrangement of piezoelectric elements as shown in the figure. To obey a small form factor in z direction the piezoelectric element drives the stage through a lever. This is shown in more detail in figure 5.2. This conceptual design with the three flexure systems stacked on top of each other satisfies the maximum dimensions of 36.5 x 42.8 x 3 mm^3.

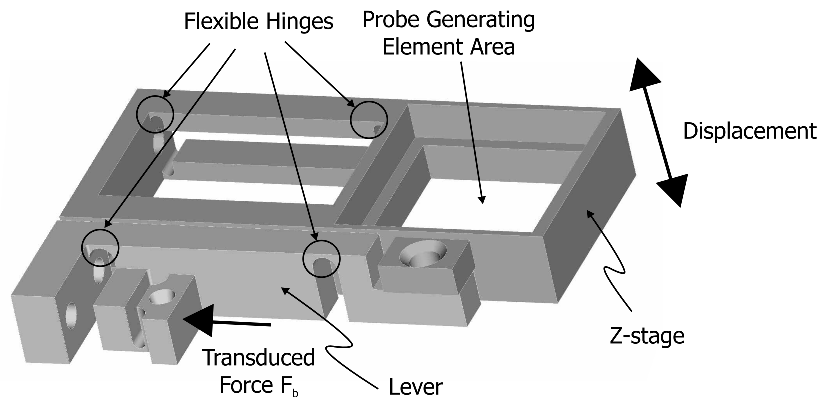

Figure 5.2: Highlighted z stage and lever of the conceptual design.

Table 5.1: Definitions of the actuator masses and stiffnesses of the x, y and z stage.

	mass [kg]	stiffness x direction [Nm^{-1}]	stiffness in y direction [Nm^{-1}]	stiffness in z direction [Nm^{-1}]
x stage	m_x	k_x^x	k_y^x	k_z^x
y stage	m_y	k_x^y	k_y^y	k_z^y
z stage	m_z	k_x^z	k_y^z	k_z^z

5.3 Modelling and Analysis

A simple dynamic model of the conceptual actuator design is given in figure 5.3. In this linear mass-spring model a distinction is made in the x, y and z direction. The masses are assumed concentrated stage masses and the stiffnesses are assumed concentrated in the flexures. Damping is not considered. Definitions for stage masses and stiffnesses in x, y and z direction are summarized in table 5.1. To link the stage and stiffness direction sub- and superscript (for example k_j^i) are introduced. The superscript i denotes the stage concerned and the subscript j denotes the observed stiffness direction. The transduced force from electrical side due to the piezoelectric effect is represented by F_{act}.

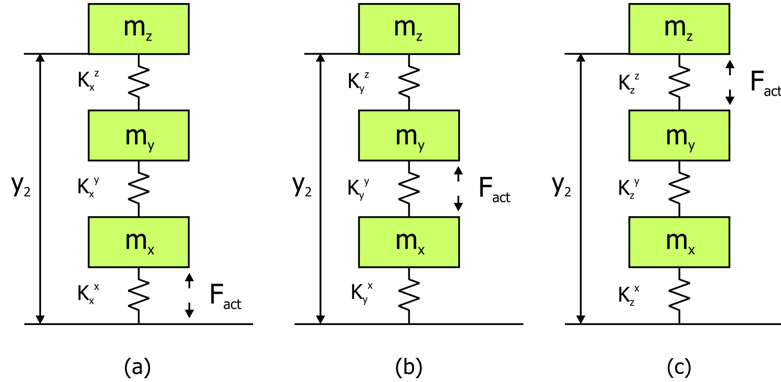

Figure 5.3: A dynamic model representation of the conceptual actuator design in x (a), y (b) and z (c) direction.

The main purpose of the stages is to restrict the displacement of the probe generating element to the direction into which it is driven. Displacements in the drive direction must be freely possible. However, the probe generating element guiding is limited by undesired parasitic motion, such as rotation and tilt. Therefore, in the sections 5.3.1 and 5.3.2 the parallel motion of each stage is analyzed. Further, in section 5.3.3 and 5.3.4, the dynamic and static behavior of the conceptual design is analyzed.

5.3.1 Imperfect Parallel Motion

The design is aimed at perfect parallel motions. To analyze the straightness and flatness of the flexure guiding systems in the conceptual design, the free body diagram for a general guiding system, as shown in figure 5.4, can be used. To bring this free body diagram in line with each stage the coordinate system transformations given in table 5.2 have to be used. For example for the z stage, the x, y and z

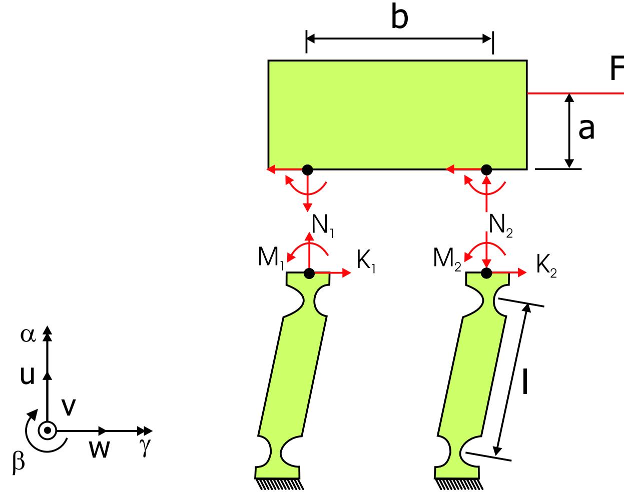

Figure 5.4: Free body diagram of a flexure mechanism. The interaction forces are denoted by N and K and the moment interaction is denoted by M.

directions denoted in figure 5.1 corresponds to respectively the $-u$, v and $-w$ direction in figure 5.5. For a movement over a relatively small stroke the normal forces N_1 and N_2 can be calculated from force and moment equilibrium. For N_1 and N_2 the results are

$$N_1 = -N_2 = \frac{F}{b}\left(\frac{l}{2} + a\right). \tag{5.1}$$

A derivation is given in Appendix C. In case the point of application of the force F is at half the flexure length $\left(a = -\frac{l}{2}\right)$ the normal forces are zero and results in a parallel movement in the vw plane. In all other cases non-zero normal forces will be obtained. As N_1 and N_2 act in opposite direction this will affect the parallel movement as it will result in a body rotation in β rotation. After rewriting (5.1) the body rotation $\Delta\beta$ can be given as a function of stroke length Δw according to

$$\Delta\beta = 3.04\left(\frac{h}{bl}\right)^2\left(\frac{l}{2} + a\right)\Delta w. \tag{5.2}$$

The derivation is given in Appendix C and the parameters are defined in figure 5.5. When applying a stroke Δw, a second parasitic motion δ in u direction is expected, as is shown in figure 5.5. However, this parasitic motion is only on the order of nanometers and furthermore, such a parasitic motion can easily be compensated by one of the other two stages in the conceptual design, as the stages are mounted orthogonally. The body rotation in β rotation, on the other hand, is in an uncontrolled direction.

Table 5.2: Coordinate system transformations.

	x direction	y direction	z direction
x stage	w	u	v
y stage	u	$-w$	v
z stage	$-u$	v	$-w$

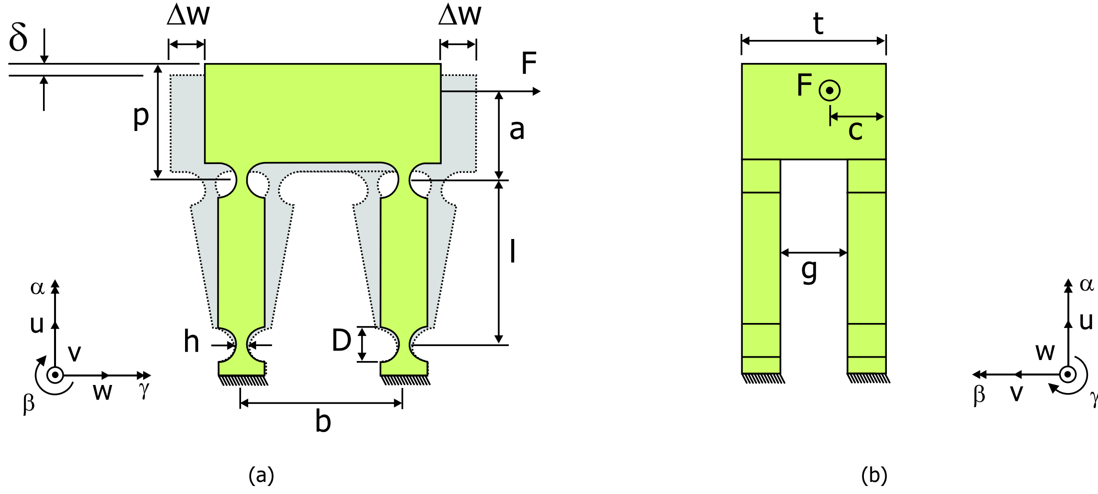

Figure 5.5: Schematic representation of a parameterized flexure mechanism: front view (a) and side view (b).

With the estimated values given in table 5.3, the rotation of the x, y and z stage can be calculated. For the x and y stage this results in an angular rotation of less than 0.2 μrad. For the z stage the rotation is approximately 45 μrad. Compared to the accuracy margins given in table 3.1, of respectively 2 μrad and 39 μrad, the straightness and flatness in the focus direction is therefore the most critical. Moreover, the straightness and flatness in the focus direction becomes even more critical as the point of application of the applied force in the proposed actuator design is not centrally in the thickness direction (i.e. $c = 0$). For the flexure mechanism shown in figure 5.5, a rough estimate of the body rotation in α direction is derived in Appendix C and is given by

$$\Delta\alpha \approx 1.86 \left(\frac{Dh}{l^2t^2}\right)\left(\frac{t}{2} - c\right)\Delta w. \tag{5.3}$$

It is noted that relation (5.3) is only valid if the condition $D/h \gg 1.2$ is met. Observing the z stage and by using the parameters given in table 5.3, the body rotation $\Delta\alpha$ is 67 μrad and therefore fairly exceed the required accuracy level of 39 μrad with it. In order to get more insight in the movement in focus direction, and how it should be adapted such that the requirements are obtained, it will be analyzed further with a finite element approach. This is discussed in the next paragraph.

Table 5.3: Initial parameter values for the parameterized flexure mechanism shown in figure 5.5.

Parameter	a [mm]	b [mm]	c [mm]	g [mm]	h [mm]	l [mm]	p [mm]	t [mm]	D [mm]	Δw [μm]
x stage	0	30	1.5	0	0.4	25	5	3	1.2	$\frac{13.4}{2}$
y stage	0	25	1.5	0	0.4	20	5	3	1.2	$\frac{13.4}{2}$
z stage	0	3	0	0	0.4	10	8	8	1.2	$\frac{30}{2}$

5.3.2 Static Finite Element Analysis

A finite element analysis is used to illustrate the functional performance of the movement in focus direction more accurately. In the analysis the analytic solution of the algebraic equations, describing the behavior of a stage, is approximated by using a finite element method. For implementation the finite element analysis software MSC.Marc/Mentat is used. The corresponding finite element model is shown in figure 5.6. This model is programmed in a script and parameterized in analogy with the flexure mechanism shown in figure 5.5. The script program flexibility is valuable as it easily enables dimensioning of the model. The corresponding model material property is assumed isotropic and linear elastic. In case of iron the modulus of elasticity is $2.1 \cdot 10^{11}$ Mpa, Poisson's ratio is selected 0.3 and the material density is 7850 kg/m^3.

Crucial in the quality of the approximation of the mechanisms behavior is the mesh generation. Especially around the flexible hinges, as here the largest stresses and material deformations are to be expected. For the model shown in figure 5.6, the mesh is generated manually, as 3-dimensional automatic mesh generation is not available. The influence of the mesh coarseness on the accuracy of the solution is examined first. This is done by repeatedly refining the mesh as long as convergence of the solution happens. The resulting mesh is shown in figure 5.6. For even more accurate results an automatic local mesh adaptivity is applied at the flexible hinges.

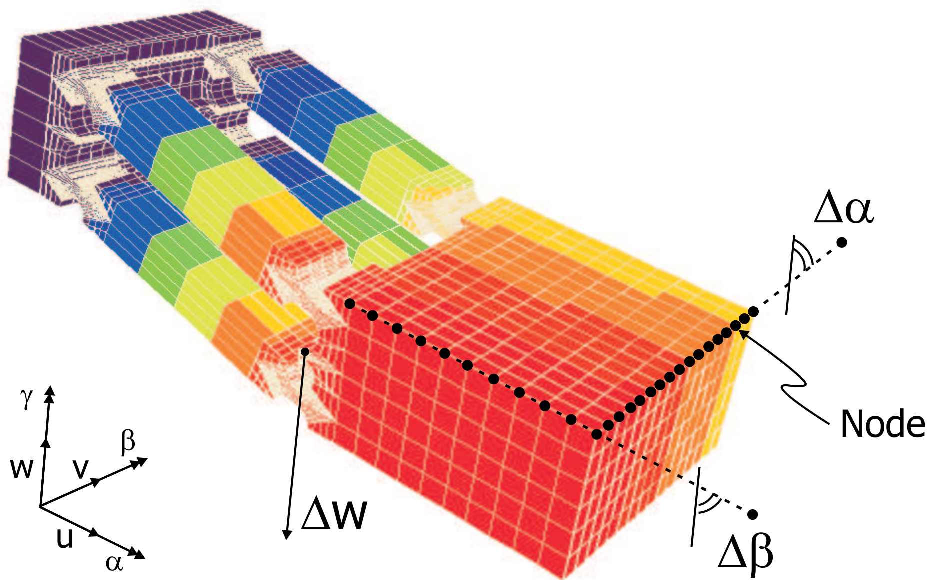

Figure 5.6: Finite element model of the z stage.

Now the model can be used to examine both the angular body rotations $\Delta\alpha$ and $\Delta\beta$. A static situation is considered. The maximum angular body rotations $\Delta\alpha$ and $\Delta\beta$ are calculated as a function of an applied stroke Δw. In the focus direction the stroke is 15 μm and in scanning direction the stroke is 6.7 μm. The body rotations $\Delta\alpha$ and $\Delta\beta$ are determined in the post processing part of the finite element analysis software by processing a so-called path plot. With a path plot the displacement of nodes of the generated mesh, along a selected path, can be plotted as function of the path length. The selected paths are shown in figure 5.6. From the path length and corresponding difference in minimum and maximum displacement the body rotation is calculated.

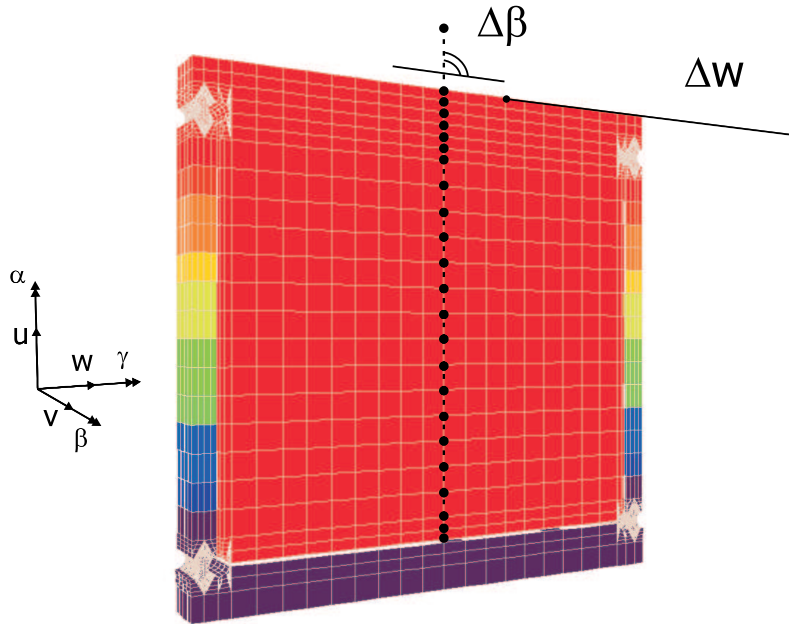

Figure 5.7: Finite element model of the x stage.

Different parameter value configurations are considered. Initially, the values for the z stage given in table 5.3 are used. By using the finite element model the body rotations $\Delta\alpha$ and $\Delta\beta$ are respectively 244 μrad and 77 μrad. To obtain the sensitivity to parameter variation, i.e. parameters b, l, a, g, D and h, all parameter are kept constant while only one parameter is varied. For the α rotation the results are summarized in figure 5.8. For the β rotation the results are summarized in figure 5.9. In these figures also the maximum tilt belonging to a focus accuracy margin of ± 280 nm and ± 140 nm is indicated, respectively being 77 μrad and 39 μrad. Notable is the correspondence in β direction of the simulation results with the body rotation relation given in (5.2). The rotation has a quadratic relation with parameters b and h, parameters a and l behave almost linearly with $\Delta\beta$ and parameter D does not influence the angular body rotation. Remarkable is the fact that a slightly negative rotation is obtained for large values of parameter b. Most likely, this is due to model imperfections. Although in α direction the simulation results are also related to the relation given in (5.3), they are less obvious.

From the figures it can be seen directly that for the initial values the body rotation $\Delta\beta$ and $\Delta\alpha$ both exceed the accuracy margin. Further, the body rotation $\Delta\beta$ is far smaller that the body rotation $\Delta\alpha$. The body rotation in β direction satisfies the requirements only if $h \leq 0.2$ mm. On the other hand, the parameter h can not be adjusted such that also the body rotation α satisfies the requirements. For a satisfied $\Delta\alpha$ body rotation one should focus on increasing the actuator thickness by means of enlarging the dimension for parameter b. However, in case of the z stage, parameter b corresponds to the actuator construction height. Limiting the construction height, in turn, is exactly the challenge of the actuator design. Therefore, this is discussed further in section 5.4.

The movement of the x stage, on the contrary, does not exceed the accuracy margin, as was already expected from a rough estimate. A finite element model of the x stage only is shown in figure 5.7. The parameter estimates given in table 5.3 lead up to a body rotation $\Delta\beta$ of 0.2 μrad, and this amply satisfies the maximum required body rotation condition of 2.0 μrad. The rotation of the y stage is not investigated separately. Motivated by de fact that in x direction the body rotation is of an order lower than the requirement, it is expected that the rotation of the y stage is also within the accuracy margin.

5.3.3 Dynamic Behavior

The proper functioning of the actuator is also determined by the parasitic resonances. Resonances in a controlled direction can be effectively suppressed but, in parasitic directions, possible vibration modes can not be attenuated. Vibration modes are induced by reaction forces due to accelerations of the actuator mass. The reaction forces propagate through the entire construction and can cause vibrations of large amplitudes, being the property of a mechanical resonance frequencies. To avoid vibration modes in the construction, the mechanical resonances should have frequencies large enough to exceed the frequency components present in the accelerations.

For a rough estimate of the lowest resonance frequency of the conceptual actuator design, also called the first eigenfrequency, the mass-spring representation given in figure 5.3 is used. Estimates for the masses are given in table 5.4. As the three masses are of the same order of magnitude, the first eigen-

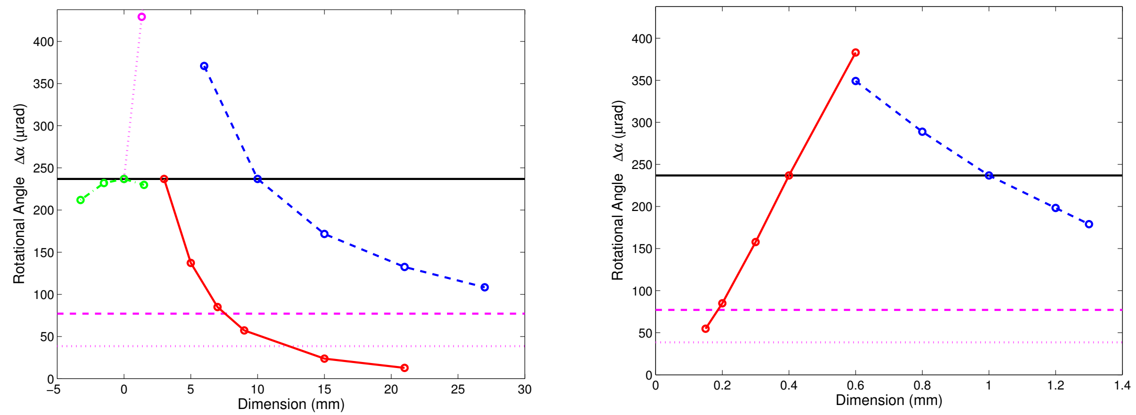

Figure 5.8: Angular body rotation $\Delta\alpha$ for initial values (solid), focus depth (dashed), accuracy margin (dotted), and for variation of different parameters: Left figure: b (○ solid), l (○ dashed), a (○ dash-dotted), g (○ dotted), Right figure: h (○ solid), D (○ dashed).

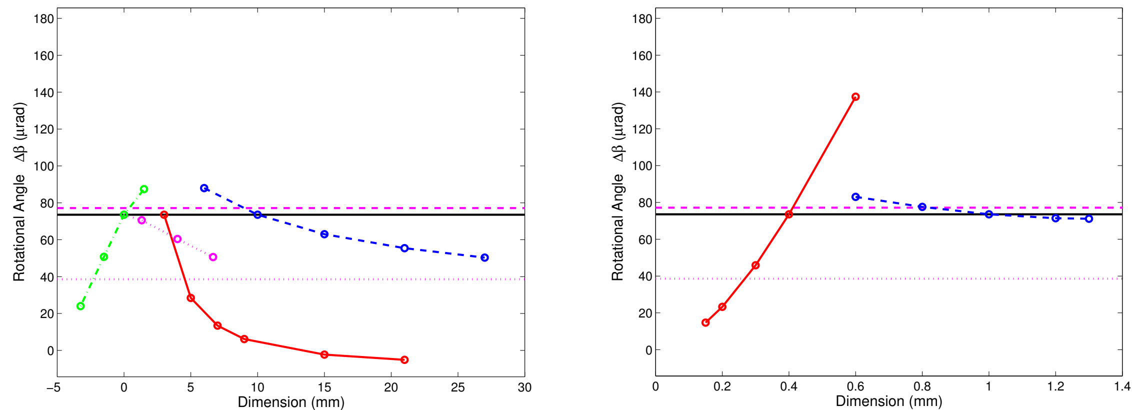

Figure 5.9: Angular body rotation $\Delta\beta$ for initial values (solid), focus depth (dashed), accuracy margin (dotted), and for variation of different parameters: Left figure: b (○ solid), l (○ dashed), a (○ dash-dotted), g (○ dotted), Right figure: h (○ solid), D (○ dashed).

Table 5.4: Values for the actuator masses and stiffnesses.

	mass 10^{-3}[kg]	stiffness x direction [Nm^{-1}]	stiffness in y direction [Nm^{-1}]	stiffness in z direction [Nm^{-1}]
x stage	9	k_x^x	$k_y^x = 3.3 \cdot 10^3\ k_y^y$	$k_z^x = 1.4\ k_z^z$
y stage	7	$k_x^y = 5.1 \cdot 10^3\ k_x^x$	k_y^y	$k_z^y = 2.2\ k_z^z$
z stage	3	$k_x^z = 1.4 \cdot 10^4\ k_x^x$	$k_y^z = 1.8 \cdot 10^3\ k_y^y$	k_z^z

frequency is expected in the direction with the lowest stiffness. The stiffnesses can be calculated by observing the flexure mechanism shown in figure 5.5, as this flexure mechanism represents each stage, and by using the parameter values given in table 5.3. For the purpose to calculate the stiffness of the flexure mechanism, in u, v or w direction, two flexible hinges acting in series are considered. Now the stiffnesses can be calculated by using the flexible hinge definitions given in Appendix C. In the controlled directions it follows for the stiffnesses that

$$\begin{aligned} k_x^x &= 3.4 \cdot 10^4 \quad \text{N/m}, \\ k_y^y &= 5.3 \cdot 10^4 \quad \text{N/m}, \\ k_z^z &= 5.7 \cdot 10^5 \quad \text{N/m}. \end{aligned} \tag{5.4}$$

It is noted that the piezoelectric element stiffness is omitted in the calculations. Further, the calculated stiffnesses in uncontrolled directions are summarized in table 5.4. For each direction the calculated stiffnesses are normalized to the controlled stage. The lowest stiffness, in an uncontrolled direction, is expected to be in the combined x and y stage in z direction. The estimated stiffnesses k_z^x and k_z^y are respectively $8.0 \cdot 10^5$ N/m and $1.3 \cdot 10^6$ N/m.

Figure 5.10: Finite Element Model of the x and y stage showing the lowest eigenfrequency at 666 Hz with movements in z directions.

The dynamical behavior of the combined x and y stage can be calculated accurately and made visible by using a finite element method. For that purpose, the combined x and y stage is modelled in MSC.Marc/Mentat. For reasons of complexity, the z stage is not included in the model and the piezoelectric elements are omitted. Again the initial parameter estimates given in table 5.3 are used to dimension the model and also the mesh is adapted as long as convergence of the solution happens. The first vibration mode occurs at a frequency of 666 Hz and is shown in figure 5.10. The corresponding out of plane deflection is clearly noticeable. It should be noted that the figure only illustrates the shape of the vibration mode, an indication of the scale is not included. Higher vibration modes (the second and third) are shown in figures D.1 and D.2 in Appendix D. The corresponding eigenfrequencies are respectively 863 Hz and 1090 Hz.

5.3.4 Driving Mechanism

In figure 5.3 the stages are driven by an actuator force F_{act}. This force originates from the piezoelectric element but is transferred in a more complicated way. For instance, the lever included in the focus direction introduces new dynamics in the system, making the static and dynamic behavior more complex. Another aspect is the interface between the piezoelectric element and stage. In the translation stage shown in figure 4.9 no interface was supposed. As the piezoelectric element should be under all conditions in the same place in the actuator design, it therefore should be fixed at all times. By applying an adhesive layer, however, one introduces additional stiffness. A third aspect is, that as a piezoelectric material is brittle in tension and therefore it cannot withstand pulling forces, a preload force is required. Combining these three aspects, the piezoelectric driven stage can be represented by the dynamic model given in figure 5.11. In fact, this model is an enhanced version of the simple piezoelectric driven translation stage model given in figure 4.9. The lever mass is represented by m_a and m_b and the lever stiffness by k_i. The lever magnification ratio is given to be i. The interface stiffness is denoted by k_g and the required preload force for the piezoelectric element is enforced through the spring with stiffness k_v. For a derivation of this model one is referred to Appendix E.

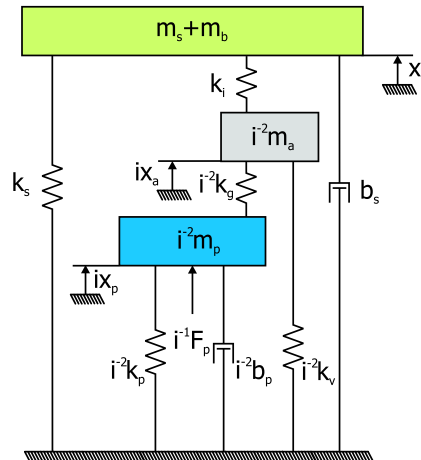

Figure 5.11: A stage representing a controlled direction of the conceptual actuator design.

However, the interface stiffness k_g is still assumed rigid, as due to surface roughness, Hertzian contacts are to be expected. One only should check for too large contact stresses causing failure. In general, the larger the contact area the smaller the contact stresses. A Hertzian contact stress analysis is proposed in [10], but here simply no failure is assumed. Using an adhesive the rigidly assumed interface condition is valid as long as the adhesive does not affect the Hertzian contacts. This is plausible as the

adhesive layer only should prevent shear effects and should not have any strength in tension, as it is subjected to a preload compression force. Therefore, the adhesive can be applied within the surface roughness. This puts a severe strain on the manufacturing technology but should theoretically be possible. The assumption can be relaxed by using piezoelectric elements with round heads. A condition to the assumption is an adhesive with a proper viscosity and shear strength. More information on adhesives and application techniques can be found in [20].

Further, the function of the preload spring is to avoid mechanical stress in the piezoelectric element, by means of an enforced offset. For an externally applied shock, with an amplitude of 6 g and acting on a mass of $19 \cdot 10^{-3}$ kg, a force of approximately 1.1 N has to be exerted to overcome the spring stiffness. The corresponding required spring deflection is determined by the spring stiffness. For simplicity all springs in the conceptual design are assumed iron helical compression springs, although figure 5.1 suggests a different spring design in z actuation. Iron helical compression springs are described in [10]. The spring stiffness is defined by

$$k_v = \frac{Gd}{8CN_a}. \tag{5.5}$$

Parameter G is the spring material shear modulus and is 80 GPa, d represent the wire diameter and is assumed to be 0.3 mm. Further, the spring index C and number of active coils N_a are typically 6 and 12 respectively. This results in a value for k_v of $1.3 \cdot 10^3$ N/m. To exert a force of 1.1 N at least a spring deflection of 0.9 mm should be applied. A third stiffness in the stage is the lever stiffness k_i. Suppose a lever with modulus of elasticity E_y, width l_w, height l_h and amplification ratio $i = \frac{l_b}{l_a}$. Here l_a and l_b are the lever arm lengths. By using uniform beam theory the stiffness k_i can be approximated by

$$k_i = \frac{E_y l_w l_h^3}{4 l_a^3 i^2 (1+i)}. \tag{5.6}$$

A derivation of this relation can be found in Appendix E. The corresponding lumped lever masses m_a and m_b can be given as function of the lever geometry according to

$$m_b = i m_a = i \frac{\rho l_a l_w l_h}{3}. \tag{5.7}$$

The parameter ρ represents the lever material density.

Table 5.5: Piezoelectric element options available in [26].

	Length 10^{-3} [m]	k_p [N/μm]	m_p 10^{-4} [kg]	x_{max} [μm]
Option 1	9	12	1.7	8
Option 2	11	16	2.0	10.5
Option 3	13.5	20	2.5	13
Option 4	18	24	3.4	18

With the definitions and assumptions for stiffnesses k_g, k_v and k_i the controlled directions of the conceptual actuator design can be analyzed further. The preliminary estimates of the corresponding stage stiffnesses k_s are already defined in (5.4). The stage masses m_s can be determined from the actuator model shown in figure 5.3, by combining m_x, m_y and m_z, and by using table 5.4. What remains are the lever amplification ratio i and the final choice of the piezoelectric element parameters. The options for piezoelectric element are listed in table 5.5.

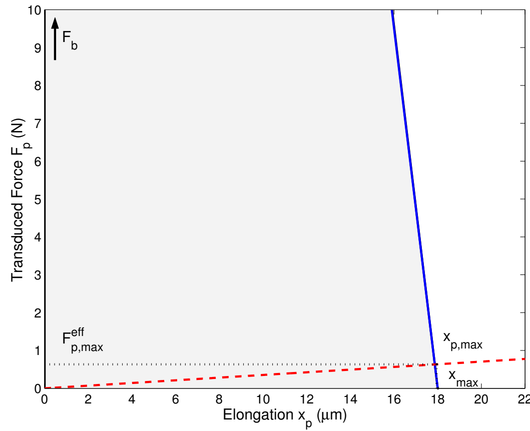

Figure 5.12: Motor-load characteristic for the x direction of the conceptual actuator design.

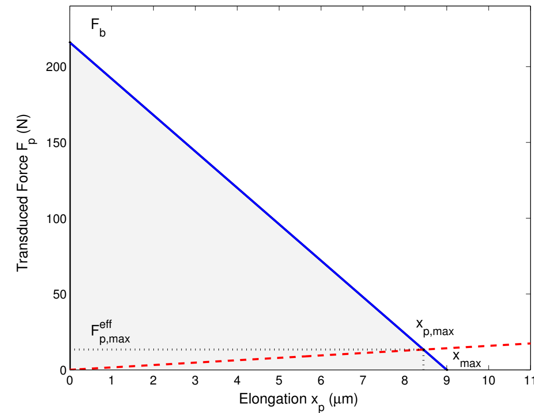

Figure 5.13: Motor-load characteristic for the z direction of the conceptual actuator design.

First the x and y stage is analyzed. In both stages no lever is included and therefore $k_i = \infty$ and $i = 1$. Therefore, in order to obtain a stage displacement of 13.4 μm, only piezoelectric element option 4 is appropriate to use. The corresponding motor-load characteristic for the x stage is given in figure 5.12. Secondly, for the z stage both the piezoelectric element and lever amplification ratio are undefined. A combination of both should be considered. The criterion used for the final choice for both is based on compact design and optimal work. This means that a small piezoelectric element is preferred and that the elongation x_p should best be accompanied with an effective transduced force F_p^{eff} as large as possible. The only condition is a stage displacement x_s of 30 μm. By using the relations given in section E.2 of the Appendix, for specific combinations of i and k_p the maximum attainable stage displacement can be calculated. The results shown in figure 5.14 show that for $k_s = 5.7 \cdot 10^5$ N/m piezoelectric element option 4 is required. As this option is not compact compared to the other options,

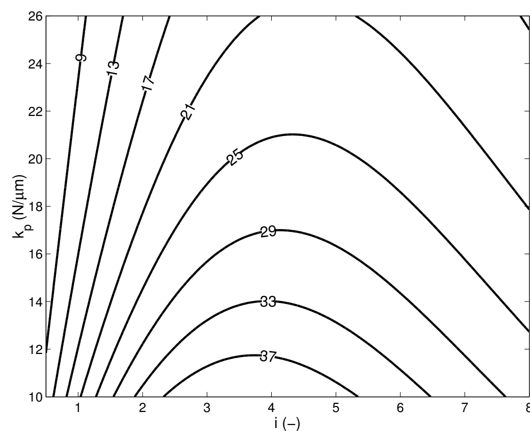

Figure 5.14: Piezoelectric element stiffness versus lever amplification ratio for $k_s = 5.7 \cdot 10^5$ N/m and resulting $x_{s,max}$ (solid), with $x_{s,max}$ given in μm.

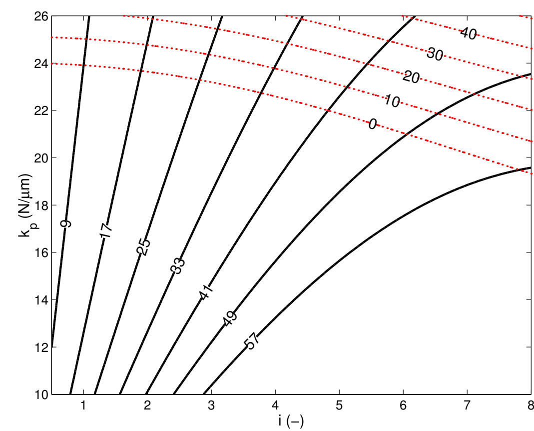

Figure 5.15: Piezoelectric element stiffness versus lever amplification ratio for $k_s = 1.0 \cdot 10^5$ N/m and resulting $x_{s,max}$ (solid) and effective transduced fore F_p (dashed), with $x_{s,max}$ given in μm and F_p given in N.

the stage stiffness k_s is assumed $1.0 \cdot 10^5$ N/m, which corresponds to a z stage with parameter $h = 0.2$ mm. Again calculations are performed. The results are shown in figure 5.15. In this figure also the effective transduced force is shown. The results lead to piezoelectric element option 1, accompanied with a lever amplification ratio of 4. The corresponding motor-load characteristic is given in figure 5.13. It is noted that for the calculations the lever dimensions l_h, l_a and l_w are assumed respectively 3, 3 and 4 mm.

5.4 Discussion

In this chapter the proposed conceptual actuator design was analyzed with respect to its kinematic, static and dynamic behavior. The challenge of the design was the integrated focus actuation in a compact construction with a height of 3 mm. In section 5.3.1 motion errors of a standard flexure mechanism were analyzed, which represents the stages in the design. The motion errors, especially parasitic rotations, occurred as soon as a stage is displaced. The larger the stroke the larger the error. The z stage was especially found sensitive for motion errors. With the help of the finite element software MSC.Marc/Mentat, more insight in the movement in focus direction was obtained. For the z stage it was concluded that the rotation in α direction was too large, and can not be reduced enough by simply dimensioning the stage. On the other hand, the β rotation would satisfy the requirements by simply adjusting the flexible hinge parameter h to 0.2 mm.

The rotation in α direction can be eliminated by an alternated design. Therefore, the point of application of the force, which drives the stage, should be central in the stage thickness direction. For the schematic representation shown in figure 5.5 this means that the point of application of the force F should be at $c = t/2$. For this newly obtained configuration already finite element simulations have been performed. The results for the rotation in β direction are shown in figure 5.4. The difference with the rotation in β direction in the old configuration (i.e. $c = 0$) is minimal.

Also the dynamical behavior of the conceptual actuator design was analyzed. In section 5.3.3 the first, and limiting, vibration mode was shown. This vibration mode was in an uncontrolled direction and

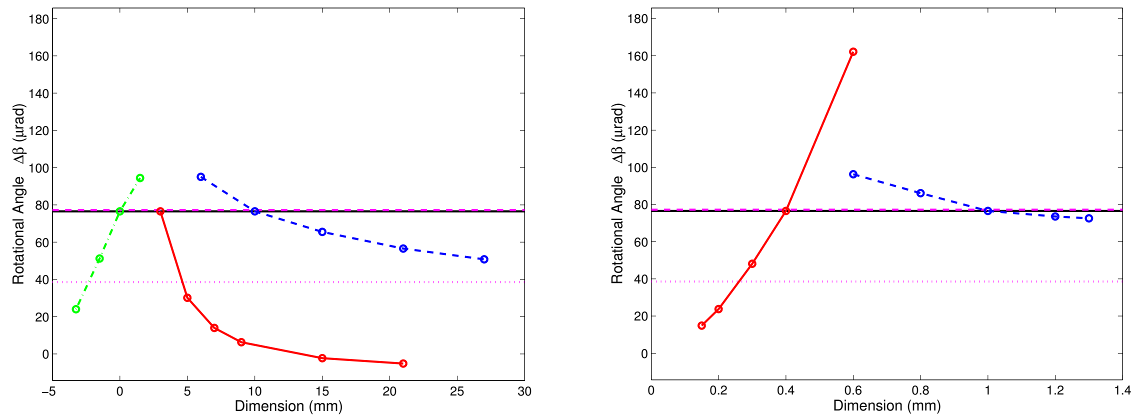

Figure 5.16: Angular body rotation $\Delta\beta$ in the new configuration for initial values (solid), focus depth (dashed), accuracy margin (dotted), and for variation of different parameters: Left figure: b ($\circ$ solid), l ($\circ$ dashed), a ($\circ$ dash-dotted), g ($\circ$ dotted), Right figure: h ($\circ$ solid), D ($\circ$ dashed).

Table 5.6: Summarized parameters of the stage shown in figure 5.11 for each actuation direction.

	i	k_p	k_s	k_g	k_v	k_i	m_p	m_s	m_a	m_b
	[-]	10^6[Nm^{-1}]	10^4[Nm^{-1}]	[Nm^{-1}]	10^3[Nm^{-1}]	10^6[Nm^{-1}]	10^{-4}[kg]	10^{-3}[kg]	10^{-4}[kg]	10^{-4}[kg]
x direction	1	12	3.4	∞	1.3	∞	3.4	19	-	-
y direction	1	12	5.3	∞	1.3	∞	3.4	10	-	-
z direction	4	24	10.0	∞	1.3	∞	1.7	3	2.1	8.4

had a resonance frequency of 666 Hz. In section 6.2 it will be seen that the expected external mechanical disturbances contain frequency components in the range up to 1000 Hz. Therefore, also the second vibration mode is expected to be excited. Most effective in increasing te resonance frequency is increasing the actuator construction height, as increasing the construction height will increase the out of plane stiffness most effective. However, this contradicts the challenge to construct an actuator with a small construction height.

In section 5.3.4 the static performance of the design was analyzed on the basis of the dynamic model shown in figure 5.11. The analysis has resulted in a final choice for the piezoelectric element and lever amplification ratio. For that purpose many assumptions on stiffnesses have been made. In general, in order to obtain the most effective maximum stage displacement, the bending stiffness of the stage k_s and also the preload spring stiffness k_v should best be as low as possible. On the other hand, the interface stiffness k_g and the lever stiffness k_i should both best be as large as possible. Otherwise, one should compensate for the reduction in displacement by changing the lever amplification ratio i and piezoelectric element k_p. Reduction in displacement may become an issue in case other materials as iron are used, such as plastics for example.

In the next Chapter the actuator will be assumed integrated in a casing, for example in a mobile phone casing. In order to proceed, assumptions about the actuator design are made. First of all, the construction height b is kept at 3 mm. Further, for the z stage, the point of application of the force is assumed central in the stage thickness direction ($c = t/2$) and the hinges are assumed optimized ($h = 0.2$ mm). As a consequence, the stage bending stiffness k_s equals $1.0 \cdot 10^5$ N/m. Furthermore, in z direction, the lever is assumed rigid. Finally, all parasitic motions are neglected and only the motion in the controlled x, y and z directions will be observed. This means that the actuator has three uncoupled directions of motion, each driven by an independent piezoelectric element. All values, which will be used for further analysis, are once more summarized in table 5.6.

Chapter 6

System Modelling

In order to evaluate the T-ROM system performance, the 3 DOF actuator is assumed to be integrated in a casing, for example, a mobile phone casing. Only the controlled directions are concerned. In order to describe the dynamic system behavior in section 6.1 a mathematical model is derived. In section 6.2 the frame suspension is considered in more detail. Finally, in section 6.3, the overall system dynamics is discussed.

6.1 Linear Dynamic System Representation

The T-ROM positioning system is modelled as a mass-spring-damper system describing the linear behavior of the system in tangential and transversal direction (either being x or y direction) and the focus (z) direction as well. It is assumed that the image sensor and storage medium are rigidly attached to the frame and therefore, besides the position of the frame in the casing, only the position of the probe generating element compared to the frame is concerned. The mass-spring-damper system is shown schematically in figure 6.1 and shows the system in one dimension. It is used to represent the system in all three directions, either in tangential, transversal or focus direction.

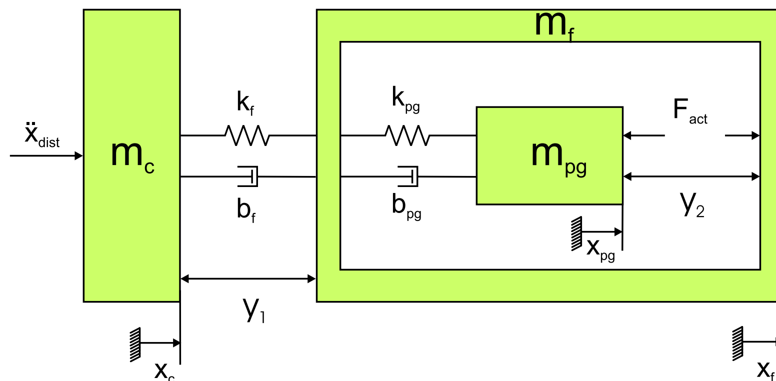

Figure 6.1: Schematic one-dimensional mass-spring-damper representation of the system.

Referring to figure 6.1, the system has two inputs. The actuation force is denoted by F_{act} and the to be expected disturbance accelerations on the casing are denoted by $\ddot{x}_{dist}$. These disturbance accelerations are discussed in more detail in the next section. The position of the casing, the frame and the probe generating element are denoted by respectively x_c, x_f and x_{pg}. Equating the sum of forces to the mass accelerations (Newton's Second Law) the one-dimensional equations of motion are given by

$$\begin{aligned} m_c\ddot{x}_c &= k_f\left(x_f - x_c\right) + b_f\left(\dot{x}_f - \dot{x}_c\right) + m_c\ddot{x}_{dist}, \\ m_f\ddot{x}_f &= k_{pg}\left(x_{pg} - x_f\right) + b_{pg}\left(\dot{x}_{pg} - \dot{x}_f\right) - k_f\left(x_f - x_c\right) - b_f\left(\dot{x}_f - \dot{x}_c\right) - F_{act}, \\ m_{pg}\ddot{x}_{pg} &= F_{act} - k_{pg}\left(x_{pg} - x_f\right) - b_{pg}\left(\dot{x}_{pg} - \dot{x}_f\right). \end{aligned} \tag{6.1}$$

It should be noted that the time dependency of the positions is omitted for the sake of clarity. The mass constants m_c, m_f and m_{pg} represent respectively the mass of the casing, frame and the probe generating element (with m_c large compared to m_f and m_f large compared to m_{pg}). Further, k_f and b_f represent the spring and damper constants of the frame suspension, whereas the probe generating element and frame are coupled through stiffness k_{pg} and damping b_{pg}. In terms of an undamped natural frequency ω_n and a damping ratio β for frame and probe generating element suspension it applies respectively that

$$\begin{aligned} \omega_{n_f}^2 &= \frac{k_f}{m_f} \quad \text{and} \quad 2\beta_f\omega_{n_f} = \frac{b_f}{m_f}, \\ \omega_{n_{pg}}^2 &= \frac{k_{pg}}{m_{pg}} \quad \text{and} \quad 2\beta_{pg}\omega_{n_{pg}} = \frac{b_{pg}}{m_{pg}}. \end{aligned} \tag{6.2}$$

The probe generating element mass, damping and stiffness parameters are defined as functions of the parameters used in the previous chapter and are summarized in table 6.1 for each actuation direction. A derivation of the relations is given in Appendix E. The mass and stiffness parameter values are given in table 5.6. As damping parameter values are not available the probe generating element damping ratio β_{pg} is assumed to be 50%. Further, the masses for casing and frame are assumed to be 0.4 and 0.1 kilogram respectively. Finally, the damping and stiffness parameters of the frame will be discussed in the next section.

Table 6.1: Actuation force and probe generating element mass and suspension definition.

	m_{pg} [kg]	b_{pg} [Nsm^{-1}]	k_{pg} [Nm^{-1}]	F_{act} [N]
x direction	$m_x + m_y + m_z + m_p$	$b_s + b_p$	$k_s + k_p + k_v$	F_p
y direction	$m_y + m_z + m_p$	$b_s + b_p$	$k_s + k_p + k_v$	F_p
z direction	$m_z + m_b + i^{-2}(m_a + m_p)$	$b_s + i^{-2}b_p$	$k_s + i^{-2}(k_p + k_v)$	$i^{-1}F_p$

Because of its linearity, charge control is considered to demonstrate the system behavior. The relative positions $y_1 = x_f - x_c$ and $y_2 = x_{pg} - x_f$ are defined as system outputs. Output y_2 is the output of main interest as it describes the relation of the probe generating element to the storage medium. At all times this position should be kept at a reference level. Output y_1 is also monitored as physically this position should be realistic, and therefore not exceed 0.5 mm. The piezoelectric element stiffness k_p will be approximated by the stiffness relation given in (4.11), as the transformation ratio T could not be measured with the present setup.

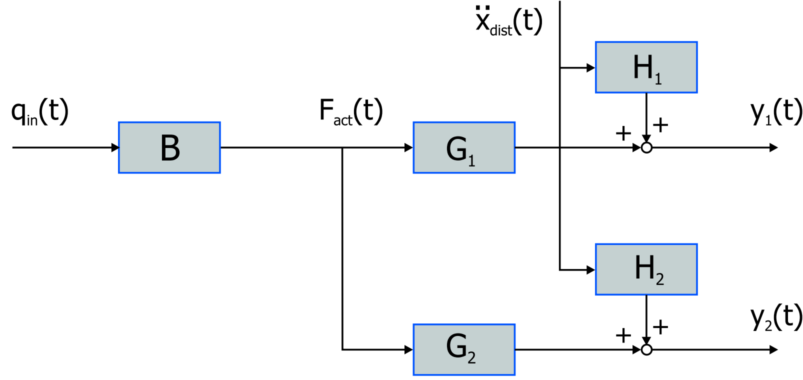

Figure 6.2: Block diagram of the open loop system.

In terms of system transfer functions the linear system behavior is described by

$$
\begin{aligned}
Y_1(s) &= G_1(s)F_{act}(s) + H_1(s)s^2X_{dist}(s), \\
Y_2(s) &= G_2(s)F_{act}(s) + H_2(s)s^2X_{dist}(s).
\end{aligned}
\tag{6.3}
$$

The variable s is the Laplace variable and $Y_1(s)$ and $Y_2(s)$ are the Laplace transforms of respectively $y_1(t)$ and $y_2(t)$. The transfer functions describing the relation between the actuator force F_{act} and the positions y_1 and y_2 are denoted by G_1 and G_2 respectively. The transfer functions H_1 and H_2 denote the influence of the disturbance input on the positions y_1 and y_2. The discussed input-output relations are shown in the block diagram of figure 6.2 and are derived in Appendix F. The actuator force F_{act}, in turn, is assumed proportional to the applied charge q_{in} by a factor B. This assumption is motivated by the fact that the transformer ratio T is not exactly known and, subsequently, the transduced force F_b is proportionally related to the actuator force F_{act} by the lever amplification ratio. The latter relation is summarized in table 6.1 for each actuation direction.

6.2 Frame Suspension Design

The frame suspension is of considerable importance as portable application puts high demands on the the ability to cope with external mechanical disturbances, especially shock disturbances. Shock disturbances are considered more critical than other external disturbances, such as temperature and humidity changes. They come in a wide variety, in magnitude and shape, and specifications are divided into operational and non-operational situations. The criteria for a non-operational specification is that there may be no damage after the shock while the operational specification require a data read out also during shock. For simulation purposes, shocks are formalized as profiles being half-sine pulses, with a duration T and peak value A [14]. Here, only shocks for operational situations will be considered. The selected shock profiles are based on the overview of current specifications, given by different companies, for storage applications [14]. From the overview, all operational shock profiles satisfying the read out criteria are selected. For analyzing joggability the jog shock profile defined in [34] will be used.

The selected profiles are shown graphically in figure 6.3 and are defined by

- Portable drive shock: $T = 3$ ms, $A = 4$ g,
- Compaq removable drive shock: $T = 11$ ms, $A = 6$ g,
- Jog shock: $T = 80$ ms, $A = 4$ g.

The spectra of the disturbance profiles are shown in figure 6.4. From this figure it is seen that the profiles contain mostly low frequency energy.

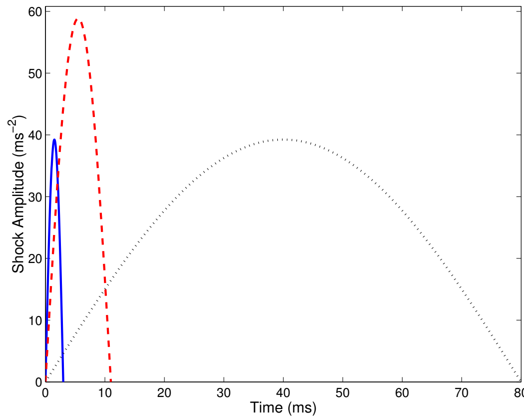

Figure 6.3: Shock profile for a portable drive shock (solid), Compaq removable drive shock (dashed) and jog shock (dotted).

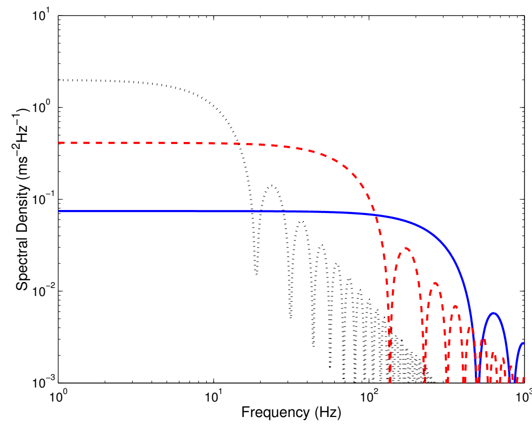

Figure 6.4: Shock profiles spectral density: portable drive shock (solid), Compaq removable drive shock (dashed) and jog shock (dotted).

Among the design parameters affecting the shock sensitivity are the frame suspension undamped natural frequency ω_{n_f} and the damping ratio β_f. Shock simulations affecting position y_1 and y_2 have been carried out for each shock, with a simulation time of 250 ms. For specific combinations of the design parameters the maximum of the response y_1 and y_2 during the simulation run are calculated. A typical simulation result, for the actuation of the system in x direction, is shown in figure 6.5. The simulation shows the system respons y_2 for a Compaq Removable Drive Shock and with ω_{n_f} equals 40 Hz and β_f is 20%. The frame suspension is assumed to be made from a material with a high internal damping, such as rubber. The undamped natural frequency is assumed to lie between 15 and 90 Hz and the damping ratio between 5% and 40%. For all possible combinations of the frame design parameters simulations have been carried out. For the actuation of the system in x direction the results are shown in Appendix G.

The jog shock simulation results show that one should select a high frame suspension damping ($\beta_f > 40\%$) to increase joggability. In addition, for a small maximum position offset it is preferred to have a frame undamped natural frequency of 35 Hz or higher. Further, to satisfy position requirements on position y_1, it results from the portable drive shock and Compaq removable drive shock simulations that ω_{n_f} should be at least 65 Hz. For the actuation of the system in y and z direction only the amplitudes of the simulation results are slightly different. The overall behavior is equal. Therefore, for all three directions, a frame undamped natural frequency of 65 Hz and a damping ratio of 50% is assumed.

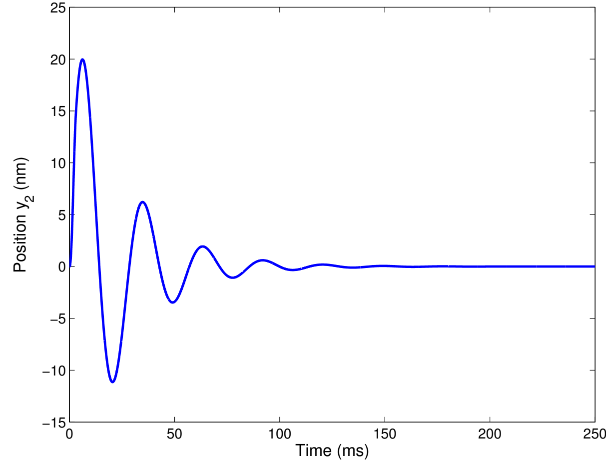

Figure 6.5: The system response y_2 for a Compaq Removable Drive Shock and with ω_{n_f} equals 40 Hz and β_f is 20%.

6.3 System and Disturbance Dynamics

The open loop dynamical properties of the given linear dynamical system can be visualized in both the frequency and time domain. Therefore, the frequency domain behavior is discussed section 6.3.1 and time domain simulations are presented in section 6.3.2.

6.3.1 System Frequency Responses

A frequency response characteristic represents the stationary input-output behavior of sinusoidal signals as function of the frequency by means of an amplitude and phase. For the dynamical model, shown in figure 6.1, the relevant input-output relations are represented in the block diagram shown in figure 6.2. The frequency responses of the system dynamics G_1 and G_2 are shown in figure 6.6. The dynamics in x, y and z direction show slightly different behavior. All three directions have a suspension undamped natural eigenfrequency ω_{n_f} at 65 Hz, as was designed in the previous section. The probe generating element undamped natural eigenfrequency ω_{npg} is respectively 4.0, 5.4 and 3.6 kHz. From the figures it is seen that the actuator force F_{act} hardly affects position y_1, especially in the low frequency region. Notable on the dynamics G_2 is the high undamped natural eigenfrequencies and the large low frequency region with constant gain. Both are a consequence of the large piezoelectric element stiffness and low mass.

The influence of the disturbance accelerations on position y_1 and y_2 is shown by the frequency responses of respectively H_1 and H_2 in figure 6.7. Both the frequency responses H_1 and H_2 show a low pass frequency behavior with the break frequency at the suspension undamped natural eigenfrequency ω_{n_f}. From frequency response H_2 it is expected that the z direction is most sensitive to disturbance accelerations on the casing, followed by the x direction. The y direction is least sensitive to disturbance accelerations. The difference between H_1 and H_2 shows that position y_1 deflects more than position y_2 on a given input.

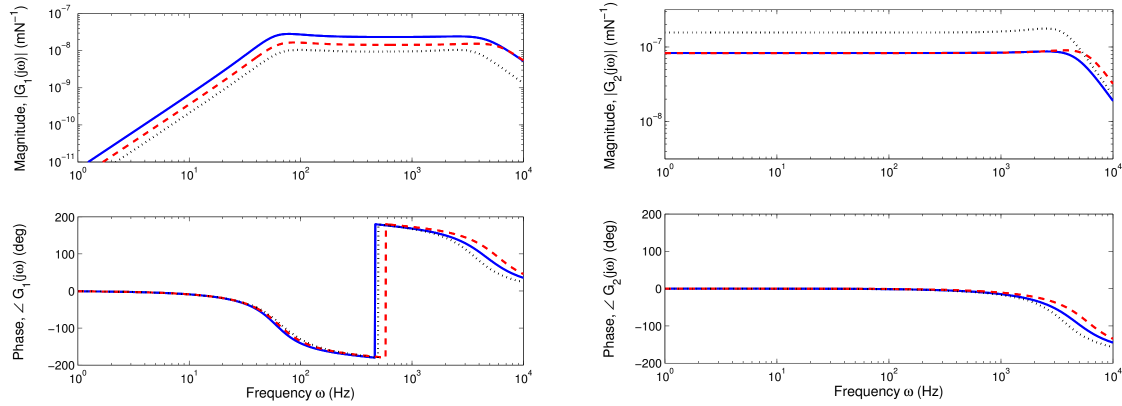

Figure 6.6: Open loop system frequency responses G_1 (left) and G_2 (right) in x direction (solid), y direction (dashed) and z direction (dotted).

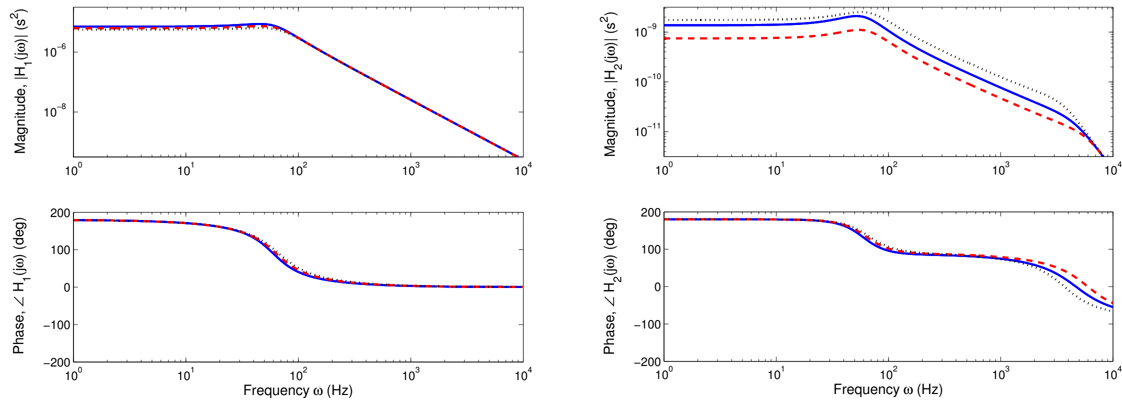

Figure 6.7: Open loop disturbance frequency responses H_1 (left) and H_2 (right) in x direction (solid), y direction (dashed) and z direction (dotted).

6.3.2 Time Domain System Behavior

The open loop disturbance behavior is demonstrated by time domain system simulations. The results are shown in the figures 6.8, 6.9 and 6.10, for respectively the system in x, y and z direction. The simulations show that in the z direction the system is most sensitive to shock disturbances, as it shows the largest amplitudes, followed by the x direction. This was already expected from the frequency responses H_2, as the frequency response in z direction has higher gains over the whole frequency range. Compared to the required accuracy margins for the system in each direction, as defined in table 3.1, only in z direction the system satisfies the requirements. In the x and y direction the responses have too large amplitudes for almost every shock, especially the Compaq removable drive shock results in large response amplitudes on y_2. Because it is discussed before in section 4.1 it is notable that the open loop disturbance response show that the system is not a self braking system. Otherwise, no probe generating element displacement would be obtained by external accelerations.

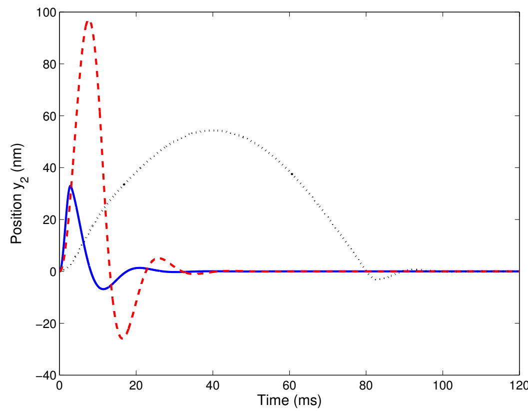

Figure 6.8: Open loop disturbance time response of position y_2 in x direction for a portable drive shock (solid), Compaq removable drive shock (dashed) and jog shock (dotted).

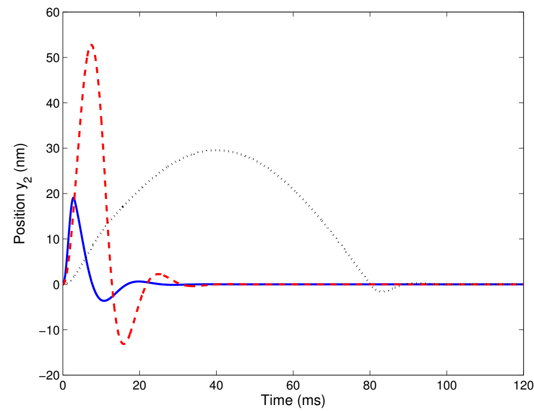

Figure 6.9: Open loop disturbance time response of position y_2 in y direction for a portable drive shock (solid), Compaq removable drive shock (dashed) and jog shock (dotted).

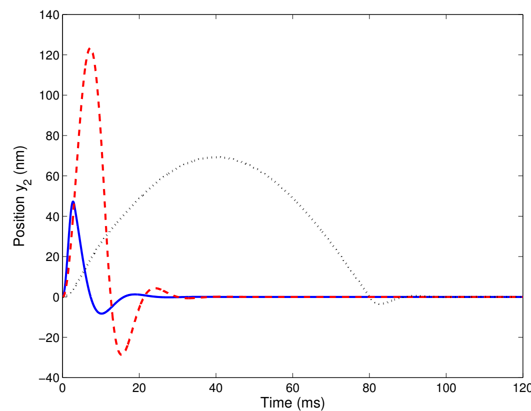

Figure 6.10: Open loop disturbance time response of position y_2 in z direction for a portable drive shock (solid), Compaq removable drive shock (dashed) and jog shock (dotted).

Finally, the open loop time response on a step in the transduced force from electrical side F_b, with an amplitude of 150 N, is shown in figure 6.11 for each direction. The z direction shows the largest amplitude, which is a consequence of the integrated lever. The response times are comparable and in either case less than 1 ms.

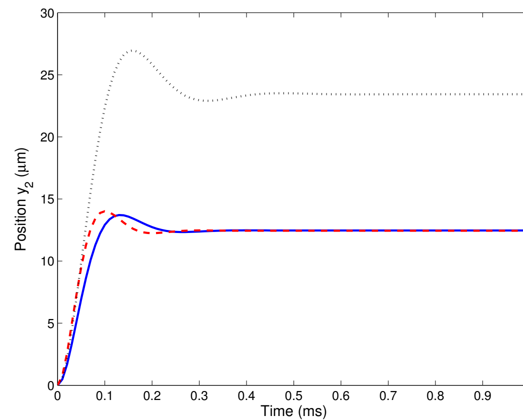

Figure 6.11: Open loop step responses of position y_2 in x (solid), y (dashed) and z (dotted) direction for 150 N step input.

6.4 Discussion

All simulations show that in open loop the system is stable. The y direction is seen to be least sensitive to external disturbances and is therefore found to be most suitable to be chosen to be the tangential direction, as this direction requires the highest accuracy. Consequently, the x direction will be used for selecting the right tracks. Furthermore, amplitude reduction can only be obtained with a higher probe generating element stiffness k_{pg}. A higher damping ratio will only damp the response faster. As the frame suspension was already optimized for the shock disturbance reduction in section 6.2, it can not contribute further to the disturbance reduction. However, a higher value for k_{pg} will limit the stroke y_2.

A solution can be found in a closed loop configuration in which, theoretically, an infinite stiffness can be obtained in a static situation. The closed loop configuration will therefore be discussed in the next Chapter in more detail.

Chapter 7

Controller Design

The T-ROM system requirements include high data rates, short access times, high mechanical shock disturbance rejection and a low bit error rate. The previous chapter showed that an open loop configuration does not satisfy all requirements. A closed loop configuration is also motivated by the fact that the piezoelectric element elongation is hard to predict exactly, due to hysteresis, as was discussed in section 4.2. Moreover, insertion of a new storage medium requires focus adjustment as well as a rotational adjustment. One of the difficulties in controlling the T-ROM system, however, is the low sampling rate of the error signal. This limits the data rate and the access times of the system. Also the suppression of the impact of mechanical shocks is limited to the lower frequency range. Nevertheless, in this chapter the controller design is performed in continuous time.

This chapter is organized as follows. First, in section 7.1, the control architecture is discussed. In section 7.2 bandwidths are estimated in order to obtain the required access times, data rates and disturbance reduction. In order to increase the sampling frequency in section 7.3 the use of a CMOS image sensor is discussed, as was proposed in Chapter 1. To improve further on the access times, in section 7.4 an initial approach to a smoothed reference trajectory is discussed. Subsequently, the controller design is discussed in section 7.5. Finally, simulation results are shown in section 7.6.

7.1 Control Architecture

In section 5.4 it was assumed that the actuator design has three uncoupled directions of motion, each driven by an independent piezoelectric element. For the control architecture this means three Single-Input-Single-Output control loops. In the previous chapter it was concluded that in x direction the system is best used for selecting the right tracks and in y direction the system is best used for scanning along the tracks. The z direction is included for focus purposes. A schematic representation of the control loops is shown in figure 7.1.

The one dimensional block diagram of the closed loop controlled system is shown in figure 7.2. Based on a known (digital) reference signal r, a charge control signal q_{in} is calculated from an error signal ε, amplified by B, and supplied to the digital to analog converter, which assigns a piecewise constant value to the actuator (zero-order-hold). The output signal of interest y_2 is filtered by a filter F, in order to attenuate the effects of high-frequency measurement noise, sampled (analog to digital converter) and fed to the digitally implemented feedback controller, represented by C. Recall that G_1 and G_2

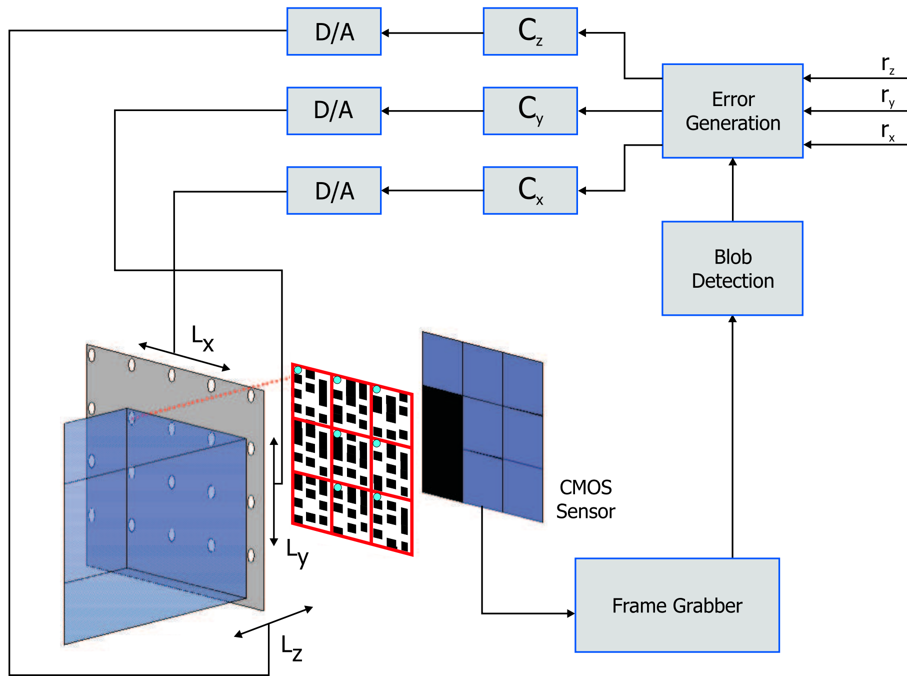

Figure 7.1: Illustration of the three control loops in the T-ROM system.

represent the system transfer functions and H_1 and H_2 describe the influence of external disturbances on the position y_1 and y_2.

The error signals are provided by the blob detection and by the error generation algorithms included in LabVIEW software. The resolution, which can be achieved by the blob detection method in x and y direction, is described in section 2.2. Using the definition given in (2.3) and the parameter values given in table 2.4, gives a resolution of 11.3 nm. This is just enough for accurately positioning in scanning (y) direction, as the accuracy level is ± 7.5 nm. In z direction the error signal generation is still not implemented in the system. The corresponding resolution is expected to be of a lower order, compared to the x and y direction, but still high enough for accurate positioning.

As already mentioned, the controller will be designed in continuous time. This will be discussed in more detail in section 7.5. Further, the gain B will be omitted ($B = 1$) and included in the controller C, as the exact value is unknown. This is motivated by the fact that B, as constant gain, only affects the magnitude and not the phase response. The consequence is that the controller gain will be larger. One should account for this when implementing the controller. Furthermore, to prevent creation of unrealistic controllers, with too high gains that lead to saturation, therefore, limiting the system input is needed. Applying such controllers would otherwise result in performance and stability problems. To take into account piezoelectric element saturation effects the transduced force from electrical side F_b, which is proportionally related to F_{act}, is supposed to be limited to 216 N.

In the remaining of this Chapter only the controller design in x and y will receive attention. The z direction is not considered. Among the reasons is the fact that the system already attenuates the mechanical shocks sufficiently. In the end, in order to read data reliably, also for the z direction a controller will be required. The controller should attain the storage medium at the Talbot distance at all times with the required accuracy. Basically, as the system dynamics in z direction resemble the system dynamics in x and y direction, the controller in z direction will have the same structure as the controller in either the x or y direction.

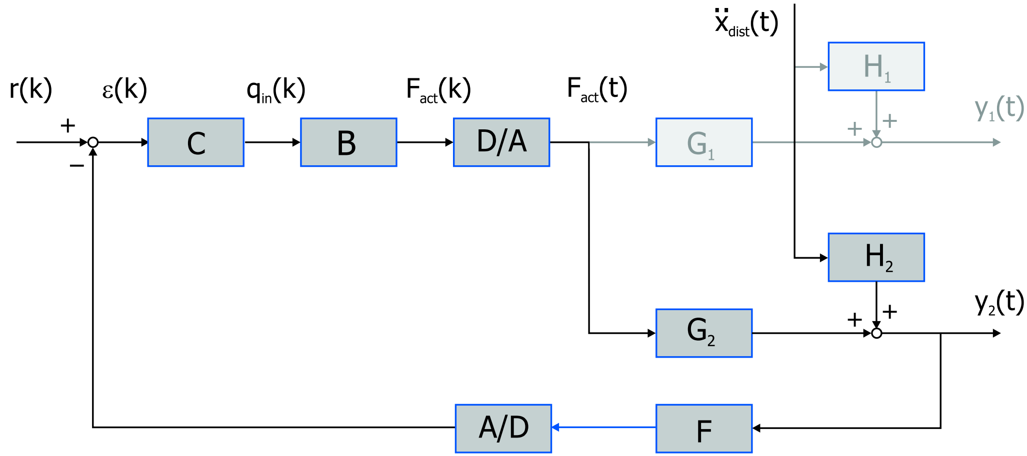

Figure 7.2: Block diagram of the closed loop system.

7.2 Bandwidth Specifications

In this section the required system bandwidth is derived for both the tangential and transversal direction. In section 7.2.1 bandwidths are specified in order to satisfy the access times while in section 7.2.2 bandwidths are estimated in order to obtain the required shock rejection.

7.2.1 Access Time Specifications

During continuous read-out of the storage medium the probe generating element should be controlled so that on average the x stage is positioned around the neutral (middle) position of a track. For reading out all data, different tracks should be selected sequentially. Short access times require the spots to jump quickly to the desired track. The access time should be on the order of 10 ms, with a maximum of 60 ms. This is comparable to conventional CD, DVD and BD players. The y stage is used to move the spots in tangential direction along the tracks on the storage medium. This movement is denoted here as scanning but, in fact, small jumps from bit to bit are considered. The bit access time depends on the number of data bits which has to be read out by one spot in a second. This will be discussed in more detail later in this section.

The corresponding required system bandwidths, in x and y direction, can be estimated from the time response of a unit step reference value. First, closing the control loop by using feedback creates new system dynamics, denoted here as $G_{cl}(j\omega)$. Then, the closed loop system bandwidth is defined to be the maximum frequency at which the output of the system will track an input sinusoid in a satisfactory manner. In terms of frequency response the bandwidth ω_b, in radians per second, can be obtained from

$$|G_{cl}(j\omega_b)| = \frac{1}{\sqrt{2}} |G_{cl}(0)| , \tag{7.1}$$

where the bandwidth is the frequency at which the magnitude of the frequency response is decreased by a factor $\sqrt{2}$ from the value of the horizontal asymptote at low frequency [7]. For a standard sec-

ond order system, with an undamped natural frequency ω_n and a damping ratio β, the bandwidth is formulated by

$$\omega_b = \omega_n \sqrt{(1-2\beta^2) + \sqrt{(1-2\beta^2)^2 + 1}}. \tag{7.2}$$

For other transfer functions, (7.2) can be used as a good approximation if they contain a dominant pair of poles. This pair of poles, which is assumed to be the closest pole pair to the $j\omega$-axis in the s-plane, describes the slowest mode and influences the dynamical behavior of the system very strongly. The bandwidth frequency measures the speed of the response in the frequency domain. For a unit step reference value, the dependency between the speed of the response, ω_n and β is described by

$$\omega_n t_s = \frac{1}{\beta} \ln \left(\frac{1}{\varepsilon\sqrt{1-\beta^2}} \right). \tag{7.3}$$

This relation describes the envelope of the time response shown schematically in figure 7.3 [22]. The settling time t_s corresponds to the time for the controlled variable first to reach and thereafter remain within a specified error band 2ε, after the given reference value has become constant.

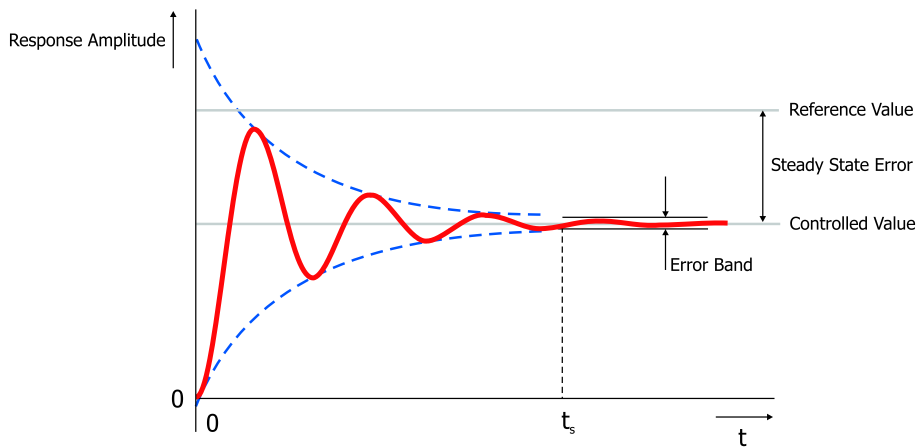

Figure 7.3: Design criteria in a step response.

The system bandwidth follows from a worst case calculation. In x direction a point-to-point move over a distance of 13.0 μm should be considered, which corresponds to the maximum distance between two track centers, as can be obtained from table 2.4. The corresponding accuracy should be 42 nm. Therefore, the error ε, which is defined in terms of percentage of the controlled value, equals 0.3%. Subsequently, for the probe generating element suspension, the access times of 10 and 60 ms corresponds to respectively a bandwidth of 240 and 40 Hz. It should be noted that track identification time is neglected.

Secondly, in y direction, the same approach can be used to determine the required bandwidth. First the bit access time is derived. For N parallel spots and a data throughput rate D, the number of data bits which has to be read out by one spot in a second, denoted by I, is defined by

$$I = \frac{D}{N\eta_{enc}}. \tag{7.4}$$

The parameter η_{enc} represents the encoding efficiency. For the parameters defined in table 2.4, the MPEG-4 and DVD requirements give 6.7 and 67 data bits per spot per second. The corresponding

time interval t_I is defined by

$$t_I = \frac{1}{I}, \tag{7.5}$$

and corresponds to the time available for a spot both accessing and reading out a bit. The bit access time is assumed to be 40% of t_I, as most likely reading out the data bits consumes more time than positioning the spots. This will be discussed in more detail in section 7.3. The MPEG-4 and DVD requirements result in access times of respectively 60 and 6 ms.

As the bits are assumed grouped consecutively, jumps of maximum 75 nm are to be expected. Each bit has to be illuminated with an accuracy of 7.5 nm. Then, the required bandwidths can be estimated with the relations given in (7.2) and (7.3). With $\varepsilon = 10\%$ the corresponding bandwidths are respectively 16.7 and 167 Hz.

7.2.2 Disturbance Reduction Specifications

An important aspect of the T-ROM system is to cope with external shock disturbances. The open loop disturbance behavior was already discussed in section 6.3.2. Only in z direction the system is able to withstand shocks without exceeding the requirements. In the x and y direction an active shock disturbance rejection is required. One justification for feedback is to reduce the effect of disturbances, internal or external, on the performance of a control system. The benefits of the closed loop system response to disturbances, compared to the open loop system response to disturbances, is described by the sensitivity frequency response. For the block diagram shown in figure 7.2 the sensitivity frequency response $S(j\omega)$ is defined by

$$S(j\omega) = \frac{1}{1 + C(j\omega)Z(j\omega)G_2(j\omega)F(j\omega)}. \tag{7.6}$$

The frequency responses C, Z, G_2 and F describe respectively the responses of the controller, the digital to analog conversion by means of a zero-order-hold, the system dynamics and the filter. A typical plot of a sensitivity frequency response is shown in figure 7.4. The response is small at low frequencies, which is desirable for good disturbance rejection. This corresponds to integral action in the controller, and will be discussed in more detail in section 7.5. At the sensitivity 0 dB crossover frequency f_{co},

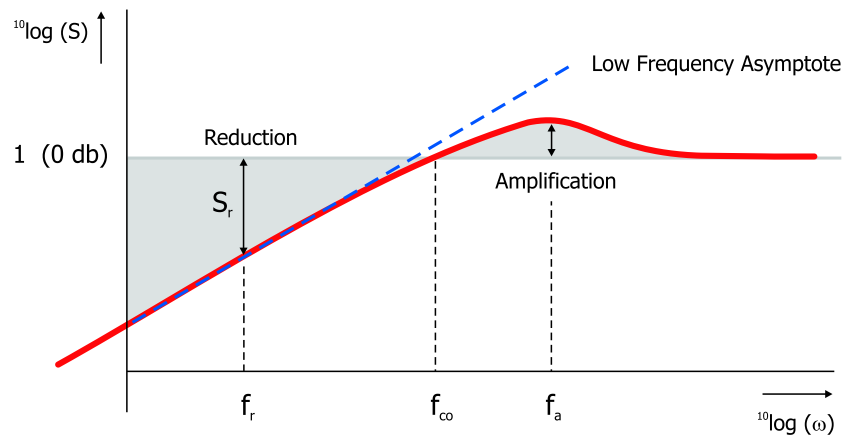

Figure 7.4: Typical plot of the sensitivity frequency response function.

Table 7.1: Disturbance reduction factors.

	Reduction factor (Portable Drive Shock) [−]	Reduction factor (Compaq Removable Drive Shock) [−]	Reduction factor (Jog Shock) [−]
x direction	0.77	2.3	1.3
y direction	2.5	7	4

the sensitivity frequency response approaches unity and crosses it, before approaching unity again for high frequencies. The sensitivity 0 dB crossover frequency, or simply sensitivity crossover frequency, approximately corresponds to the bandwidth definition given in (7.2).

In order to obtain the desired disturbance rejection, the systems open loop disturbance behavior is used to estimate the required bandwidth. In the x and y direction, an accuracy level of respectively 42 nm and 7.5 nm is specified. Compared to the maximum of the responses, shown in the figures 6.8 and 6.9, the required reduction factors can be calculated. The reduction factors are summarized in table 7.1. For example, for the jog shock in x direction, a reduction of 1.3 is required. Approximations of the frequencies at which the disturbance reduction should be obtained are based upon sinusoidal signals with a period of twice a shock duration. For the shock durations of 3, 11 and 80 ms the corresponding frequencies are 167, 45 and 6 Hz. In practice, however, the shock spectra contain more than one single frequency, as is shown in figure 6.4. The given frequencies are the frequencies at which the magnitudes of the spectral contents are decreased by 20% from the value of the low frequency horizontal asymptotes. Therefore, the frequencies 167, 45 and 6 Hz, serve only as indications of the shock frequency contents.

The sensitivity crossover frequency can be approximated by assuming a slope h (on a log-log scale) of the asymptote of the sensitivity frequency response at low frequencies, as is illustrated in figure 7.4. Then, for a disturbance which occurs at a frequency f_r, and needs to be reduced by a factor S_r, the sensitivity crossover frequency f_{co} can be calculated from

$$^{10}\log\left(S_r\right) \;=\; h \cdot \,^{10}\log\left(\frac{f_{co}}{f_r}\right). \tag{7.7}$$

In both the x and y direction the reduction factors, given in table 7.1, will bound the sensitivity frequency responses. By assuming a slope h of $+1$, f_{co} can be calculated such that the bounds are satisfied. As the sensitivity crossover frequency approximates the bandwidth, in x and y direction the bandwidth should approximately be 104 and 418 Hz respectively.

7.2.3 Sampling Frequency Requirements

The bandwidth frequency estimates are summarized in tabel 7.2. The system bandwidth frequency, however, is limited by the fact that the system operates on samples of the sensed output y_2 rather than on a continuous time signal. Using a continuous time controller design method, without accounting for the sampling frequency, will show a degradation of performance due to sampling, as the lagging effect of the zero-order-hold is ignored. Required sampling rates of 20 times the bandwidth frequency are therefore recommended [7]. A better approach is to analyze the entire system using an exact discrete analysis. This allows lower sampling rates, in order of 5 times the bandwidth frequency. Because of simplicity, the controller design method, which will be used in section 7.5, will be performed in continuous time. The lagging effect of the zero-order-hold will be taken into account separately by means of a frequency response function. This will be discussed in more detail in section 7.5.

Table 7.2: Bandwidth requirements.

	Bandwidth ω_b ($t_s = 60$ ms) $[Hz]$	Bandwidth ω_b ($t_s = 10$ ms) $[Hz]$	Bandwidth ω_b (Disturbance Rejection) $[Hz]$
x direction	40	240	104
y direction	16.7	167	418

As will be seen in the next section, a practical sampling frequency is around 1000 Hz. When assuming that the controller design method, which will be used in section 7.5, approximates the discrete controller design method, the bandwidth is expected to be 5 times lower than the sampling frequency. Therefore a maximum bandwidth of around 200 Hz is to be expected. Compared to the bandwidth requirements, as summarized in table 7.2, it is expected that especially the disturbance rejection of the system in y direction will not be reached. Therefore, in the next section, also the feasibility of even higher sampling frequencies than 1000 Hz are investigated.

7.3 Image Sensor Bandwidth Improvements

The bandwidth estimates derived in the previous section require sampling frequencies of 1000 Hz and more. The sampling frequency, however, is limited by the CCD sensor refresh rate. Currently available CCD sensors have full-frame refresh rates of 30 to 40 Hz. An option to increase the sampling rate is to use a CMOS sensor instead of CCD sensor. CMOS sensors offer the possibility to read out small regions-of-interest at a significantly higher rate than the full-frame refresh rate. This is called windowing or region-of-interest read out. By placing a window around the areas on the medium that contain the servo marks, the servo lines, one can detect the servo marks at higher rates. A typical servo mark area, as is depicted in figure 2.4, covers 1% of the total sensor area. In principle, the refresh rate for reading out the servo information, using windowing, can be increased by a factor of 100.

Both a CCD and CMOS sensor converts an image, by means of photons, into a voltage, only the conversion method is different. The voltage level depends linearly on the light intensity and the integration time [2]. The latter is also known as the sensor shutter time and is inversely proportional to the refresh rate. When the light intensity or integration time decreases, the voltage level will reduce, as less photons are captured. For very low voltage levels noise sources will dominate the signal. An overview of noise sources in image sensors is given in [2] but will not be discussed here. In order to accurately determine the position in the T-ROM system at a high rate, the blob quality should be sufficient, i.e. with a sufficiently high signal to noise ratio. However, the spots generated by the aperture array have a very low light intensity. Noise is dominating the signal as soon as the refresh rate is increased. Compensating by increasing the power of the laser is best not to be done as it is at the cost of power consumption. Another option is to use a lens array in stead of an aperture array, as it generates spots with significantly higher intensity [3]. The lens array will be used here without discussing its spot generation in more detail.

To show the feasibility of the blob detection at significantly higher rates, a CMOS sensor was integrated in a tabletop setup of the T-ROM system and was carefully aligned with the other components. The sensor is a 12 bit Silicon Imaging digital camera with a resolution of 1280 x 1024 pixels. The tabletop setup is shown schematically in figure 7.5. In LabVIEW software the camera communication is programmed by means of serial commands. The program allows to adjust the pixel value gain and offset. Also selecting a region of interest and read out at higher rates is possible. In the presented setup a

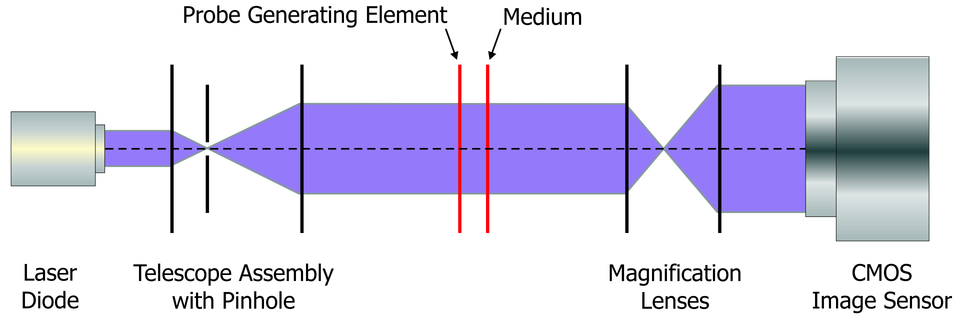

Figure 7.5: Schematic layout of a T-ROM tabletop setup with integrated CMOS image sensor.

window is defined around a servo line, with a width of 1200 pixels and a height of 3 pixels. This corresponds to approximately 0.3% of the total number of pixels. Three different sampling frequencies are selected, namely 15, 1000 and 3700 Hz. After the measurement the 3 rows of pixels are averaged and the results are shown in figure 7.6. The intensity scale has 4095 levels (12 bit). The increase in gain when increasing the sampling rate is notable. From the 15 Hz measurement is also notable that some pixels got saturated.

The measured blobs are quantified by a signal-to-noise ratio SNR, which is defined here according to

$$SNR = \frac{A}{\sigma}, \tag{7.8}$$

with A the amplitude of the blob intensity profile and σ the standard deviation of the noise. The standard deviation is determined by first filtering the signal with a 4th-order low pass Butterworth filter. Afterwards, the standard deviation is calculated from the difference of the original unfiltered signal and the filtered signal. The signal-to-noise ratio for each sampling frequency is summarized in table 7.3. The measurements are done randomly, only the gain and offset are adjusted. The maximum resolution in position which can be determined is not investigated. It is therefore difficult to qualify the blob profiles. In general the signal-to-noise ratio decreases when the frame rate increases. Without studying the results in more depth the measurements show at first sight promising results.

Table 7.3: Signal-to-noise-ratios of the blob measurements.

Sampling frequency	15 Hz	1000 Hz	3700 Hz
	[−]	[−]	[−]
Blob Amplitude A	3500	850	300
Noise Standard Deviation σ	187	61	58
Signal-to-noise ratio	19	14	5

7.4 Reference Trajectory

Using a step reference value, while dealing with a large sample delay, results in a large positioning error during a motion. As a consequence, as in a piezoelectric element the transduced force from

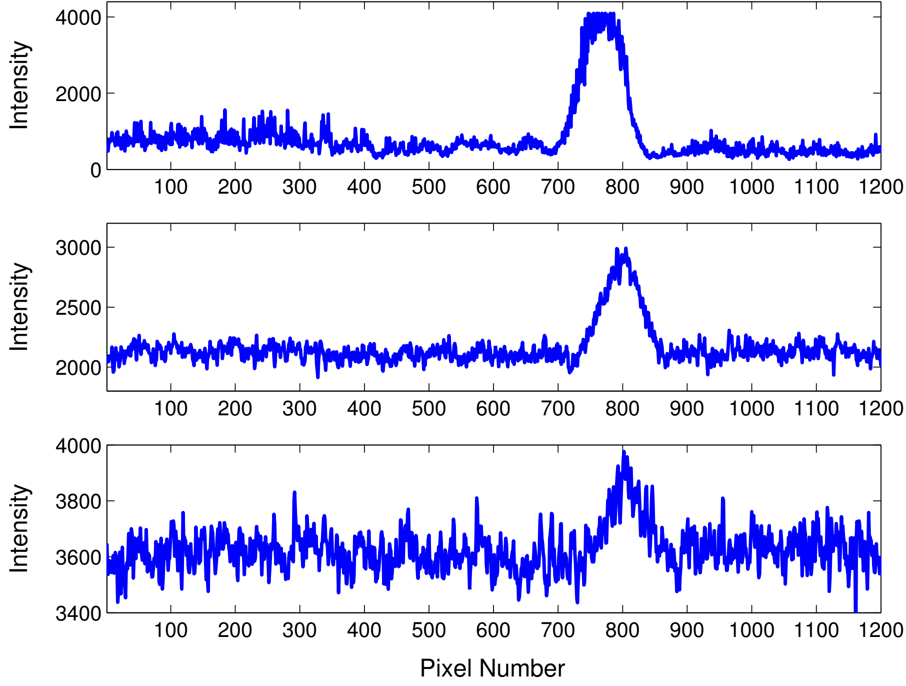

Figure 7.6: Blob measurements at a sample rate of 15 Hz (top), 1000 Hz (middle) and 3700 Hz (bottom).

electrical side is limited, saturation effects may occur, especially in the worst case situation that the spots have to jump over the maximum distance of 13.4 μm. To improve on the positioning error during a motion a smoothed reference trajectory can be used. In case of a second order trajectory, the trajectory should be designed such that acceleration and velocity constraints are not exceeded. For the conceptual actuator design, discussed in Chapter 5, the acceleration constraint is determined by the stage mass and the transduced force available from the piezoelectric element. The bound on the acceleration $\overline{a}$ can be calculated from

$$\overline{a} = \frac{F_{act}}{m_{pg}}. \tag{7.9}$$

For the system in x direction the force F_{act} is maximum 216 N and the stage mass m_{pg} approximates 19.5 gram. Therefore, it follows $\overline{a} = 1.1 \cdot 10^4$ m/s^2. Further, an indication of the bound on the velocity is found in [26] and based on the response time of piezoelectric elements. For the piezoelectric elements used here the velocity constraint $\overline{v}$ equals 0.23 m/s. For a worst case jump in x direction, which is 13 μm and corresponds to the maximum distance between two track centers, the execution time equals 0.07 ms, and is obtained in an unconstraint situation and .

However, when implementing a planned trajectory in the T-ROM system, it is important to consider the effect of discretization. A smooth motion, while dealing with a low sampling frequency, requires lower bounds on the acceleration and velocity. A consequence is the loss of time optimality, and therefore a longer execution time is expected. An approach to synchronize with the sampling frequency is given in [16]. The round-off value for the time range of constant acceleration $t'_{\overline{a}}$ can be calculated by

$$t'_{\overline{a}} = \text{ceil}\left(\frac{t_{\overline{a}}}{T_s}\right) \times T_s, \tag{7.10}$$

with ceil($\cdot$) denoting the rounding off toward the next higher integer and T_s represents the sample interval. The time range $t_{\overline{a}}$ gives the time range of the constant acceleration in an unconstrained

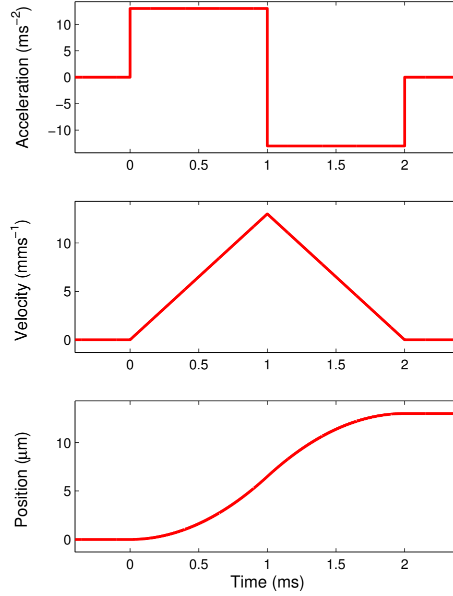

Figure 7.7: Second order trajectory profile with $T_s = 1000$ Hz.

situation. The new value for the bound on the acceleration can then be calculated from

$$\overline{a}' = \frac{\overline{x}}{t'^2_{\overline{a}}}. \tag{7.11}$$

It is noted that $\overline{a}' \leq \overline{a}$ as $t'_{\overline{a}} \geq t_{\overline{a}}$. A same approach is valid for the recalculation of the range of constant velocity t_v. In figure 7.7 the calculated second order trajectory profile, for a worst case jump over 13 μm, is given for a sampling frequency of 1000 Hz. The bound on the acceleration is 13 ms^{-2} and t_a equals 1 ms, while the velocity constraint is not reached, and therefore t_v equals zero. A similar second order trajectory profile can be calculated for accessing the bits.

In order to obtain the trajectory, an input signal for the piezoelectric element may be calculated by a feedforward controller. The feedforward control problem is then to generate the force required the elongate the piezoelectric element, by overcoming the element stiffness. Mass feedforward is not in order as inertia starts playing a role at frequencies much higher than the sampling frequency ($>$ 3 kHz). However, feedforward control based upon inverse system dynamics require accurate system models. In the case of a piezoelectric element an accurate stiffness value is required. But, as stated before in section 4.3.2, the stiffness is in fact rather undefinable as one should distinguish different operating situations. The hysteresis effect makes the elongation even harder to predict. In order to deal with unmodelled system behavior feedforward control always needs feedback control. Furthermore, as tracking a reference trajectory is not an aim in itself, the focus is on feedback control.

7.5 Feedback Controller Design

The importance of a feedback controller in the T-ROM system was already discussed before. Summarized, the control design problem can be stated as finding a controller which achieves short access times and obtains shock disturbance rejection. The controller will be designed such that the loop gain frequency response function has a suitable shape. First, for the closed loop system given in figure 7.2,

Table 7.4: Controller parameters.

	T_s [ms]	K [Nm^{-1}]	τ_i [ms]	τ_f [ms]	GM [dB]	PM [deg]
x direction	1	$9 \cdot 10^9$	0.64	0.53	16.8	88
y direction	0.77	$16 \cdot 10^9$	0.5	0.4	8.1	48

the loop gain frequency response $G_{ol}(j\omega)$ is defined by

$$G_{ol}(j\omega) = C(j\omega)Z(j\omega)G_2(j\omega)F(j\omega). \tag{7.12}$$

The zero-order-hold frequency response $Z(j\omega)$ describes the sequence of step functions at the digital to analog conversion output and can be characterized by

$$Z(j\omega) = \frac{1 - e^{-j\omega T_s}}{j\omega}, \tag{7.13}$$

where T_s represents the sample period of the signals. The filter operation is by means of a first order low-pass filter. The frequency response $F(j\omega)$ is therefore described by

$$F(j\omega) = \frac{1}{j\omega\tau_f + 1}, \tag{7.14}$$

with τ_f the time constant of the filter.

In order to achieve disturbance attenuation, at low frequencies the sensitivity frequency response needs to be small. This can be achieved by making the loop gain large, i.e. $|G_{ol}(j\omega)| \gg 1$, in the low frequency region. This can be obtained by including an integral action in the controller transfer function C. Integral control is moreover required for eliminating the steady state error, between reference and controlled value. In the region where $|G_{ol}(j\omega)|$ approximates 1, it is not sufficient to consider the magnitude of the loop gain alone as instability may occur. To guarantee a stable and robust system the stability and robustness margins, i.e. gain margin, phase margin and modulus margin [7], are selected to be respectively 2, 45 degrees and 0.5. Finally, to adjust the bandwidth frequency, a proportional gain is added to the controller transfer. The controller frequency response $C(j\omega)$, with proportional and integral action, has the form

$$C(j\omega) = K\left(1 + \frac{1}{j\omega\tau_i}\right), \tag{7.15}$$

where K represents the proportional gain and τ_i represents the integration time constant. In the frequency domain the corresponding break frequency f_i can be obtained from

$$\tau_i = \frac{1}{2\pi f_i}. \tag{7.16}$$

To ensure that the closed loop response is fast enough the proportional gain should be large. However, to prevent saturation effects and instability, the proportional gain must not be increased too much. Regarding the integrating action one should pay attention to a proper time constant τ_i, as for a too large value a too slow system may be obtained, or for a too small value instability may occur.

For a satisfactory fast closed loop response and disturbance rejection in x direction, the proportional gain K is chosen to be $9 \cdot 10^9$ and the corresponding integration time constant τ_i is 0.64 ms. This integration time constant corresponds to a break frequency $f_i = 250$ Hz. The controller frequency response is shown in figure 7.8. The filter time constant τ_f is 0.53 ms and as proposed the sampling frequency is selected to be 1000 Hz. The sensitivity frequency response is shown in figure 7.9, and shows a reduction in the frequency region below 234 Hz. The controller parameters are summarized in table 7.4. The results will be discussed in section 7.6.

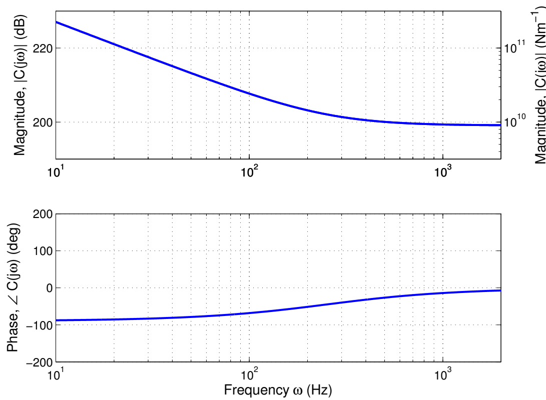

Figure 7.8: Controller frequency response.

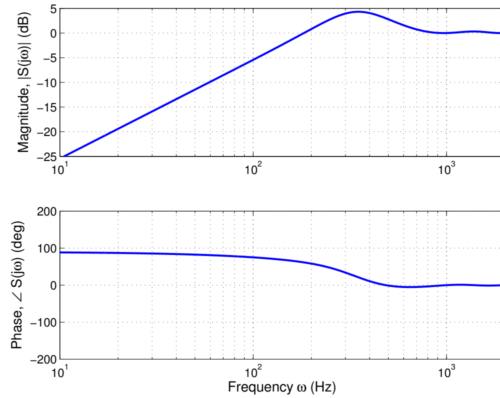

Figure 7.9: Sensitivity frequency response.

7.5.1 Stability Analysis

The controller design ensures the closed loop system remains stable. From the loop gain frequency response, shown in figure 7.10, the gain and phase margin is respectively 16.8 dB, which corresponds to a factor 6.9, and 88 degrees. The resulting bandwidth frequency equals 234 Hz. The gain and phase margin and the modulus margin, can also be analyzed in a Nyquist diagram. These margins determine how closely the loop gain approaches the point $(-1, 0)$. In figure 7.11, a modulus margin of 0.5 is marked, which corresponds to the radius of the given circle with the center at the point $(-1, 0)$. Without calculating the exact modulus margin it is seen that the stability and robustness margins are fulfilled. It is noted that the resulting stability and robustness margins are larger than the requirements. The reason is, smaller margins would substantially degrade the damping, resulting in much larger access times.

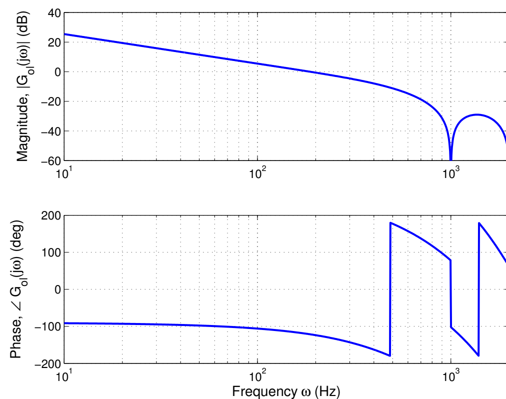

Figure 7.10: Loop gain frequency response.

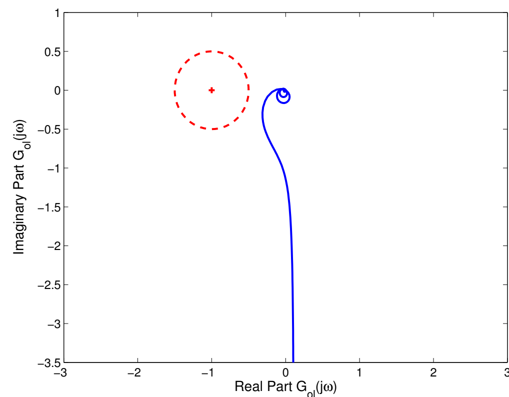

Figure 7.11: Nyquist diagram of the loop gain (solid) and a modulus margin of 0.5 (dashed).

7.6 Simulation Results

The results of the controller design for the closed loop performance are also evaluated by using MatLab/Simulink. The closed loop response to a reference value is shown in figure 7.12. The settling time is 6 ms, and therefore satisfies the requirement of accessing a new track within 10 ms. In figure 7.13, the closed loop shock disturbance response indeed does not exceed the required accuracy level of ± 42 nm.

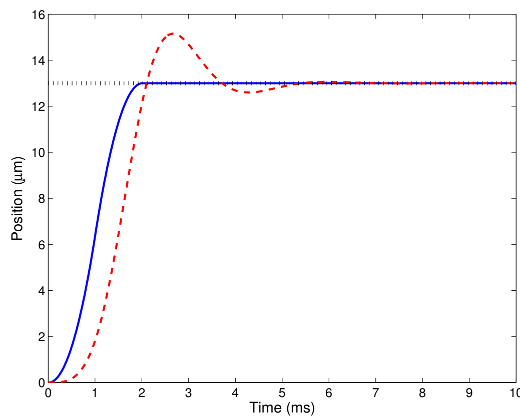

Figure 7.12: Time response in x direction for T_s = 1000 Hz: input (solid), output (dashed) and accuracy margin (dotted).

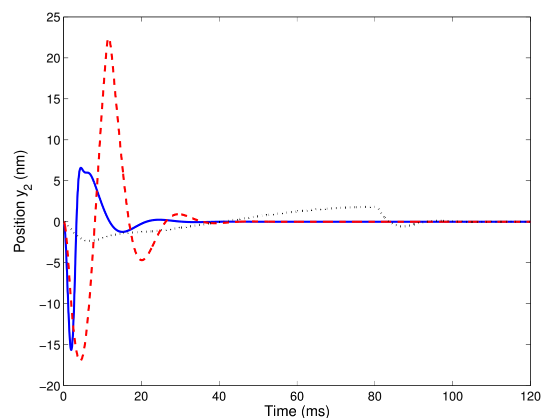

Figure 7.13: Shock response in x direction with T_s = 1000 Hz and for a portable drive shock (solid), Compaq removable drive shock (dashed) and jog shock (dotted).

Also for the y direction a proportional and integral controller is designed. However, in order to satisfy the shock requirements, a sampling frequency of 1300 Hz is required. The controller and filter param-

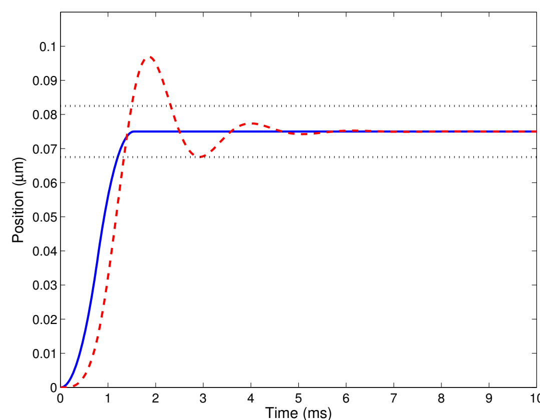

Figure 7.14: Time response in y direction for T_s = 1300 Hz: input (solid), output (dashed) and accuracy margin (dotted).

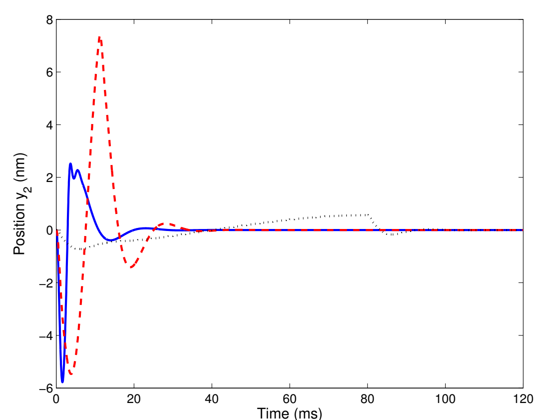

Figure 7.15: Shock response in y direction with T_s = 1300 Hz and for a portable drive shock (solid), Compaq removable drive shock (dashed) and jog shock (dotted).

eters are given in table 7.4. In the table also the stability margins are given. The bandwidth obtained from the loop gain frequency response equals 326 Hz. The closed loop results in y direction are shown in the figures 7.14 and 7.15. The settling time is approximately 2.5 ms, which is in the requirement (6 ms), and all shock responses satisfy the requirement of ± 7.5 nm.

7.7 Discussion

In order to achieve satisfactory system behavior sampling frequencies up to 1300 Hz were required. The limiting factor was the mechanical shock disturbance rejection in the tangential (y) direction, as this direction requires the highest accuracy. In general, mechanical shock disturbance rejection required higher sampling frequencies than satisfactory access times require. Originally, the bandwidth was limited by the CCD image sensor refresh rate. Experimental results had shown that using a CMOS image sensor would allow to increase the bandwidth significantly. Rates of more than 1000 Hz gave, at first sight, good results. The remaining question will be at what level of accuracy the position really can be detected.

It was noted that the resolution in the newly to be developed demonstrator is just high enough for accurately positioning the probe generating element in tangential direction. For the final aim of the T-ROM system, a storage medium size of 18 x 18 mm^2 is suggested. By using the definition for the resolution, given in (2.3), this leads to an improvement of a factor 2.5 compared to the system configuration discussed in section 2.4. Then, for the final aim, the resolution will be 4.5 nm.

Chapter 8

Conclusions and Recommendations

For the T-ROM optical storage system, a 3 degree of freedom (DOF) actuator was motivated on the basis of positioning and alignment requirements of the system. Afterwards, an in-plane piezoelectric actuator was designed at Philips Research.

Piezoelectric actuation was found to be the best option to actuate the DOFs. Monolithic piezoelectric stack elements, which operate in the longitudinal mode, are the best to use due to their high performance. Moreover, they allow a compact actuator design. In order to predict and get insight in the piezoelectric element behavior an electromechanical model was derived. A difference between voltage and charge steering was established, as piezoelectric elements suffer from hysteresis in a voltage configuration and behave linearly in a charge configuration.

The challenge of the actuator design was the integration of a focus and scanning actuation in a compact construction with a height of maximum 3 mm. Simple calculations, as well as a finite element analysis, showed that in-plane movements satisfy the requirements. In the out-of-plane direction, the motion errors exceeded the requirements. Therefore, a recommendation for an alternate design was given. The construction height constraint also limited the dynamic behavior of the actuator. The first vibration mode was in an uncontrolled direction, and was excited by the expected external mechanical shock disturbances. Significantly increasing the resonance frequency could only be obtained by increasing the construction height.

In order to analyze the T-ROM system performance, the 3 DOF actuator was assumed to be integrated in a casing, for example, a mobile phone casing. Only the controlled directions were observed. A simple one-dimensional model showed that in in-plane directions the actuator capabilities to cope with external mechanical shock disturbances are not satisfactory. The system was found to be most sensitive to low frequency disturbances. In order to increase joggability, a high suspension damping was suggested.

In order to have satisfactory access times and improve the disturbance rejection, control objectives were specified. Because of linearity, charge control was considered to demonstrate the system behavior. Subsequently, for the in-plane directions straightforward proportional and integral feedback controllers were designed. The controller design for the out-of-plane direction was omitted, but would have the same structure as the controllers in the in-plane directions. After control, satisfying disturbance rejection was obtained. The system also gave satisfactory access times for playing DVD quality videos.

A condition to the proposed feedback controllers was a sufficiently high sampling rate of the error signal. As the image sensor was used to generate the error signal, this put severe demands on the image sensors' refresh rate. In the present setup a CCD image sensor was used, which has a typical refresh rate of 30 Hz. Theoretically, CMOS image sensor windowing would allow to increase the refresh rate significantly. Experimental measurement results had shown that CMOS image sensor windowing gave at first sight promising results for refresh rates up to more than 1000 Hz.

8.1 Recommendations

In order to meet the requirements, it was concluded that the actuator design requires modifications for the out-of-plane actuation. Increasing the construction height is not an option as this was the challenge of the design. Therefore, in order to satisfy the kinematic and static behavior of the stage used for the out-of-plane motion, the point of application of the applied force should be central to the stage thickness direction. The stage should simultaneously be dimensioned such that the hinge thicknesses (parameter h) are 0.2 mm. In order to also satisfy the dynamical behavior, the first vibration mode must have a higher frequency. Besides the option to increase the construction height no other options are given.

The T-ROM system performance was analyzed by considering a charge steering configuration. However, a voltage control configuration is more realistic to use in practice, in spite of the hysteresis effect. Using the approach of describing hysteresis as given in this report, one should focus on an appropriate measurement setup.

Finally, in order to achieve the required disturbance rejection, the sampling frequency needs to be increased. CMOS image sensor windowing had shown that servo mark measurements at higher rates only show promising results. The maximum achievable resolution should be investigated in order to decisively determine whether the servo mark quality is sufficient. One should check for a resolution of at least 15 nm. If not, then the resolution detection of the present moiré magnification technique should be improved.

Bibliography

[1] H.J.M.T.A. Adriaens, W.L. de Koning and R. Banning, "*Modeling piezoelectric actuators*," IEEE/ASME Transactions on Mechatronics, Volume 5, Issue 4, pp. $331-341$, December 2000.

[2] M. Balistreri, H. Goossens, C. Liedenbaum, S, Stallinga, R. Wegh, H. Wilderbeek, "*Holographic Data Storage, A technology assensment*," Philips Nat.Lab. Report TN2002/191, Eindhoven, 2002.

[3] M. Béguin and L.P. Bakker, "*Optical probe array generation, Application in the T-ROM system*," Philips Nat.Lab. Report TN2005/00266, Eindhoven, 2005.

[4] J.M. Cruz-Hernández and V. Hayward, "*On the Linear Compensation of Hysteresis*," Proceeding of the 36th IEEE Conference on Decision and Control, pp. $1956-1957$, San Diego, December 1997.

[5] J.P. Feenstra, P.C. Breedveld and J. van Amerongen, "*Actuation methods for a Surface AcousticWave Motor*," 2nd International Workshop on Piezoelectric Materials and Applications in Actuators, Heinz Nixdorf Institute, University of Paderborn, Parderborn, Germany, May 2005.

[6] R.T. Fenner, "*Mechanics of Solids*," CRC Press LLC, 1999, ISBN $0-632-02018-0$.

[7] G.F. Franklin, J.D. Powell and A. Emami-Naeini *Feedback Control of Dynamic Systems*, Third Edition, Addison-Wesley Publishing Company, 1994. ISBN 0-201-53487-8.

[8] P. Ge and M. Jouaneh, "*Tracking Control of a Piezoceramic Actuator*," IEEE Transactions on Control Systems Technology, Volume 4, No. 3, May 1996.

[9] M. Goldfarb and N. Celanovic, "*Modeling Piezoelectric Stack Actuators for Control of Micromanipulation*," IEEE Control Systems Magazine, Volume 17, No. 3, pp. $69-79$, 1997.

[10] B.J. Hamrock, B.O. Jacobson and S.R. Schmid, "*Fundamentals of Machine Elements*,", McGraw-Hill, Boston, 1999, Paperback Edition, ISBN $0-256-19069-0$.

[11] A.E. Holman, P.M. Scholte, W.Chr. Heerens and F. Tuinstra, "*Analysis of Piezo Actuators in Translation Constructions*," Review of Scientific Instruments, Volume 66, Issue 5, pp. $3208-3215$, May 1995.

[12] T.J. de Hoog, A.A.A. Kastelijn and H.R.M. Verberne, "*Position control in the T-ROM optical card system*," Proceedings of the 8th Philips Conference on Applications of Control Technology, Hilvarenbeek, The Netherlands, $15-16$ February, 2005.

[13] J.W. Judy, D.L. Polla and W.P. Robbins, "*A linear piezoelectric stepper motor with submicrometer step size and centimeter travel range*," Ultrasonics, Ferroelectrics and Frequency Control, IEEE Transactions on Volume 37, Issue 5, p.p. $428-437$, September 1990.

[14] A.A.A. Kastelijn and M.A.H. van der Aa, "*Shock Considerations for a Small Form Factor Optical Drive,*" Philips Nat.Lab. Report TN2002/307, Eindhoven, 2002.

[15] M.P. Koster, "*Constructieprincipes voor het nauwkeurig bewegen en positioneren,*" Uitgeverij Universiteit Twente, The Netherlands, 1996, ISBN. $90-365-0832-0$.

[16] P. Lambrechts, M. Boerlage and M. Steinbuch, "*Trajectory planning and feedforward design for electromechanical motion systems,*" Elsevier Control Engineering Practice 13, pp. $145-157$, 2005.

[17] A. van der Lee, D. Brulls, C. Busch, A. Immink, W. Coene and A. Hekstra, "*Two-Dimensional Optical Storage,*" Japanese Journal of Applied Physics, Volume 43, No. 7B, pp. $4912-4914$, 2004.

[18] H. Liess, T. Hegewald, J.Heinzl, R. Lerch, A. Kappel, T. Schwebel, B. Gottlieb and R. Kraul, "*Piezo Inchworm Actuator for heavy loads,*" Proceeding of the 9th International Conference on New Actuators, pp. $144-147$, Bremen, Germany, 2004.

[19] C.K. Lim, S. He, I. Chen and S.H. Yeo, "*A Piezo-on-Slider Type Linear Ultrasonic Motor for the Application of Positioning Stages,*" Proceedings of the 1999 IEEE/ASME International Conference on Advanced Intelligent Mechatmnics, Attanta, USA, September 1999.

[20] Henkel Loctite Corporation, $http://www.loctite.com$.

[21] B.J. MacLachlan, N. Elvin, C. Blaurock and N.J. Keegan, "*Piezoelectric valve actuator for flexible diesel operation*", Proceedings of SPIE Smart Structures and Materials 2004, Industrial and Commercial Applications of Smart Structures Technologies, pp. 167-178, August 2004.

[22] J.L. Min and J.J. Scharge, "*Ontwerpen van analoge en digitale regelsystemen,*" Uitgeverij Nijgh & Van Ditmar, The Hague, The Netherlands, 1982, ISBN $90-236-0372-9$.

[23] S. Mittal and C.H. Menq, "*Hysteresis Compensation in Electromagnetic Actuators Through Preisach Model Inversion,*" IEEE/ASME Transactions on Mechatronics, Volume 5, No. 4, pp. $394-409$, December 2000.

[24] R. Perez, A. Lal, Y. Miyahara, J. Breguet and H. Bleuler, "*Modeling, Characterisation and Implementation of a Monolithic Piezo-Actuator of* 2 *and* 3 *Degrees of Freedom,*" Proceeding of the 9th International Conference on New Actuators, pp. $41-44$, Bremen, Germany, 2002.

[25] P. Pertsch, D. Rößger, E. Henning, W. Plötner and A. Bauer, "*The Shear Effect in Piezoferroelectric Ceramics and it's Application to Actuator Devices,*" Proceeding of the 9th International Conference on New Actuators, pp. $41-44$, Bremen, Germany, 2002.

[26] Physik Instrumente, PI Ceramics, "*Piezo Ceramics Actuators & Custom Subassemblies,*" Product Catalog 2005.

[27] Piezo Systems, Inc, $http://www.piezo.com$.

[28] J. van Randeraat and R.E. Setterington, "*Piezoelectric Ceramics,*" Philips Application book, Second Edition, 1974.

[29] H. Richter, E.A. Misawas, D.A. Lucca and H. Lu, "*Modeling nonlinear behavior in a piezoelectric actuator,*" Journal of the International Societies for Precision Engineering and Nanotechnology, volume 25, pp. $128-137$, 2001.

[30] W.J.M. Schlösser, W. Post, "*Een samenvattende beschouwing van de overbrengingen in werktuigen,*" Lecture notes course $4B630$ and $4B600$, Eindhoven University of Technolgy, Eindhoven, January 2000.

[31] G. van Schothorst, "*A dynamic test set-up for active vibration control using piezoelectric devices (Smart Discs)*," Philips Nat.Lab. Report TN091/98, Eindhoven, 1998.

[32] T. Shigematsu and M.K. Kurosawa, "*Nanometer Resolution 2-D In-Plane SAW Motor*," Proceeding of the 9th International Conference on New Actuators, pp. 140 − 143, Bremen, Germany, 2004.

[33] Standards Committee of the IEEE Ultrasonics, Ferroelectrics, and Frequency Control Society, "*An American National Standard: IEEE Standard on Piezoelectricity*," The Institute of Electrical and Electronics Engineers, ANSI/IEEE Std 176 − 1987, New York, 1987.

[34] M. Steinbuch and H. Heijboer, "*Design of Suspension and Servo-systems for Compact Disc Mechanisms under Shock Disturbances*," Philips Nat.Lab. Report TN176/91, Eindhoven, 1991.

[35] N. Tamer and M. Dahleh, "*Feedback Control of Piezoelectric Tube Scanners*," Proceedings of the 33rd Conference on Decision and Control, pp. 1826 − 1831, 1994.

[36] K. Uchino, "*Piezoelectric Actuators 2004: Materials, Design, Drive/Control, Modeling and Applications*," Proceeding of the 9th International Conference on New Actuators, pp. 38 − 47, Bremen, Germany, 2004.

[37] N.K. Vestmoen Nilsen and R.A. de Callafon, "*Control Design for a Piezo-Electric Dual-Stage Instrumented Suspension*", Proceedings of the IASTED International Conference on Control and Applications, Marina del Rey, USA, March 2004.

[38] W. Wischnewskiy, S. Kovalev, J. Rapp and O. Vyshnevskyy, "*Simple New Ultrasonic Piezoelectric Actuators for Precision Linear Drives*," Proceeding of the 9th International Conference on New Actuators, pp. 778 − 779, Bremen, Germany, 2004.

[39] W. R. Wehl, "*Ink-Jet Printing: The Current State of the Art*," Microelectronic Applications in Intelligent Peripherals and their Interconnection Networks, Proceedings, p.p 46 − 52, May 1989.

[40] H. van der Wulp, "*Piezo driven stages for nanopositioning with extreme stability, theoretical aspects and practical design considerations*," Thesis, Delft University Press, 1997, ISBN 90 − 407 − 1491 − 6.

[41] A.C. Zaanen and J.P. Baartman, "*The accuracy of the Philips platform a micro Stewart platform, developed by CFT*," Philips Nat.Lab. Report TN150/98, Eindhoven, 1998.

List of Symbols

All symbols used in this report are summarized below. It should be noted that sub- and superscripts, which refer to either a direction, stage or a component, are omitted.

α	Local φ coordinate
β	Local ψ coordinate, Damping ratio [-]
γ	Local θ coordinate
δ	Spot pitch offset [m], Parasitic stage motion as defined in figure 5.5 [m]
$\Delta\alpha$	Rotational angle in α direction [rad]
$\Delta\beta$	Rotational angle in β direction [rad]
$\Delta\theta$	Rotational angle in θ direction [rad]
$\Delta\Theta$	Magnified rotational angle of rotational angle $\Delta\theta$ [rad]
Δu	Displacement in w direction [m]
Δw	Displacement in w direction [m]
ε	Error signal [m], Electrical permittivity [C/Vm]
η_{enc}	Encoding efficiency [-]
λ	Light beam wavelength [m]
ξ	Accuracy margin [m]
ρ	Material density [m^3/kg], Relative storage density [-]
σ	Noise standard deviation [-]
$\Delta\sigma$	Displacement [m]
$\Delta\Sigma$	Magnified displacement of displacement $\Delta\sigma$ [m]
τ	Time constant [s]
υ	Angle between current and magnetic field [degrees]
φ	Global φ coordinate
ψ	Global ψ coordinate
θ	Global θ coordinate
ω	Frequency [rad/s]
ω_n	Undamped natural frequency [rad/s]
ω_b	Bandwidth [rad/s]
a	Spot diameter (Full Width at Half Maximum) [m], Distance as defined in figure 5.5 [m]
$\overline{a}$	Acceleration bound [m/s^2]
A	Shock amplitude [g], Blob Amplitude [-], Piezoelectric element surface area [m^2]
$\mathbf{A}$	nxn upper triangular matrix of ones
A/D	Analog to digital conversion

Symbol	Description
b	Channel bit length [m], Distance as defined in figure 5.5 [m], Damping [Ns/m]
B	Gain
c	Sensor pixel size [m], Distance as defined in figure 5.5 [m], Elastic stiffness [N/m]
C	Spring index [-], Linear piezoelectric element capacitance [F], Controller
C_m	Linearized Maxwell capacitor [F]
D	Size as defined in figure 5.5 [m]
D/A	Digital to analog conversion
d	Data area dimension [m], Spring wire diameter [m], Piezoelectric strain constant [-]
D	Bit rate [bits/s], Dielectric Displacement [C/m^2]
e	Medium holder thickness [m], Piezoelectric stress constant [N/Vm]
E	Electric Field [V/m]
E_y	Modulus of elasticity [N/m^2]
f	Medium dimension [m], Break away force [N], Frequency [Hz]
$\underline{f}$	nx1 vector of breakaway forces
F	Force [N], Filter
F_b	Piezoelectric element blocking force [N]
F_D	Spot depth of focus [m]
F_p	Transduced force from electrical side [N]
F_p^{eff}	Effective transduced force from electrical side [N]
g	Medium holder length [m], Size as defined in figure 5.5 [m], Piezoelectric strain constant [Vm/N]
G	Shear modulus [Gpa], Open loop system dynamics
G_{cl}	Closed loop system
G_{ol}	Open loop system
h	Flexure thickness as defined in figure 5.5 [m], Slope [dB/dec], Data carrier dimension [m], Piezoelectric stress constant [V/m]
H	Operator representing the hysteresis of piezoelectric element, Open loop disturbance dynamics
i	Bit number ($1 \leq i \leq n$) [-], Lever amplification ratio [-], Current [A]
I	Number of bits read out by one spot per second [-], Current [A]
j	Bit number ($1 \leq j \leq n$) [-]
k	Stiffness [N/m], Probe generating element width [m]
$\underline{k}$	nx1 vector of Maxwell model spring stiffness
k_p^o	Open electrode piezoelectric element stiffness [N/m]
k_p^s	Closed electrode piezoelectric element stiffness [N/m]
K	Number of Pixels [-], Force [N], Proportional action
$\mathbf{K}$	nxn diagonal matrix of spring stiffness
l	Flexure length as defined in figure 5.5 [m], Lever length [m]
l_h	Lever height [m]
l_w	Lever width [m]
L	piezoelectric element length [m], Translation
m	Mass [kg], Probe generating element thickness [m]
M	Moment [Nm]
M_m	Number of bits per Macrocell [-]
M_t	Number of bits per Macrocell [-]

n	Probe generating element length [m], Number of bits over the length of a macrocell [-], Number of Maxwell slip elements [-]
N	Number of spots [-], Normal force [N]
N_a	Number of spring active coils [-]
NA	Numerical aperture [-]
p	Spot pitch / Macrocell dimension [m], Size as defined in figure 5.5 [m]
P	Polarization direction
q	Charge [C]
Q	Magnification ratio[-]
r	Reference value [m]
R	Oversampling rate [-], Rotation
s	Elastic compliance [m^2/N]
$\underline{s}$	nx1 vector of slopes
S	Strain [-], Sensitivity
S_r	Reduction factor [-]
SNR	Signal-to-noise ratio [-]
t	Stage thickness as defined in figure 5.5 [m], Track Pitch [m]
$t_{\overline{a}}$	Acceleration time range [s]
t_I	Time to read out one bit by one spot [s]
t_s	Settling time [s]
T	Stress [N/m^2], Transformer ratio [C/m], Shock duration [s], Number of tracks per Macrocell [-]
T_s	Sample interval [s]
u	Local x coordinate, Sensor surface dimension [m], Voltage [V]
u_H	Voltage across hysteresis operator H
u_m	Saturation Voltage [V]
v	Local y coordinate
$\overline{v}$	Velocity bound [m/s]
V	User storage capacity [Mb]
w	Local z coordinate, Sensor surface thickness [m]
x	Global x coordinate, Elongation [m], Spring endpoint position in Maxwell slip model [m]
$\underline{x}$	nx1 vector of spring endpoints in Maxwell slip model
x_b	Position of element in Maxwell slip model [m]
$\ddot{x}_{dist}$	Disturbance acceleration [m/s^2]
x_{max}	Free piezoelectric element elongation [m]
$\overline{x}$	Position bound [m]
y	Global y coordinate, Relative position [m]
z	Global z coordinate
z_S	Relative distance between storage medium and sensor [m]
z_T	Talbot distance [m]
Z	Zero-order-hold

BD	Blu-ray Disc
CCD	Charge Coupled Device
CD	Compact Disc
CMOS	Complementary Metal Oxide Semiconductor
DOF	Degree(s) Of Freedom
DVD	Digital Versatile Disc
GM	Gain Margin
PI	Proportional-Integral
PM	Phase Margin
T-ROM	Talbot Read Only Memory
TwoDOS	Two-Dimensional Optical Storage

Appendix A

System Components

The T-ROM system consists of four basic components. The dimensions and typical features of each individual component are related to other components, as they form one unit. For example, the number of spots should at least fit the number of pixels at the image sensor and the number of macrocells on the storage medium. On the basis of principles known from conventional optical storage systems, like the Compact Disc (CD) player, Digital Versatile Disc (DVD) player and Blu-ray disc player, the dimensions and typical features for the T-ROM optical storage system can be derived. In this Appendix the components are discussed separately.

A.1 Illumination Unit

For illuminating the data on the storage medium a laser diode with a wavelength of 405 nm is used. Due to thermal effects the tolerance on the wavelength is approximately 5 nm.

Table A.1: Illumination unit variables.

Parameter	**Variable**	**Value**	**Unit**
Wavelength	λ	405	nm

A.2 Image Sensor

A second component in the T-ROM system is the image sensor. As the image sensor is the limiting component in the system (due to its relatively high cost) it is discussed first. This image sensor is of a silica base and has to represent the bit pattern on the storage medium by detecting the light that is let trough by the transparant bits. In figure A.1 a schematic representation of the image sensor is given. The pixel dimension is denoted by parameter c. The dimension of the sensor surface u depends on the storage medium dimension d, as shown in figure A.3 and will be discussed later, according to

$$u = \frac{d}{Q}, \tag{A.1}$$

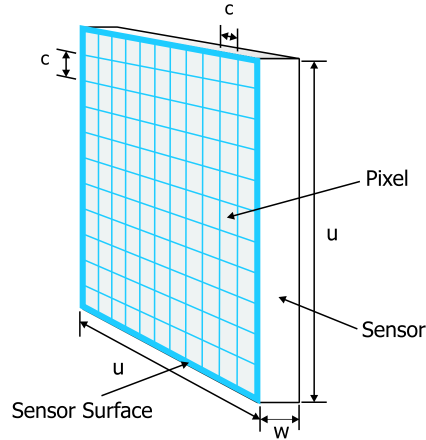

Figure A.1: Schematic representation of a image sensor.

where Q represents the magnification of the data bits on the image sensor pixels. Now the number of pixels K can be given by

$$K = \frac{u^2}{p^2} \cdot 10^6. \quad \text{(A.2)}$$

The used values for the variables are given in table A.2.

Table A.2: Image sensor variables.

Parameter	**Variable**	**Value**	**Unit**
Sensor Pixel Length	c	6.7	μm
Sensor Surface Thickness	w	1	mm
Magnification	Q	1	
Sensor Surface Length	u	7.3	mm
Number of pixels	K	$1.2 \cdot 10^6$	

A.3 Probe Generating Element

For creating the spots a probe generating element is used. When illuminating the array with apertures an array of spots is created at the so-called Talbot distance. The talbot effect is illustrated in figure 2.1 for an one dimensional case. The result for the two dimensional situation is illustrated in figure A.2. The probe generator has a quartz base with a chromium layer and has dimension of k x m x n mm. The array of apertures is printed in the chromium layer. The variable p represents the spot pitch. The spot diameter a (full width at half maximum) is defined by

$$a = \frac{\lambda}{2NA}, \quad \text{(A.3)}$$

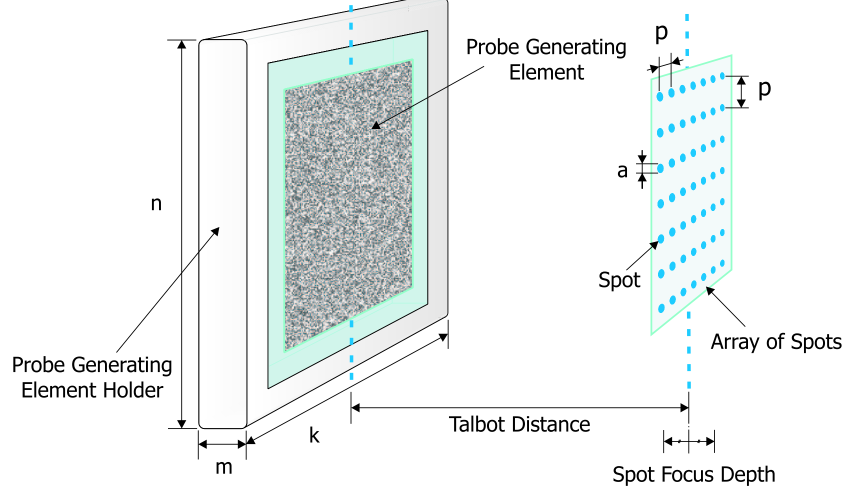

Figure A.2: Schematic representation of the probe generating element.

where λ is the wavelength of the light beam and NA the numerical aperture. Also the depth of focus is a consequence of the used wavelength and NA. The depth of focus is formulated as

$$F_D = \frac{\lambda}{2(NA)^2}. \quad (A.4)$$

The number of generated spots N directly depends on the number of used pixels K on the image sensor. When using a linear oversampling rate of R the number of spots is defined by

$$N \geq \frac{K}{R^2}. \quad (A.5)$$

The used values for the parameters are listed in table A.4.

Table A.3: Probe generating element variables.

Parameter	**Variable**	**Value**	**Unit**
Probe Generating Element Length	n	7.3	mm
Probe Generating Element Width	k	7.3	mm
Probe Generating Element Thickness	m	0.5	mm
Numerical Aperture	NA	0.6	
Oversampling Rate	R	2	
Talbot Distance	z_T	0.9	mm
Spot Diameter (FWHM)	a	338	nm
Spot Focus Depth	F_D	563	nm
Number of Spots	N	$3.0 \cdot 10^5$	

A.4 Storage Medium

The storage medium is the component that contains the information to be read. The storage medium carrier consists of a quartz base, with a linear dimension of h, and data imprinted in a chromium layer. On this colorless glass made of almost pure silica an area is reserved for data storage as is shown in figure A.3. The carrier is placed in an aluminium holder with dimensions e x f x g mm. The structure of the medium can be divided in two parts: macrocells and bits. A macrocell is divided in a number of bits and the bits are transparent or non-transparent areas. This illustrated in figure 2.7. A bit in one macrocell has a length of b, and is also known as the channel bit length (CBL), and is defined by

$$b = \frac{a}{\rho_{tangential}}. \tag{A.6}$$

Here a spot diameter of a nm is used and $\rho_{tangential}$ denotes the relative tangential density of the bits in one macrocell. In the transversal direction the bits are located in tracks with a width of t nm, also know as the track pitch (TP), and is defined by

$$t = \frac{a}{\rho_{transversal}}. \tag{A.7}$$

Here $\rho_{transversal}$ gives the relative transversal density of the tracks in one macrocell. Further, with a user storage capacity V and with an encoding efficiency η_{enc}, the total storage capacity S is defined as

$$S = \frac{V}{\eta_{enc}}. \tag{A.8}$$

Now the dimension of one macrocell depends on the total storage capacity and on the oversampling rate by the image sensor pixels R. The dimension of one macrocell, in μm, is given by

$$p = Rc, \tag{A.9}$$

and equals the spot pitch. The corresponding total linear data dimension d, in mm, follows from

$$d^2 = \frac{8 \cdot 1024 \cdot 1024}{10^{12}} btS. \tag{A.10}$$

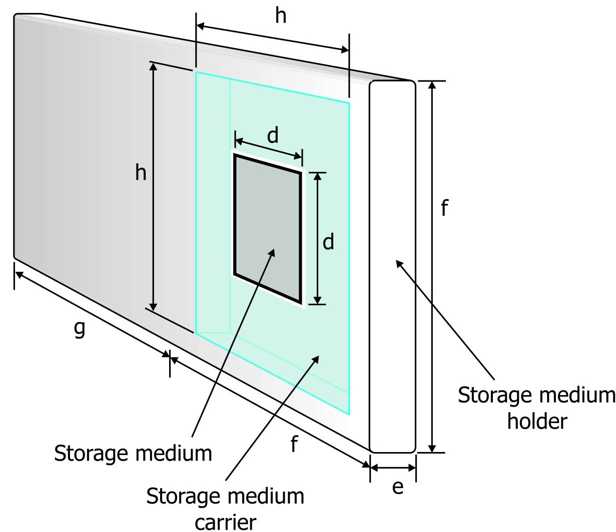

Figure A.3: Schematic representation of the storage medium holder.

The linear data dimension is used to calculate the linear sensor dimension, as given by A.1.

A data carrier contains as much macrocell as there are spots, and therefore the number of macrocells is N. From the foregoing calculations can be made to show the number of bits per macrocell, the number of bits per track and the number of tracks per macrocell. The number of bits per macrocell M_m can be given by

$$M_m = \frac{c^2}{bt} \cdot 10^6. \tag{A.11}$$

Further. the total number of bits per track M_t can be given by

$$M_t = \frac{c}{b} \cdot 10^3. \tag{A.12}$$

Finally the total number of tracks per macrocell T can be given by

$$T = \frac{c}{t} \cdot 10^3. \tag{A.13}$$

For the data carrier the used values for the parameters are listed in table A.4.

Table A.4: Storage medium variables.

Parameter	**Variable**	**Value**	**Unit**
Medium Carrier Dimension	h	11	mm
Medium Dimension	f	15	mm
Medium Holder Length	g	10	mm
Medium Holder Thickness	e	1	mm
User Storage Capacity	V	100	Mb
Relative Tangential Density	$\rho_{tangential}$	4.5	
Relative Transversal Density	$\rho_{transversal}$	0.8	
Encoding Efficiency	η_{enc}	0.5	
Total Storage Capacity	S	200	Mb
Channel Bit Length	b	75	nm
Track Pitch	t	422	nm
Storage Medium Area Dimension	d	7.3	mm
Macrocell dimension	p	13.4	mm
Number of Bits per Macrocell	M_m	2837	
Number of Bits per Track	M_t	89	
Number of Tracks per Macrocell	T	32	

Appendix B

Piezoelectric models

B.1 Linearized Piezoelectric Relations

The most widely recognized description of piezoelectric behavior was published by a standards committee of the IEEE in 1987 [33]. The formulated linearized constitutive relations, presented in the publication, can form the basis for modelling piezoelectric behavior. The electrical relation is obtained from an unstressed piezoelectric element placed under the influence of an electrical field. The electrical condition is given by

$$D = \varepsilon E. \tag{B.1}$$

This expression relates the electric field strength E by the permittivity of the element ε to the dielectric displacement D (charge per unit area). At a zero electric field strength, the mechanical condition of the same element is given by

$$S = sT. \tag{B.2}$$

Here quantity T gives the applied stress, quantity S is the strain and their relationship is described by the compliance of the piezoelectric element s. Since the piezoelectric effect relates the electrical and mechanical behavior of piezoelectric elements, the electrical and mechanical behavior can be formulated by a set of coupled equations according to

$$\begin{cases} S &= s^E T + dE, \\ D &= dT + \varepsilon^T E. \end{cases} \tag{B.3}$$

Here T and E form the independent variables. Since the choice of the independent variables is arbitrary, different sets of coupled equations exist. Alternate forms of the constitutive equations are given by

$$\begin{cases} E &= -gT + \frac{1}{\varepsilon^T} D, \\ S &= s^D T + gD, \end{cases} \tag{B.4}$$

$$\begin{cases} E &= -hS + \frac{1}{\varepsilon^S} D, \\ T &= c^D S - hD, \end{cases} \tag{B.5}$$

$$\begin{cases} D &= eS + \varepsilon^S E, \\ T &= c^E S - eE, \end{cases} \tag{B.6}$$

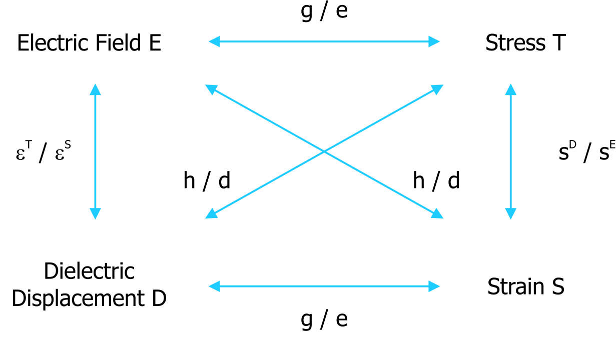

Figure B.1: Linear piezoelectric relations.

In these equations, s^D and s^E are the elastic compliances, ε^T and ε^S are the electric permittivities and c^D and c^E are the elastic stiffness. It is noted that the reciprocal of the elastic stiffness is linear related to the elastic compliances. The superscripts refer to the quantity kept constant under boundary condition. Further d and g are the piezoelectric strain constants and h and e are the piezoelectric stress constants. An overview of all relations is given in figure B.1. The stress T, strain S, electric field E and dielectric displacement D are related to respectively force F, elongation x, voltage u and charge q, as is shown schematically in figure 4.1. For a stacked piezoelectric element, with n wafers, it applies

$$\begin{aligned} T(t) &= \frac{-F(t)}{A}, \\ S(t) &= \frac{x(t)}{L}, \\ E(t) &= \frac{nu(t)}{L}, \\ D(t) &= \frac{q(t)}{nA} = \frac{i(t)t}{nA}. \end{aligned} \tag{B.7}$$

Here L and A represents respectively the length and surface area of a piezoelectric element, as given in figure 4.6. The parameter i represent the current through the element.

To link electrical and mechanical quantities, double subscripts (for example d_{pq}) are introduced. The first subscript (p) gives the direction of the electric field, the second (q) describes the direction of the material response. In this section the actuator is assumed to work in the 33-direction, also called the longitudinal mode, as both the electrical field and strain are in the same direction. This is shown schematically in figure 4.6, For a more detailed discussion one is referred to [28].

When controlling the voltage across the piezoelectric element, the electric circuit has to be closed. Consequently, the electric field E becomes constant and the required current can flow to electrically charge the element. In a voltage configuration the elongation, in the 3-direction, can be obtained from

$$S_3 = s_{33}^E T_3 + d_{33} E_3. \tag{B.8}$$

By controlling the voltage, and so the electric field, the elongation x can be written as

$$x = nd_{33}u - \frac{1}{k_p^E} F. \tag{B.9}$$

The force F is an externally applied force. From (B.9) it can be seen that F will result in a reduction of the elongation. The piezoelectric element stiffness k_p^E, defined for a constant electric field strength,

can be obtained when considering a zero input u, and so E equals 0. This results in

$$k_p^E = \frac{AE_y\left(1 - k_{33}^2\right)}{L}. \tag{B.10}$$

Here E_y is the modulus of elasticity. The coupling factor k_{33} is a measure of the effectiveness of the piezoelectric effect. It describes the ability of a piezoelectric material to transform electrical energy into mechanical energy and vice versa. For more information one is referred to [28].

Finally, for a discussion on the relations between the piezoelectric relations given in this section and the piezoelectric relations given in section 4.1.1, one referred to [1].

B.2 Generalized Maxwell Model

The Maxwell slip model is introduced in [9] to describe the effect of hysteresis present in a piezoelectric element between voltage input and element elongation. In fact in this model a distinction is made in modelling the hysteresis and piezoelectric effect. This becomes clear when defining

$$u_p(t) = u_{in}(t) - u_H(t), \tag{B.11}$$

where voltage u_{in} is the applied voltage and voltage u_H is defined as a function of the applied charge according to

$$u_H(t) = H\left(q_{in}(t)\right). \tag{B.12}$$

Here H represents the hysteresis effect on the electrical side.

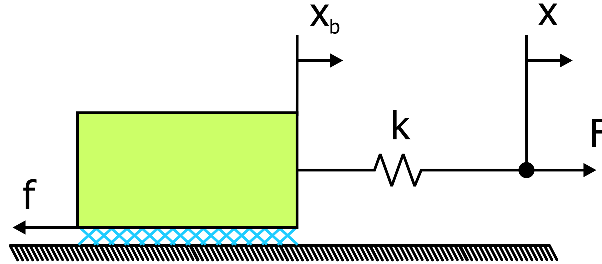

Figure B.2: Maxwell slip model.

In the generalized Maxwell model the hysteresis effect is completely mechanically represented. Afterwards a transformation to the electrical domain is made. A force F represents the force acting on the endpoint of an ideal spring, which is coupled to a massless element, as function of the displacement of the endpoint of the spring x The rigid mass is suffering for a coulomb friction independent of the sliding velocity. A schematic representation is given in figure B.2. The constitutive behavior of the hysteresis model can be described by

$$F(t) = \begin{cases} k\left(x(t) - x_b(t)\right) & \text{if } \left|k\left(x(t) - x_b(t)\right)\right| < f, \\ f\,sign(\dot{x}(t)) \wedge x_b(t) = x(t) - \frac{f}{k} sign(\dot{x}(t)) & \text{if } \left|k\left(x(t) - x_b(t)\right)\right| \geq f. \end{cases} \tag{B.13}$$

Table B.1: Maxwell capacitors and saturation voltages for 10 parallel Maxwell slip models.

Element	1	2	3	4	5	6	7	8	9	10
Maxwell Capacitor	0.1710	0.1470	0.1230	0.0990	0.0749	0.0509	0.0269	0.0028	0.0212	1.4665
Saturation Voltage	0.0560	0.0963	0.1208	0.1296	0.1227	0.1000	0.0616	0.0074	0.0624	4.8024

In this relation k represents the spring stiffness, f represents the breakaway friction force and x_b is the position of the massless element. By parallel coupling an infinite number of Maxwell models a so-called generalized Maxwell model is obtained. In the case that n Maxwell models are coupled, relation (B.13) changes in

$$F(t) = \sum_{i=1}^{n} F_i(t) = \sum_{i=1}^{n} \begin{cases} k_i\left(x(t) - x_{b_i}(t)\right) & \text{if } |k_i\left(x(t) - x_{b_i}(t)\right)| < f_i, \\ f_i sign(\dot{x}(t)) \wedge x_{b_i}(t) = x(t) - \frac{f_i}{k_i} sign(\dot{x}(t)) & \text{if } |k_i\left(x(t) - x_{b_i}(t)\right)| \geq f_i, \end{cases} \tag{B.14}$$

From a hysteresis measurement, from a relaxed state, the model can be parameterized directly from a piecewise linear fit of the rising curve of the hysteresis, as shown in figure B.4. The curve fit for n Maxwell models results in n slopes, representing the spring stiffness of each Maxwell model. From the piecewise approximation of the hysteresis the stiffness can be obtained form

$$\underline{k} = \mathbf{A}^{-1}\underline{s}. \tag{B.15}$$

Here $\underline{s}$ is a nx1 vector of slopes, $\mathbf{A}$ is an nxn upper triangular matrix of ones and $\underline{k}$ is a nx1 vector of Maxwell model spring stiffness. The breakaway force can be obtained from

$$\underline{f} = \mathbf{K}\underline{x}. \tag{B.16}$$

where $\underline{f}$ is a nx1 vector of breakaway forces, $\mathbf{K}$ is an nxn diagonal matrix of spring stiffness and $\underline{x}$ is a nx1 vector of spring endpoints. Once the vectors $\underline{k}$ and $\underline{f}$ are determined also the force $F(t)$ to spring endpoint x relation is know according to (B.14). The electrical parameters can be obtained by matching the mechanical parameters according to

$$\begin{cases} F(t) & \rightarrow u_H(t), \\ x(t) & \rightarrow q_{in}(t), \\ k_i & \rightarrow C_{m\ i}^{-1}, \\ f_i & \rightarrow u_{mi}. \end{cases} \tag{B.17}$$

Here C_m and u_m are respectively a so-called linearized Maxwell capacitor and a Maxwell saturation voltage.

As the hysteresis effect occurs in the electrical domain the parameters can be determined by a piecewise linear fit of the measured voltage versus charge data. But, as charge measurements are not available in the present setup, another approach is used here to show the working of the model. First an assumption is made for the transformer ratio T. Then, the voltage and charge relation can be extracted from a voltage versus displacement measurement, by using the definition given in (4.2). The voltage versus displacement measurement performed on a piezoelectric element, with a blocking force $F_b = 216$ N and a free elongation $x_{max} = 18$ μm, is shown in figure B.3. The corresponding Maxwell capacitors C_m and saturation voltages are given in table B.1.

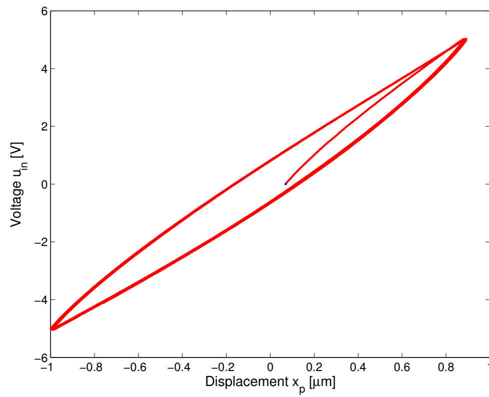

Figure B.3: Hysteresis measurement.

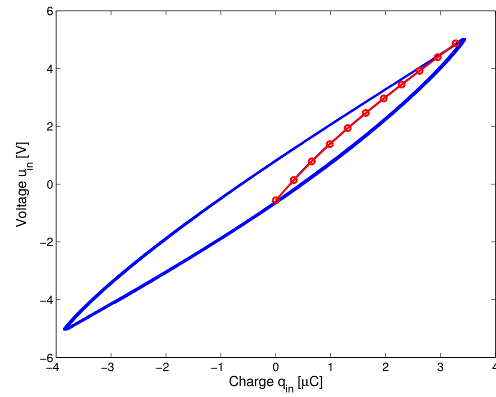

Figure B.4: Piecewise linear fit on rising curve.

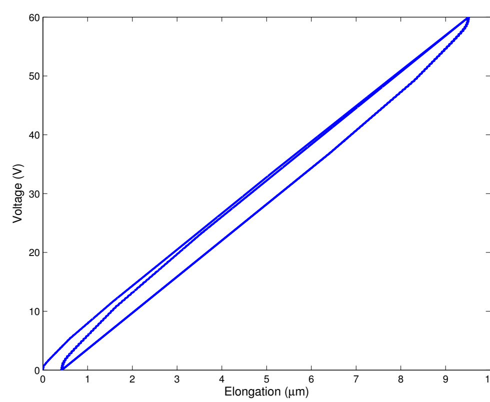

Figure B.5: Hysteresis simulation with an input voltage varying between 0 V and 60 V.

Appendix C

Flexures

C.1 Flexible Hinge

A flexible hinge and its parameters are given in figure C.1. Parameter E_y represents the modulus of elasticity and t represents the hinge thickness. The stiffness in different directions can be approximated with the equations given below as long as small rotations are considered, $h, D \ll L$ and $b, t < L$ and also $\sqrt{\frac{h}{D}}$ is in the realistic range between 0.1 and 0.5. The angular stiffness in point A in respectively β, γ and α-direction can be approximated by

$$k_\beta = \left(\frac{dM}{d\beta}\right)_A = 0.093\sqrt{\frac{h}{D}}E_y t h^2, \tag{C.1}$$

$$k_\gamma = \left(\frac{dM}{d\gamma}\right)_A = 0.04\sqrt{\frac{h}{D}}E_y t^3 = 0.43\frac{t^2}{h^2}k_\beta, \tag{C.2}$$

$$k_\alpha = \left(\frac{dM}{d\alpha}\right)_A = 0.05\sqrt{\frac{h}{D}}E_y t^3 \left(1.2 + \frac{D}{h}\right)^{-1} = 0.54\frac{t^2}{h^2}\left(1.2 + \frac{D}{h}\right)^{-1} k_\beta. \tag{C.3}$$

A more detailed description on these relations can be found in [15]. Further, in case a force is acting in point B on a distance L to the pivot, the stiffness in respectively in u, v and w direction is approximated by

$$k_u = \left(\frac{dF}{dx}\right)_B = 0.48\sqrt{\frac{h}{D}}E_y t, \tag{C.4}$$

$$k_v = \left(\frac{k_\gamma}{L^2}\right)_B = 0.04\sqrt{\frac{h}{D}}\frac{E_y t^3}{L^2} = 0.08\frac{t^2}{L^2}k_u, \tag{C.5}$$

$$k_w = \left(\frac{k_\beta}{L^2}\right)_B = 0.093\sqrt{\frac{h}{D}}\frac{E_y t h^2}{L^2} = 0.19\frac{h^2}{L^2}k_u. \tag{C.6}$$

C.2 Flexure Mechanism

By using the approximations given in the previous section the parallel motion of a flexure mechanism, as shown in figure C.2(a), can be analyzed. The parallelism of this flexure guiding system can be

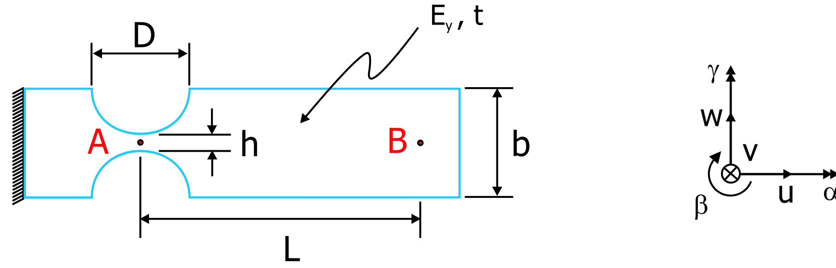

Figure C.1: Parameterized flexible hinge.

evaluated on the basis of the free body diagram shown in figure C.2(b). In this lumped parameter system uniformity is assumed and hence by means of equilibrium

$$\begin{aligned} M_1 &= M_2 = M, \\ K_1 &+ K_2 = F, \\ N_1 &= -N_2 = N. \end{aligned} \tag{C.7}$$

From moment equilibrium it follows for the rigid assumed body that

$$2M + Fa - Nb = 0. \tag{C.8}$$

The moment M and normal force N are induced by the driving force F. If the beams are free of normal forces, no body rotation in β-direction will be obtained. Otherwise, for movements over a relatively small stroke, the body rotation $\Delta\beta$ can be interpreted as an extension Δu of one beam and a shortening Δu of the other beam according to

$$\Delta\beta = \frac{2\Delta u}{b}. \tag{C.9}$$

Parameter b represents the in-between distance of the beams.

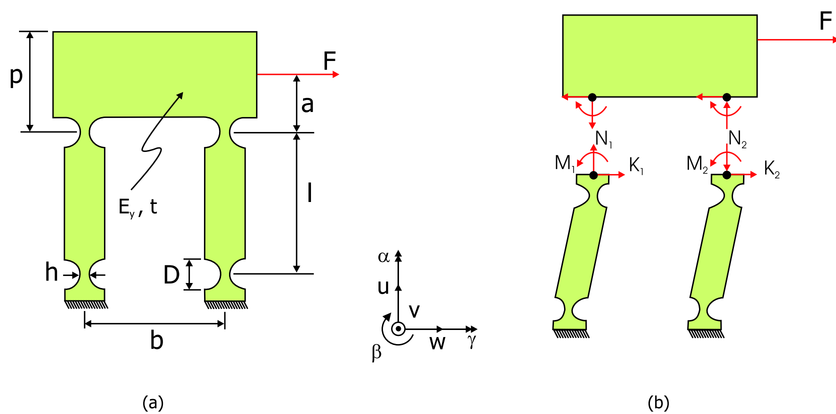

Figure C.2: Parameterized flexure mechanism (a) and its free body diagram (b).

To obtain the elongation Δu observe the beam free body diagram given in figure C.3(a). For a tilted beam, with an angle β, and due to internal symmetry, it follows

$$M_a = M_b = -k_\beta \beta = M. \tag{C.10}$$

For beam 1 of the flexure mechanism given in figure C.2 it follows, from moment equilibrium and by making use of the relations given in C.7, that

$$2M = K_1 l \cos\beta + Nl \sin\beta, \tag{C.11}$$

and for beam 2 it follows that

$$2M = K_2 l \cos\beta - Nl \sin\beta. \tag{C.12}$$

By equalization of (C.11) and (C.12), while observing a small angle ($\beta \ll 1$), it follows that

$$M = \frac{Fl}{4}. \tag{C.13}$$

Hence, relation (C.8) can be rewritten in

$$N = \frac{F}{b}\left(\frac{l}{2} + a\right). \tag{C.14}$$

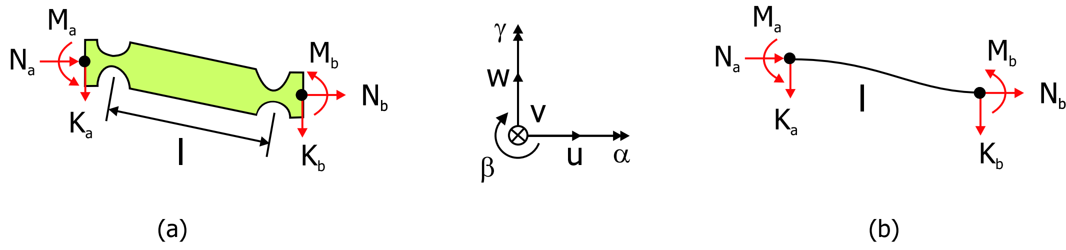

Figure C.3: Free body diagram of a rigid beam (a) and a uniform beam (b).

Observing the same flexure mechanism, but now with leaf springs in stead of rigid beams with flexible pivots. In analogy with the bending of rigid beams, also bending uniform beams can be analyzed. The elongation, deflection and slope of a uniform beam, as shown in figure C.3(b), are defined in [6] as

$$\begin{aligned} u_b - u_a &= \frac{l}{E_y A} N_b & \text{and} \quad & N_a = -N_b, \\ w_b - w_a - \beta_a l &= \frac{l^3}{3E_y I} K_b - \frac{l^2}{2E_y I} M_b & \text{and} \quad & K_a = -K_b, \\ \beta_b - \beta_a &= \frac{l^2}{2E_y I} K_b - \frac{l}{E_y I} M_b & \text{and} \quad & M_a = -M_b + K_b l. \end{aligned} \tag{C.15}$$

Here, parameters E_y, A and I represent respectively the modulus of elasticity, the beam cross area and the second moment of the beam area. As for the situation in figure C.3(b) $\beta_b - \beta_a = 0$, it follows

$$M_b = \frac{K_b l}{2} = M_a = M. \tag{C.16}$$

From the relation in (C.15) it also follows that the normal forces N_a en N_b are independent of the forces K_a en K_b. Therefore, by considering uniformity of the two beams, it follows for the body of the flexure mechanism in figure C.2 that

$$K_1 = K_2 = \frac{F}{2}. \tag{C.17}$$

With $K_b = K_1$ it follows from relation (C.16) that

$$M = \frac{Fl}{4}. \tag{C.18}$$

This force and moment relation equals the relation given in (C.13).

Now the body rotation $\Delta\beta$ as function of the stroke Δw in w-direction can be derived. The stroke Δw is related to the driving force F by two parallel combinations of two springs acting in series, with each a spring stiffness k_w. Hence

$$F = k_w \Delta w. \tag{C.19}$$

Further, the beam elongation can be obtained by considering two springs in series, with each a spring stiffness k_u. Therefore

$$N = \frac{k_u}{2} \Delta u. \tag{C.20}$$

Together with the force and moment relation given in (C.13) the beam elongation Δu as function of stroke Δw can be obtained from (C.8). After some calculations it follows that

$$\Delta u = \frac{2k_w}{bk_u} \left(\frac{l}{2} + a \right) \Delta w. \tag{C.21}$$

Finally, by using (C.9) the body rotation is given by

$$\Delta\beta = 3.04 \left(\frac{h}{bl} \right)^2 \left(\frac{l}{2} + a \right) \Delta w. \tag{C.22}$$

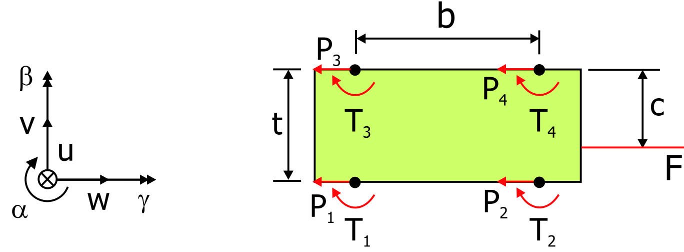

Figure C.4: A bottom view of the flexure mechanism free body diagram given in figure C.2.

In analogy with the body rotation in β direction also the body rotation in α direction can be approximated with the flexible hinge approximations. Observing figure C.4 it follows that

$$\begin{aligned} P_1 + P_2 &= \frac{F}{2}, \\ P_3 + P_4 &= \frac{F}{2}, \\ T_1 = T_2 = T_3 &= T_4 = T. \end{aligned} \tag{C.23}$$

From moment equilibrium it follows that

$$Fc + 4T - (P_3 + P_4)\, t = 0. \tag{C.24}$$

Rewriting gives

$$T = \frac{F}{4} \left(\frac{t}{2} - c \right). \tag{C.25}$$

The angular rotation of the flexure mechanism given in figure C.2(a) can be calculated by assuming 4 parallel combinations of 2 springs in series, each with a stiffness k_α. Further, by using relation (C.19) and also the angular springs stiffness approximation in (C.3), it follows from (C.25) for the angular body rotation that

$$\Delta\alpha = 1.86 \left(\frac{Dh}{l^2 t^2} \right) \left(\frac{t}{2} - c \right) \Delta w. \tag{C.26}$$

It should be noted that this relation is only valid as the condition $\frac{D}{h} \gg 1.2$ is met.

Appendix D

Actuator Vibrations Modes

For the conceptual actuator design, discussed in Chapter 5, the second and third vibration modes are shown in respectively figure D.1 and figure D.2.

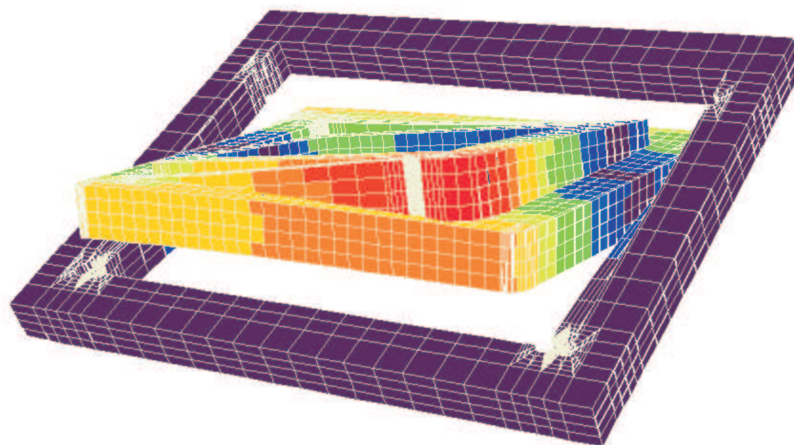

Figure D.1: Finite Element Model of the x and y stage showing the second vibration mode with an eigenfrequency at 863 Hz.

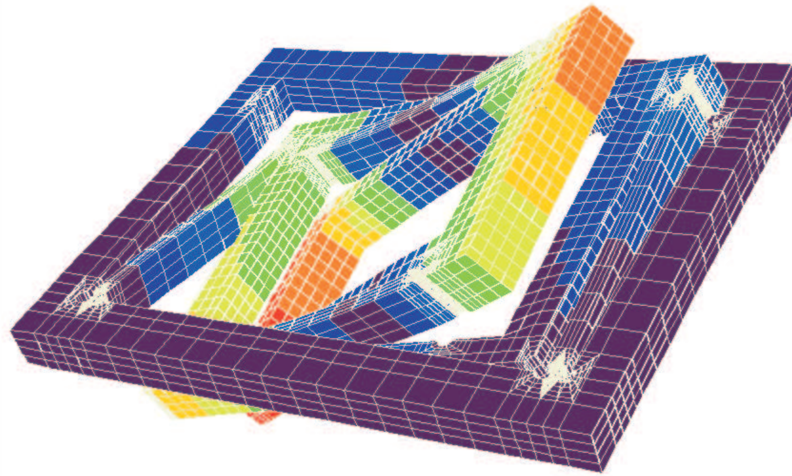

Figure D.2: Finite Element Model of the x and y stage showing the third vibration mode with an eigenfrequency at 1090 Hz.

Appendix E

Stage Dynamic System Model

The translation stage shown in figure 5.11 is a simplified model of the model shown in figure E.1. The simplification is based on integrating the lever amplification ratio in the system

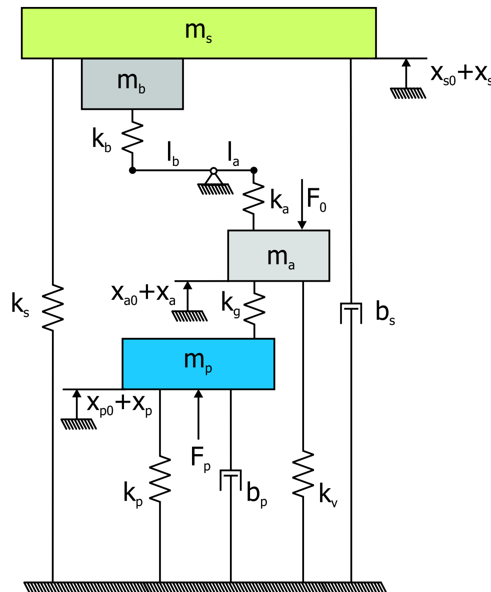

Figure E.1: Schematic representation of a flexure mechanism driven by a piezoelectric element via a lever.

For a uniform lever, with an amplification ratio $i = \frac{l_b}{l_a}$, simplifications are shown in figure E.2. The masses m_a and m_b are represented as a third of the lever mass on the right and left side of the hinge. Hence

$$\begin{aligned} m_a &= \frac{\rho l_a l_w l_h}{3}, \\ m_b &= i m_a. \end{aligned} \tag{E.1}$$

The parameters l_w and l_h are respectively the lever width and height and ρ represents the lever material

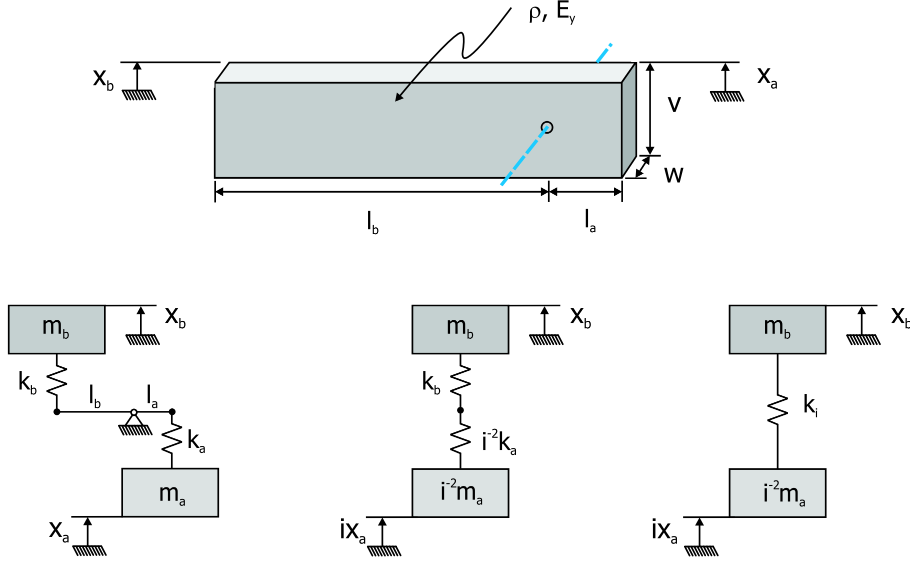

Figure E.2: A lever and its simplified dynamic representations.

density. From uniform beam theory [15] it follows for the stiffness k_a and k_b respectively that

$$\begin{aligned} k_a &= \frac{E_y l_w l_h^3}{4 l_a^3}, \\ k_b &= \frac{E_y l_w l_h^3}{4 l_b^3} \qquad = i^{-3} k_a. \end{aligned} \tag{E.2}$$

The material modulus of elasticity is denoted by E_y. Simplifications can be made by considering the fact that the inertia of a mass m_a at a distance l_a equals the inertia of a mass m_a/i^2 at a distance il_a [15]. Likewise, a stiffness k_a, acting at a distance l_a and shifted by x_a, equals a stiffness k_a/i^2, acting at a distance il_a and shifted by ix_a. As the springs in figure E.2 are acting in series it can be derived for stiffness k_i that

$$k_i = \frac{k_a}{i^2 (1+i)} = \frac{E_y l_w l_h^3}{4 l_a^3 i^2 (1+i)}. \tag{E.3}$$

E.1 Dynamic System Model

For the simplified dynamic system representation, shown in figure 5.11, the equations of motion can be given by equating the sum of forces to the mass acceleration. Hence

$$\begin{aligned} i^{-2} m_p i \ddot{x}_p &= i^{-1} F_p - i^{-2} k_p (i x_p - x_0) - i^{-2} b_p (i \dot{x}_p - \dot{x}_0) + i^{-2} k_g (i x_a - i x_p), \\ i^{-2} m_a i \ddot{x}_a &= -i^{-2} k_g (i x_a - i x_p) - i^{-2} k_v (i x_a - x_0) + k_i (x_s - i x_a), \\ (m_s + m_b) \ddot{x}_s &= -k_s (x_s - x_0) - b_s (\dot{x}_s - \dot{x}_0) - k_i (x_s - i x_a). \end{aligned} \tag{E.4}$$

Position x_0 represents the fixed world and can therefore be omitted. The given second-order differential equations can be rewritten in a set of first-order differential equations. By defining the state vector of the system given as

$$\underline{x} = \begin{bmatrix} x_p & x_a & x_s & \dot{x}_p & \dot{x}_a & \dot{x}_s \end{bmatrix}^T,$$

and with the force F_p as system input and the positions x_p and x_s as system output, the state space representation of the system can be given by

$$\begin{cases} \underline{\dot{x}} &= \mathbf{A}\underline{x} + \mathbf{B}\underline{u}, \\ \underline{y} &= \mathbf{C}\underline{x} + \mathbf{D}\underline{u}. \end{cases} \tag{E.5}$$

The system matrix $\mathbf{A}$, the input matrix $\mathbf{B}$, the output matrix $\mathbf{C}$ and direct transmission matrix $\mathbf{D}$ are given by

$$\mathbf{A} = \begin{bmatrix} 0 & 0 & 0 & 1 & 0 & 0 \\ 0 & 0 & 0 & 0 & 1 & 0 \\ 0 & 0 & 0 & 0 & 0 & 1 \\ \frac{-k_p-k_g}{m_p} & \frac{k_g}{m_p} & 0 & \frac{-bp}{m_p} & 0 & 0 \\ \frac{k_g}{m_a} & \frac{-k_g-k_v-i^2k_i}{m_a} & \frac{ik_i}{ma} & 0 & 0 & 0 \\ 0 & \frac{ik_i}{m_s+m_b} & \frac{-k_i-k_s}{m_s+m_b} & 0 & 0 & \frac{-b_s}{m_s+m_b} \end{bmatrix},$$

$$\mathbf{B} = \begin{bmatrix} 0 & 0 & 0 & \frac{1}{m_p} & 0 & 0 \end{bmatrix}^T,$$

$$\mathbf{C} = \begin{bmatrix} 1 & 0 & 0 & 0 & 0 & 0 \\ 0 & 0 & 1 & 0 & 0 & 0 \end{bmatrix},$$

$$\mathbf{D} = \begin{bmatrix} 0 \\ 0 \end{bmatrix}.$$

E.2 Quasi-static Transfer functions

The equations of motion, given in in (E.4), after Laplace transform are be given by

$$\begin{aligned} \left[i^{-2}m_p s^2 + i^{-2}b_p s + i^{-2}(k_p + k_g)\right] ix_p &= F_p + \left[i^{-2}k_g\right] ix_a, \\ \left[i^{-2}m_a s^2 + i^{-2}(k_v + k_g) + k_i\right] ix_a &= \left[i^{-2}k_g\right] ix_p + [k_i]\, x_s, \\ \left[(m_s + m_b)s^2 + b_s s + (k_s + k_i)\right] x_s &= [k_i]\, ix_a. \end{aligned}$$

In case stiffness $k_g \to \infty$ ($x_a = x_p$) the equations of motion after Laplace transform become

$$\begin{aligned} \left[i^{-2}(m_p + m_a)s^2 + i^{-2}b_p s + i^{-2}(k_p + k_v) + k_i\right] ix_p &= i^{-1}F_p + [k_i]\, x_s, \\ \left[(m_s + m_b)s^2 + b_s s + (k_s + k_i)\right] x_s &= [k_i]\, ix_p. \end{aligned}$$

In the frequency range where the moving parts behave as freely moving rigid masses the mechanical transfer is constant. The quasi-static transfer functions between force F_p and position x_p and x_s can now be given by respectively

$$\frac{x_s}{F_p} = \frac{k_i i^2}{k_s k_i i^2 + k_s k_p + k_s k_v + k_i k_p + k_i k_v}, \tag{E.6}$$

$$\frac{x_p}{F_p} = \frac{(k_s + k_i)\, i}{k_s k_i i^2 + k_s k_p + k_s k_v + k_i k_p + k_i k_v}. \tag{E.7}$$

By combining (E.6) and (E.7) it follows for the position relation

$$\frac{x_s}{x_p} = \frac{k_i i}{k_s + k_i}. \tag{E.8}$$

In case both stiffness $k_g \rightarrow \infty$ and $k_i \rightarrow \infty$ ($x_a = x_p$ en $ix_p = x_s$) the equations of motion after Laplace transform can be written as

$$\left[(m_s + m_b + i^{-2}(m_p + m_a))s^2 + (b_s + i^{-2}b_p)s + k_s + i^{-2}(k_p + k_v)\right] x_s = i^{-1}F_p.$$

For the quasi-static transfer functions between force F_p and position x_p and x_s it follows respectively

$$\frac{x_s}{F_p} = \frac{i^2}{k_s i^2 + k_p + k_v}, \tag{E.9}$$

$$\frac{x_p}{F_p} = \frac{i}{k_s i^2 + k_p + k_v}. \tag{E.10}$$

The relation between x_s and x_p is now described by only the lever amplification i.

In case both stiffness $k_g \rightarrow \infty$ and $k_i \rightarrow \infty$ the stiffness k_{pg}, describing the stiffness relation between F_{act} and y_2 as defined in section 6.1, can be given by using relation (E.6). It follows that for k_{pg} that

$$k_{pg} = k_s + i^{-2}\,(k_p + k_v). \tag{E.11}$$

This stiffness relation may only be used by simultaneous considering the fact that

$$F_{act} = i^{-1}F_b. \tag{E.12}$$

Using the equation of motion after Laplace transform the mass m_{pg} and damping b_{pg} are given by

$$m_{pg} = m_s + m_b + i^{-2}(m_p + m_a), \tag{E.13}$$

and

$$b_{pg} = b_s + i^{-2}\,(b_p + b_v). \tag{E.14}$$

It is noted that the stage mass m_s should be composed by the individual stage masses, i.e. m_x, m_y and m_z, defined in table 5.1. In case no lever is included the stiffness, mass and damping relations are obtained by considering $i = 1$ and $m_a = m_b = 0$.

Appendix F

T-ROM Dynamic System Model

The second-order linear differential equations of (6.1) can be rewritten in a set of first-order differential equations. By defining the state vector of the system as

$$\underline{x} = \begin{bmatrix} x_c & x_f & x_{pg} & \dot{x}_c & \dot{x}_f & \dot{x}_{pg} \end{bmatrix}^T,$$

and defining the relative displacements $y_1 = x_f - x_c$ and $y_2 = x_{pg} - x_f$ as system outputs, the state space representation of the system is defined by

$$\begin{cases} \dot{\underline{x}} &= \mathbf{A}\underline{x} + \mathbf{B}\underline{u}, \\ \underline{y} &= \mathbf{C}\underline{x} + \mathbf{D}\underline{u}. \end{cases} \tag{F.1}$$

Output y_2 is the output of main interest as it describes the relation of the probe generator to the medium. At all times this position should be maintained. Output y_1 is only monitored as physically this position should be realistic. With the two inputs u_1 and u_2 respectively being $\ddot{x}_{dist}$ and F_{act}, the matrices are given by

$$\mathbf{A} = \begin{bmatrix} 0 & 0 & 0 & 1 & 0 & 0 \\ 0 & 0 & 0 & 0 & 1 & 0 \\ 0 & 0 & 0 & 0 & 0 & 1 \\ -\frac{k_f}{m_c} & \frac{k_f}{m_c} & 0 & -\frac{b_f}{m_c} & \frac{b_f}{m_c} & 0 \\ \frac{k_f}{m_f} & -\frac{k_{pg}}{m_f} - \frac{k_f}{m_f} & \frac{k_{pg}}{m_f} & \frac{b_f}{m_f} & -\frac{b_{pg}}{m_f} - \frac{b_f}{m_f} & \frac{b_{pg}}{m_f} \\ 0 & \frac{k_{pg}}{m_{pg}} & -\frac{k_{pg}}{m_{pg}} & 0 & \frac{b_{pg}}{m_{pg}} & -\frac{b_{pg}}{m_{pg}} \end{bmatrix},$$

$$\mathbf{B} = \begin{bmatrix} 0 & 0 \\ 0 & 0 \\ 0 & 0 \\ 1 & 0 \\ 0 & -\frac{1}{m_f} \\ 0 & \frac{1}{m_{pg}} \end{bmatrix},$$

$$\mathbf{C} = \begin{bmatrix} -1 & 1 & 0 & 0 & 0 & 0 \\ 0 & -1 & 1 & 0 & 0 & 0 \end{bmatrix},$$

$$\mathbf{D} = \begin{bmatrix} 0 & 0 \\ 0 & 0 \end{bmatrix}.$$

The transfer functions G_1 and G_2, mentioned in section 6.1, now describe the relation of F_{act} and y_1 and y_2 respectively. Transfer functions H_1 and H_2 describe the influence of the disturbance acceleration on y_1 and y_2 respectively.

Appendix G

Shock Simulation

The result for the Portable Drive Shock on position y_1 and y_2 are shown in figure G.1, for the Compaq Removable Drive Shock the results are shown in figure G.2 and for the Jog Shock the results are shown in figure G.3.

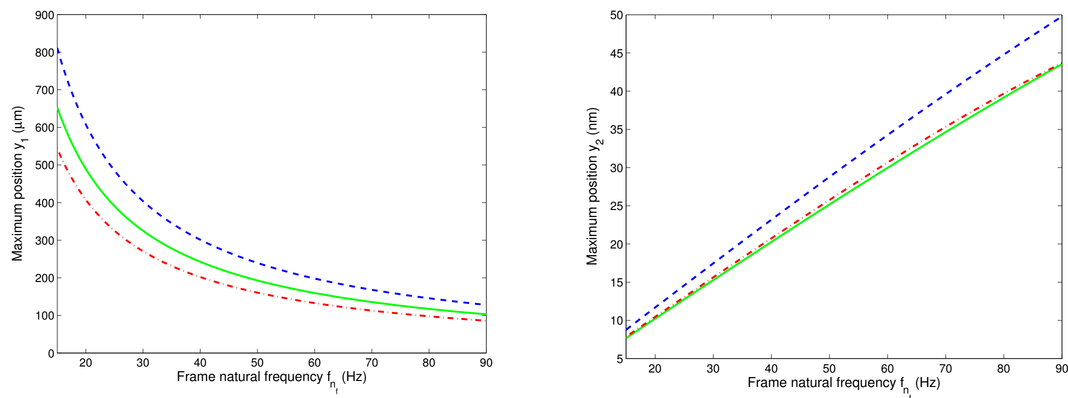

Figure G.1: Response y_1 (left) and y_2 (right) on the portable drive shock with β_f is 5% (dashed), 20% (solid) and 40% (dash-dotted).

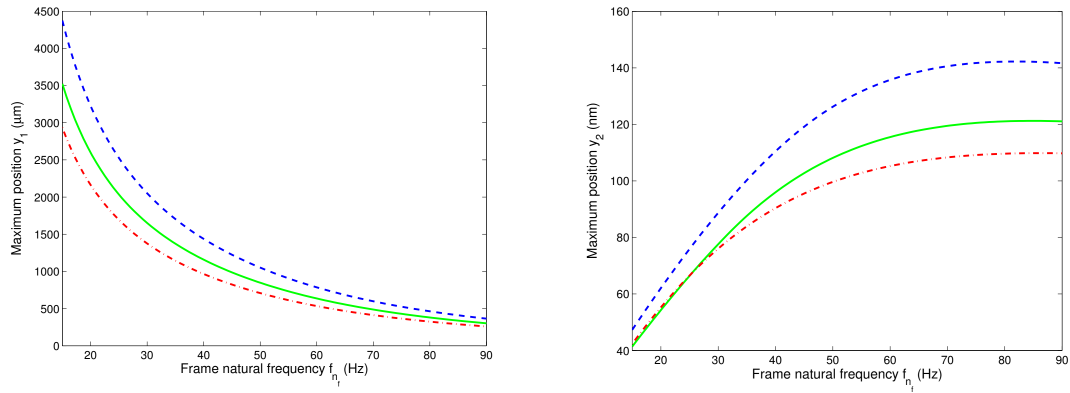

Figure G.2: Response y_1 (left) and y_2 (right) on the Compaq removable drive shock with β_f is 5% (dashed), 20% (solid) and 40% (dash-dotted).

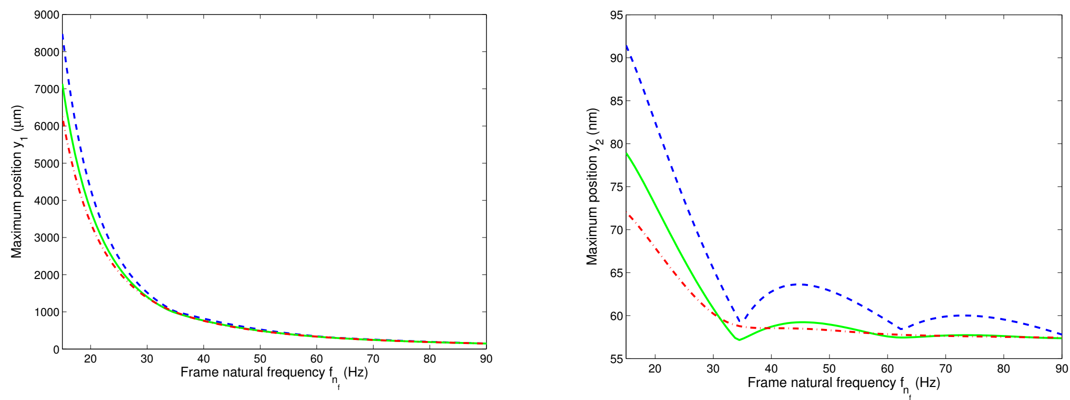

Figure G.3: Response y_1 (left) and y_2 (right) on the jog shock with β_f is 5% (dashed), 20% (solid) and 40% (dash-dotted).